Measurements of the CMB by the *Planck* satellite and their Implications - The Low Frequency Instrument

Carlo Burigana (INAF-IASF Bologna)
On behalf of LFI Consortium

Ecole Internationale Daniel Chalonge
12th Paris Cosmology Colloquium 2008
CMB, DM, DE, DARK AGES, LSS in the Standard Model of the Universe
George Smoot, Nobel Prize of Physics and Daniel Chalonge Medal

Observatoire de Paris, Paris Campus, 17-19 July 2008

Outline

- Description of *Planck*
  - Main parts
  - Performance
- Main differences between *Planck* & WMAP
- APS sensitivity
- Scanning strategy & systematics
- DPC & separation of CMB from foregrounds
- Cosmological implications
  - Parameters
  - Some examples: inflation, DE, adiabatic/isocurvature perturbations
- From cosmology to "astrophysical cosmology"
  - Reionization
  - SZ
- Astrophysics: Extragalactic sources
- Astrophysics: Galactic components & Solar System studies

A Planck view

FIG 1.2.—*Planck* focal plane unit. The HFI is inserted into the ring formed by the LFI horns, and includes thermal stages at 18 K, 4 K, 2 K and 0.1 K. The cold LFI unit (20 K) is attached by bipods to the telescope structure.

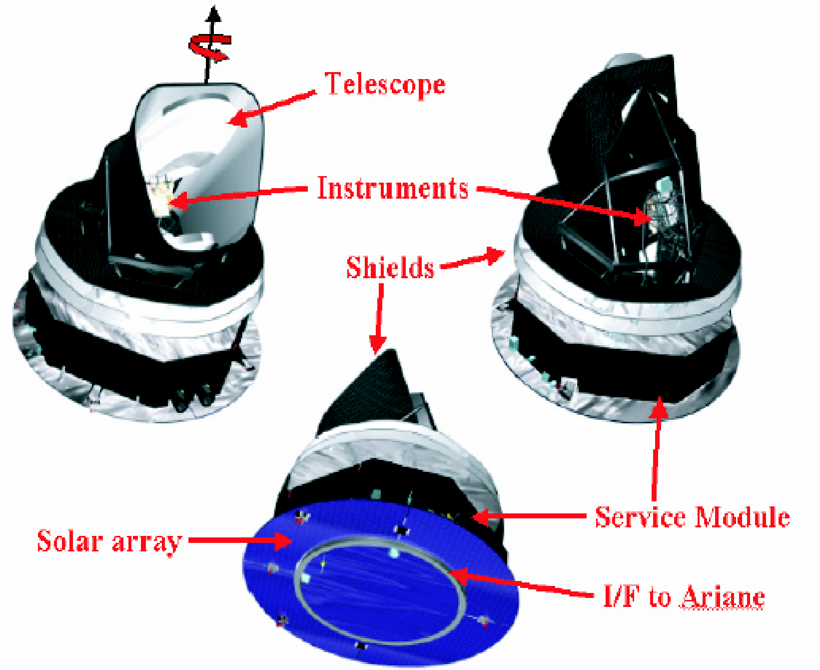

FIG 1.1.— Main elements of *Planck*. The instrument focal plane unit (barely visible) contains both LFI and HFI detectors. The function of the large baffle surrounding the telescope is to control the far sidelobe level of the radiation pattern as seen from the detectors. The specular conical shields (often called "V-grooves") thermally decouple the Service Module (which contains all warm elements of the satellite) from the Payload Module. The satellite spins around the indicated axis, such that the solar array is always exposed to the Sun, and shields the payload from solar radiation. Figures courtesy of Alcatel Space (Cannes).

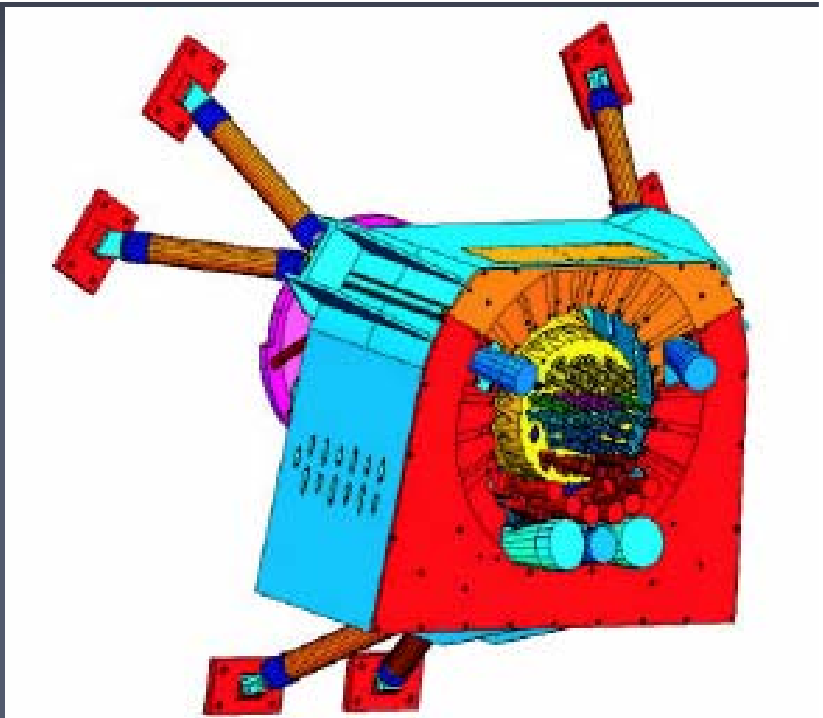

LFI view – I

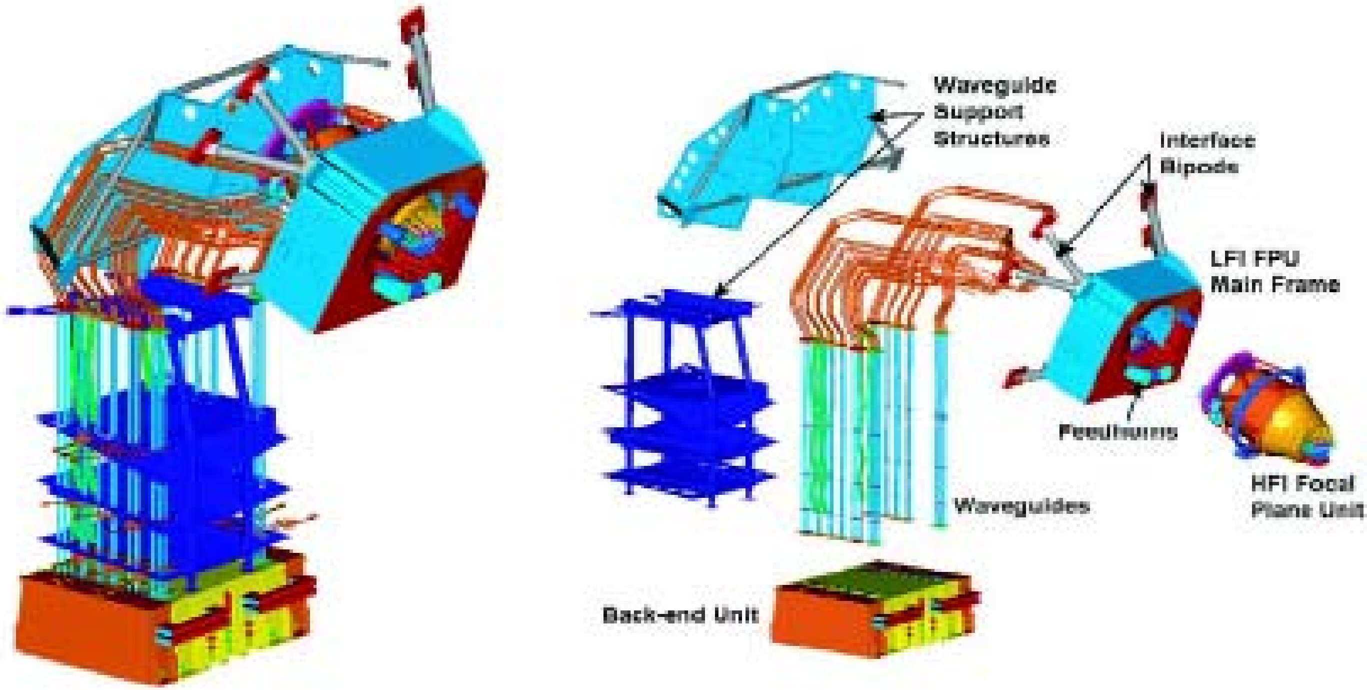

FIG. 1.5.—The LFI radiometer array assembly (left), with details of the front-end and back-end units (right). The front-ends are based on wide-band low-noise amplifiers, fed by corrugated feedhorns which collect the radiation from the telescope. The waveguides transport the amplified signals from the front-end (at 20 K) to the back-end (at 300 K). They are designed to meet simultaneously radiometric, thermal, and mechanical requirements, and are thermally linked to the three V-groove thermal shields of the *Planck* payload module. The back-end unit, located on top of the *Planck* service module, contains additional amplification as well as the detectors, and is interfaced to the data acquisition electronics. The HFI is inserted into and attached to the frame of the LFI focal-plane unit.

LFI view – II

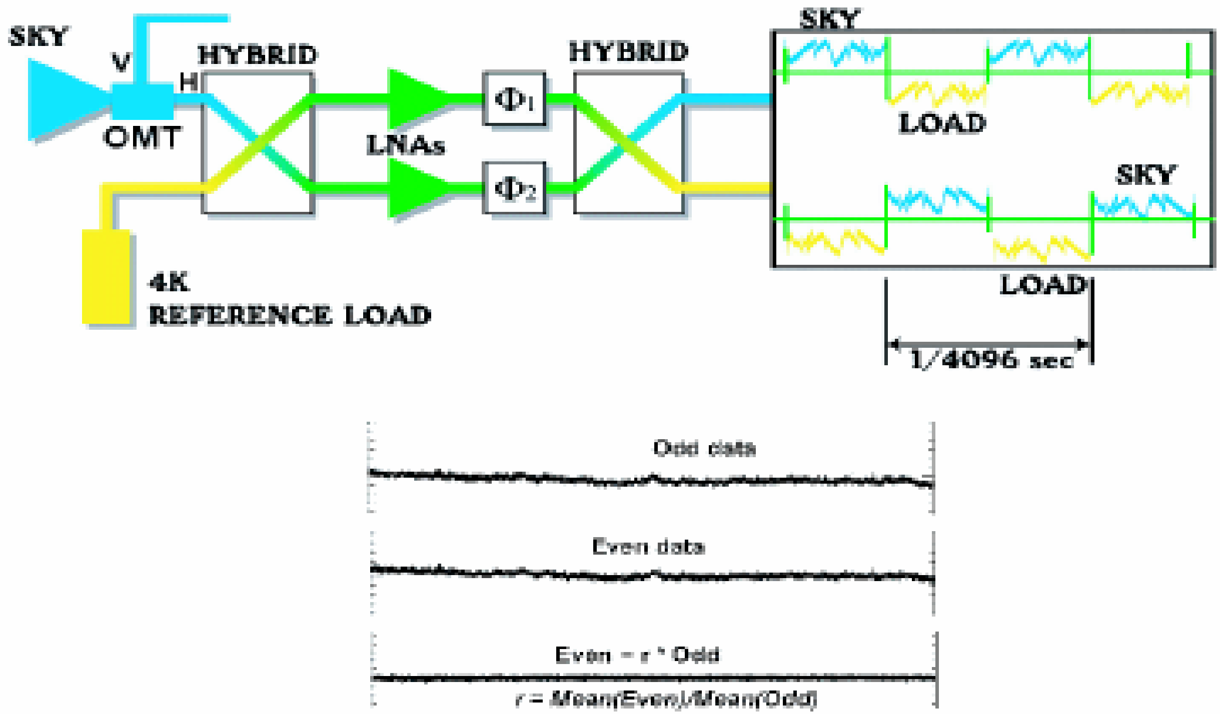

FIG. 1.6.—(*Top*) Schematic of the LFI front-end radiometer. The front-end unit is located at the focus of the *Planck* telescope, and comprises: dual profiled corrugated feed horns (Villa et al. 2002); low-loss (~ 0.2 dB), wide-band (> 20%) orthomode transducers; and radiometer front-end modules with hybrids, cryogenic low noise amplifiers, and phase switches. (*Bottom*) Measured radiometer output of the Elegant Breadboard model at 30 GHz. Shown are the signals from the two detector diodes ("odd" and "even" samples), which correspond to the sky and reference load, in which the noise is dominated by a non-white, $1/f$-type component. The radiometer design, however, is such that the $1/f$ component is highly correlated in the two diodes, so that the difference signal is extremely stable and insensitive to $1/f$ fluctuations.

HFI view – I

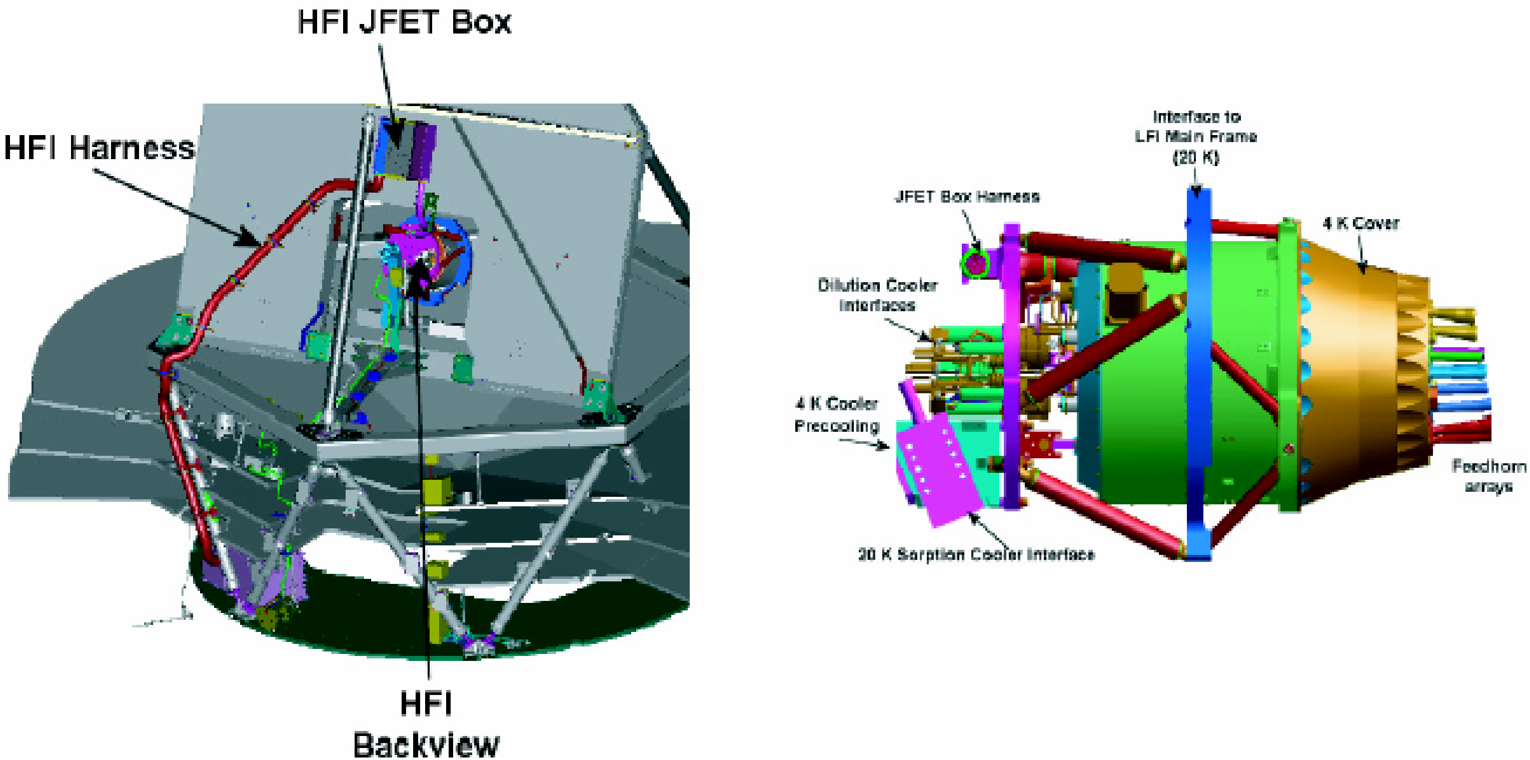

FIG 1.7.—The HFI focal plane unit. The telescope focuses radiation at the entrance of the corrugated horns. This flux is then filtered and detected by the low temperature (0.1 K) bolometers. The attachment points for the 20 K, 4 K, and 0.1 K coolers are shown, as well as the entrance point of the harness. The harness is shielded by a flexible bellows, and leads the bolometer signals to JFET-based circuits mounted in a box on the frame of the telescope. From this box, a second harness leads the signals to room-temperature electronics in the service module.

HFI view – II

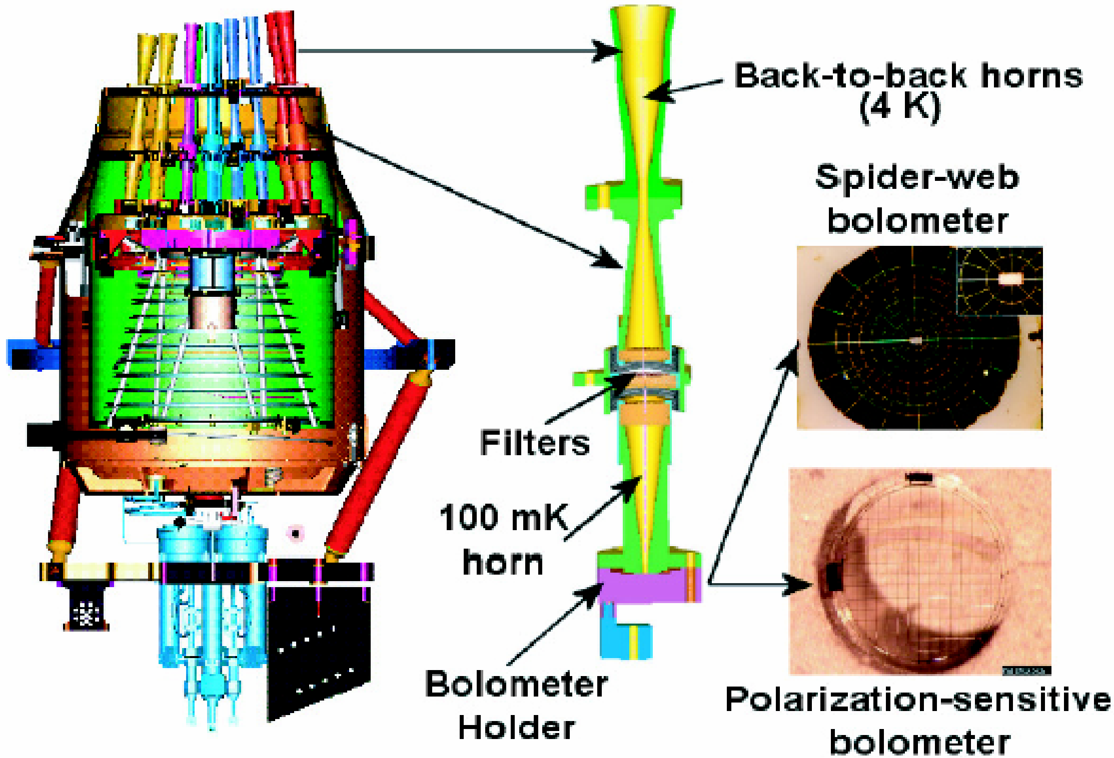

FIG 1.8.—Cutaway view of the HFI focal plane unit. Corrugated back-to-back feedhorns collect the radiation from the telescope and deliver it to the bolometer cavity through filters which determine the bandpass. The bolometers are of two kinds: (a) "spider-web" bolometers, which absorb radiation via a spider-web-like antenna; and (b) "polarisation-sensitive" bolometers, which absorb radiation in a pair of linear grids at right angles to each other. Each grid absorbs one linear polarization only. The absorbed radiant energy raises the temperature of a thermometer located either in the center of the spider-web, or at the edge of each linear grid.

Cooling system

V-groove radiators (to 60 K)

20 K H_2 sorption coolers (JPL)

4 K Stirling cooler (RAL/MMS)

0.1 K $^3He/^4He$ dilution cooler (CRTBT)

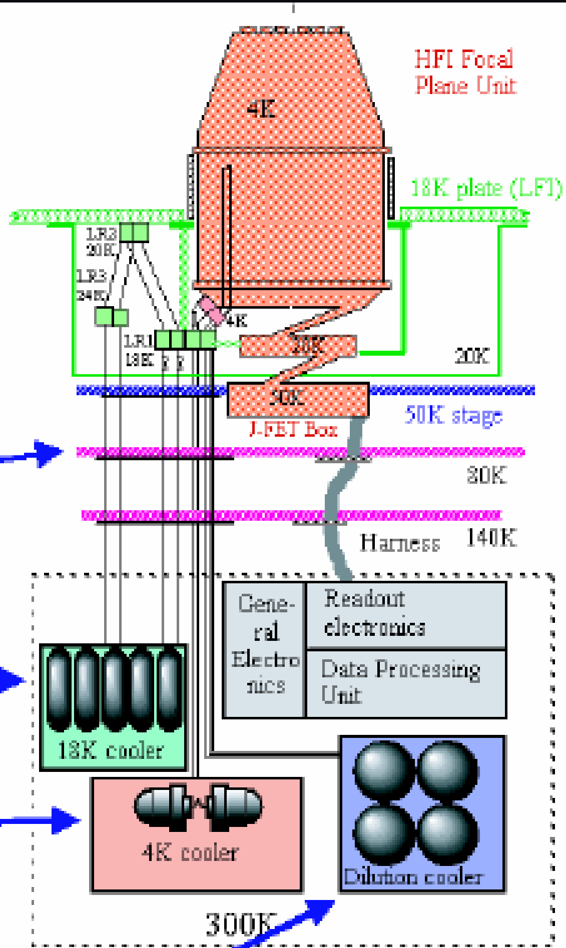

FIG 1.9.—The HFI cooling chain comprises the hydrogen sorption cooler providing 18 K, the closed-loop Joule-Thomson refrigerator providing 4 K, and a dilution refrigerator providing 0.1 K to the bolometers..

LFI Performance Goals[a]

Instrument Characteristic	Center Frequency [GHz]		
	30	44	70
InP HEMT Detector technology	MIC		MMIC
Detector temperature	20 K		
Cooling system	H_2 Sorption Cooler		
Number of feeds	2	3	6
Angular resolution [arcminutes FWHM]	33	24	14
Effective bandwidth [GHz]	6	8.8	14
Sensitivity [$\mathrm{mK\,Hz}^{-1/2}$]	0.17	0.20	0.27
System temperature [K]	7.5	12	21.5
Noise per 30′ reference pixel [μK]	6	6	6
$\Delta T/T$ Intensity [b] [10^{-6} μK/K]	2.0	2.7	4.7
$(\Delta T/T)$ Polarisation (Q and U) [b] [μK/K]	2.8	3.9	6.7
Maximum systematic error per pixel [μK]	< 3	< 3	< 3

[a] All subsystems are designed to reach or exceed the performances of this table.

[b] Average 1σ sensitivity per pixel (a square whose side is the FWHM extent of the beam), in thermodynamic temperature units, achievable after 2 full sky surveys (14 months).

HFI PERFORMANCE GOALS[a]

INSTRUMENT CHARACTERISTIC	CENTER FREQUENCY [GHz]					
	100	143	217	353	545	857
Spectral resolution $\nu/\Delta\nu$	3	3	3	3	3	3
Detector technology	Spider-web and polarisation-sensitive bolometers					
Detector temperature	0.1 K					
Cooling system	20 K Sorption Cooler + 4 K J-T + 0.1 K Dilution					
Number of spider-web bolometers	0	4	4	4	4	4
Number of polarisation-sensitive bolometers	8	8	8	8	0	0
Angular resolution [FWHM arcminutes]	9.5	7.1	5.0	5.0	5.0	5.0
Detector Noise-Equivalent Temperature [μKs$^{0.5}$]	50	62	91	277	1998	91000
$\Delta T/T$ Intensity [b] [$10^{-6}\mu$K/K]	2.5	2.2	4.8	14.7	147	6700
$\Delta T/T$ Polarisation (U and Q)[b] [$10^{-6}\mu$K/K]	4.0	4.2	9.8	29.8	...	...
Sensitivity to unresolved sources [mJy]	12.0	10.2	14.3	27	43	49
ySZ per FOV [10^{-6}]	1.6	2.1	615	6.5	26	605

[a] Goal sensitivities. All subsystems have been designed to reach or exceed the performances of this table, which are expected to be achieved in orbit. Sensitivity requirements are a factor of two worse, and would still achieve the core scientific objectives of the mission.

[b] Average 1σ sensitivity per pixel (a square whose side is the FWHM extent of the beam), in thermodynamic temperature units, achievable after 2 full sky surveys (14 months).

Summary of Planck Instrument Characteristics

Instrument Characteristic	LFI			HFI					
Detector Technology	HEMT arrays			Bolometer arrays					
Center Frequency [GHz]	30	44	70	100	143	217	353	545	857
Bandwidth ($\Delta\nu/\nu$)	0.2	0.2	0.2	0.33	0.33	0.33	0.33	0.33	0.33
Angular Resolution (arcmin)	33	24	14	10	7.1	5.0	5.0	5.0	5.0
$\Delta T/T$ per pixel (Stokes I)[a]	2.0	2.7	4.7	2.5	2.2	4.8	14.7	147	6700
$\Delta T/T$ per pixel (Stokes Q &U)[a]	2.8	3.9	6.7	4.0	4.2	9.8	29.8	...	...

[a] Goal (in μK/K) for 14 months integration, 1σ, for square pixels whose sides are given in the row "Angular Resolution".

Planck telescope

Optical configuration

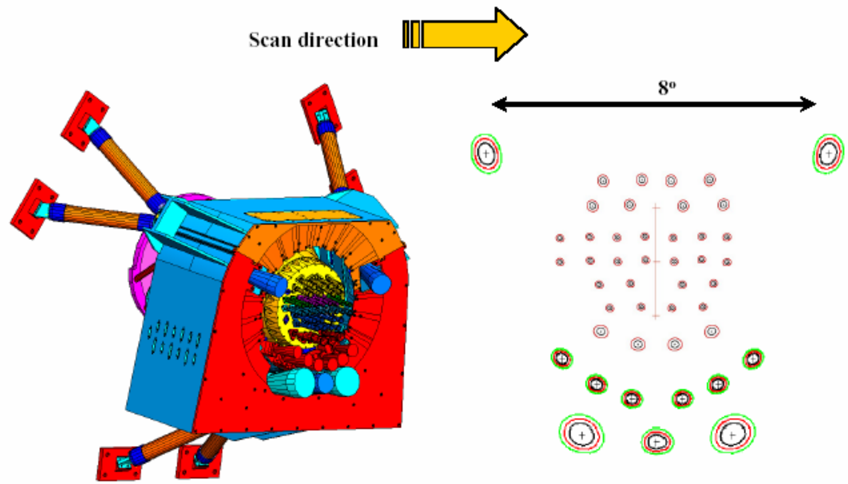

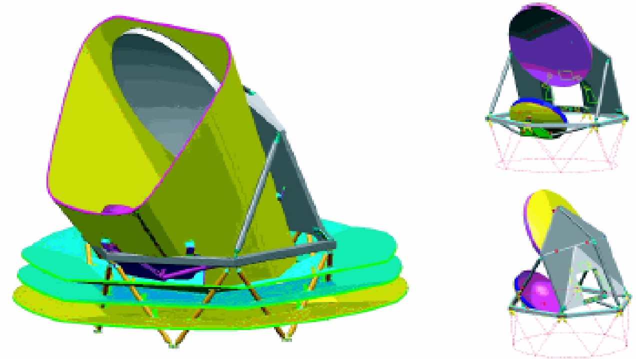

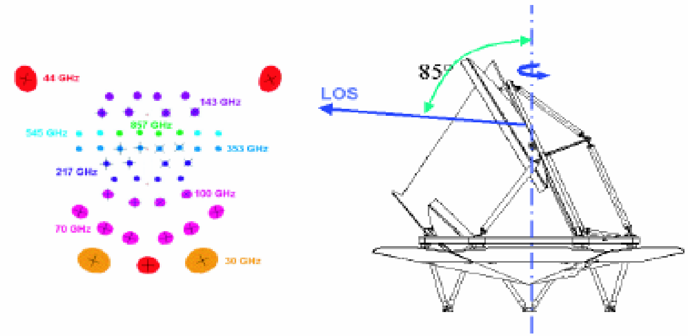

FIG 1.10.—The *Planck* optical system, including the telescope baffle and V-grooves, which provide straylight control in addition to thermal isolation. The attachment points for the LFI focal plane unit can be seen in the upper right. The reflectors are under manufacture by Astrium Gmbh (Friedrichshafen) together with the telescope support structure (under manufacture by Contraves, Zürich). Views courtesy of Alcatel Space (Cannes). The telescope field-of-view is offset from the spin axis of the satellite by an angle of 85°. The footprint of the field-of-view on the sky is seen in the lower left; it covers about 8° on the sky at its widest. Each spot corresponds to the 20 dB contour of the radiation pattern; the ellipticities seen are also representative of the shape of the beam at full-width-half-maximum. The black crosses indicate the orientation of the pairs of linearly polarised detectors within each horn. The field-of-view sweeps the sky in the horizontal direction in this diagram.

TELESCOPE MIRROR PARAMETERS

Parameter	Primary mirror	Secondary mirror
Radius of curvature of the ellipsoid [mm]	1440.000	−643.972
Conic constant	−0.86940	−0.215424
Elliptical perimeter [mm]	1555.98 × 1886.79	1050.96 × 1104.39
Reflectors centre to major axis offset [mm]	1038.85	−309.52

Launch & orbit Lissajous around L2

New transfer phase shorter

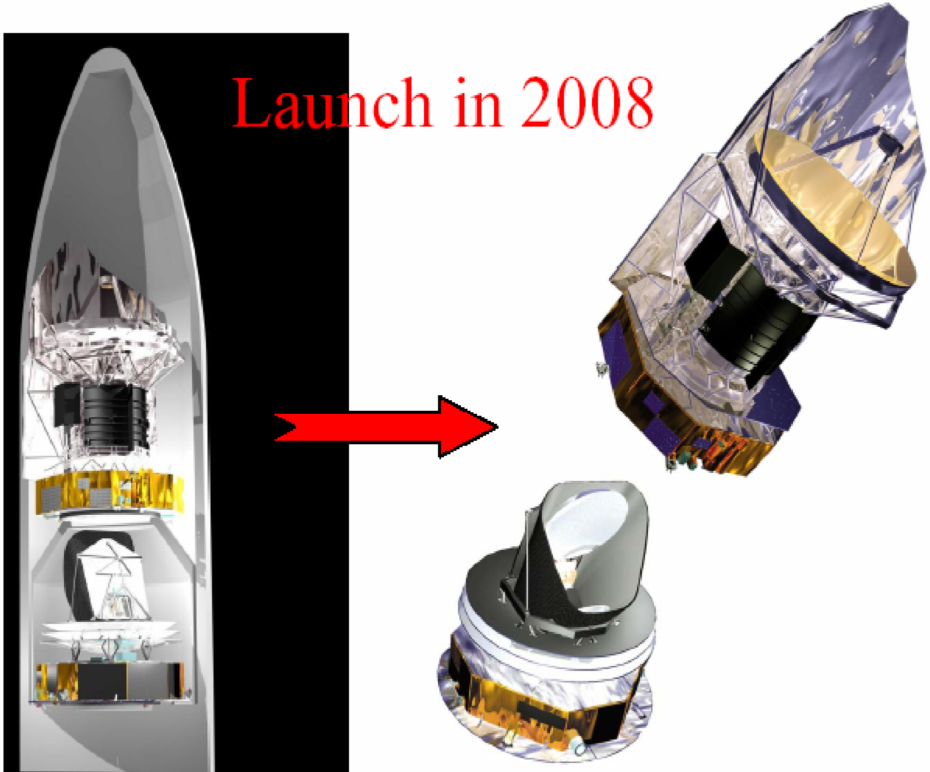

FIG 1.11.— *Planck* and *Herschel* ready for launch under the Ariane 5 fairing. The two satellites separate just after launch and proceed independently to their final orbits. View courtesy of Alcatel Space (Cannes).

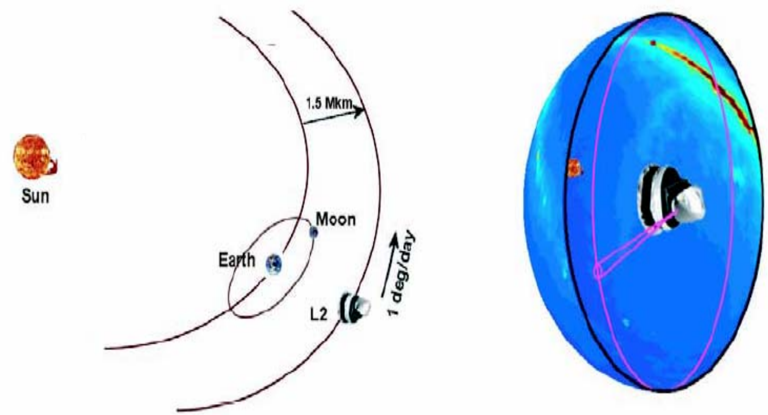

FIG 1.4.—*Planck* orbit at the 2nd Lagrangian point of the Earth-Sun system (L_2). The spin axis is pointed near the Sun, with the solar panel shading the payload, and the telescope sweeps the sky in large circles at 1 rpm.

Main differences between Planck & WMAP – I

- WMAP: 2 telescopes, sky-sky difference, radiometers only
- *Planck:* 1 telescope, sky-sky difference & sky-reference difference, radiometers & bolometers
- Cryogenics much more aggressive for *Planck* in order to
  - achieve sensitivity
  - bolometer work condition
  - radiometer 4K reference load temperature
- WMAP "intrinsically" more stable
- Planck stability largely relies on thermal stability

Main differences between Planck & WMAP – II

- WMAP
- 23, 33, 41, 61, 94 GHz
- 0.88, 0.66, 0.51, 0.35, 0.22 deg (beam solid angle)$^{1/2}$ ~ FWHM
- 20-30 uK on 20' side

- *Planck*
- 30, 44, 70 GHz (LFI), 100, 143, 217, 353, 545, 857 GHz (HFI)

→ HFI coverage of high frequencies !

- 35, 26, 13, 9.2, 7.1, 5, 5, 5, 5 arcmin (FWHM)
- 8, 8, 8, 2.1, 1.4, 2.2, 6.7, 67, 3050 uK on 30' side

→ from 3 to 10 times sensitivity improvement

→ better resolution, better frequency coverage

→ essentially cosmic variance / astrophysical limited in T

Main differences betwen Planck & WMAP – III

PLANCK – LFI CALIBRATORS FOR GROUND TESTING

Planck-LFI ground tests required to power the feedhorns with a black-body signal at cryogenic temperature, to mimic the sky signal. Results from calibrations are strongly depending on ‘blackness’ of this source (and on modelling abilities).

LFI will make also “absolute” measures, within 4K reference loads sensitivity

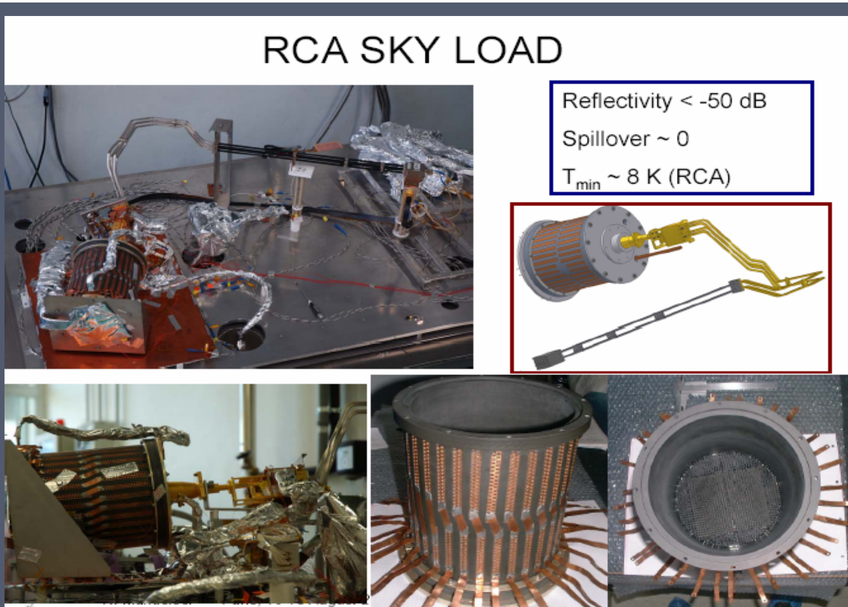

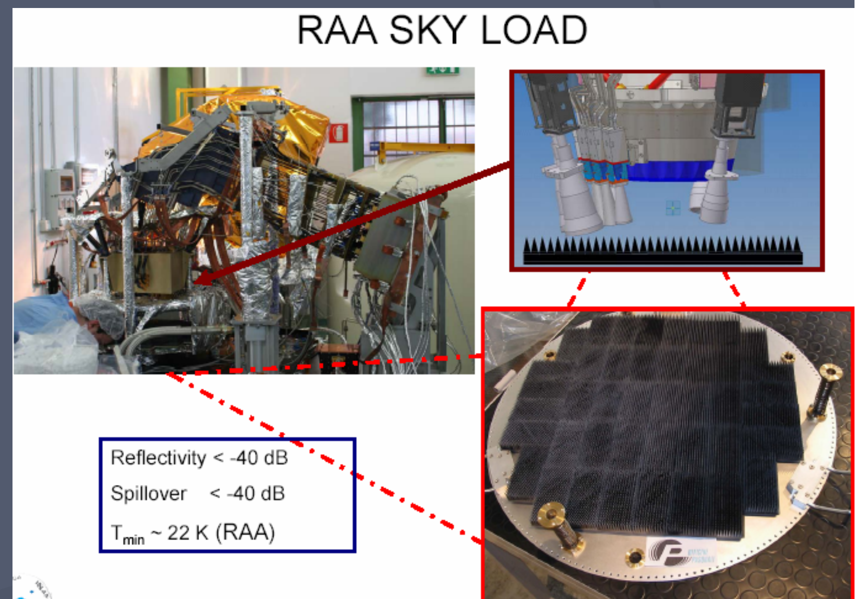

APS & corresponding error

$$\frac{\delta T}{T}(\hat{\gamma}) = \sum_{\ell=1}^{\infty} \sum_{m=-\ell}^{\ell} a_{\ell m} Y_{\ell m}(\hat{\gamma}) \, , \qquad (7)$$

where $\hat{\gamma}$ is the observation unit direction vector.

Isotropy around the observer $\longrightarrow$ $a_{\ell m}$ should have zero mean, $\langle a_{\ell m} \rangle = 0$, and variance C_ℓ

$\vartheta/\mathrm{deg} = 180/\ell$

Dimensionless temperature fluctuation $\delta T/T$

(Physical) temperature fluctuation δT

Given the CMB monopole temperature = 2.725 K

(Mather J.C., Fixsen D.J., Shafer R.A., Mosier C., Wilkinson D.T., 1999, ApJ, 512, 511)

the dimensionless C_ℓ will be $\simeq 7.4 \times 10^{12}$ smaller than the C_ℓ expressed in terms of μK^2 (in thermodynamic temperature).

$$C_\ell \equiv \langle| a^2_{\ell m} |\rangle = \frac{1}{2\ell+1}\sum_m a^2_{\ell m}$$
$$= 2\pi \int d\cos\theta C(\theta) P_\ell(\cos\theta) \quad (8)$$

$$C(\theta) \equiv \langle \frac{\delta T}{T}(\hat{\gamma}_1)\frac{\delta T}{T}(\hat{\gamma}_2)\rangle$$
$$= \frac{1}{4\pi}\sum_l (2l+1)\, C_\ell\, P_\ell(\cos\theta)\,; \quad (9)$$

here $\cos\theta = \hat{\gamma}_1 \cdot \hat{\gamma}_2$ and P_ℓ is the Legendre polynomial.

Since each given anisotropy field is a single realization of a stochastic process, it may be different from the average over the ensemble of all possible realizations of the given (true) model with given parameters. This translates into the fact that the $a_{\ell m}$ coefficients are random variables (possibly following a Gaussian distribution), at a given ℓ, and therefore their variance, C_ℓ, is χ^2 distributed with $2\ell+1$ degrees of freedom. The relative variance δC_ℓ on C_ℓ is equal to $\sqrt{2/(2\ell+1)}$ which is quite relevant at low ℓ because of the relatively small number of available modes.

→ "COSMIC VARIANCE": it defines the ultimate limit on the accuracy at which a given model defined by an appropriate set of parameters can be constrained by the angular power spectrum.

Another similar variance in anisotropy experiments is related to the SKY COVERAGE. This variance depends on the observed sky fraction, $f_{\rm sky}$.

At the largest multipoles achievable with a given experiment the most relevant uncertainties are related to the EXPERIMENT RESOLUTION and SENSITIVITY.

→ OVERALL UNCERTAINTY: (Knox L., 1995, Phys. Rev. D., 48, 3502)

$$\frac{\delta C_\ell}{C_\ell} = \sqrt{\frac{2}{f_{\rm sky}(2\ell+1)}}\left[1+\frac{A\sigma^2}{NC_\ell W_\ell}\right], \qquad (10)$$

A=size of the surveyed area, σ=rms noise per pixel, N=total number of observed pixel, W_ℓ=beam window function.

For a symmetric Gaussian beam →

$W_\ell = \exp(-\ell(\ell+1)\sigma_{\rm B}^2)$

where $\sigma_{\rm B} = {\rm FWHM}/\sqrt{8\ln 2}$.

TT, EE, BB, TE modes

$$\Delta T = \sum_{\ell m} a_{\ell m} Y_{\ell m}(\theta, \phi)$$

$$C_\ell^T = \langle |a_{\ell m}|^2 \rangle$$

$$(\Delta T_\ell)^2 = \frac{1}{2\pi} \ell(\ell+1) C_\ell^T$$

$$P_E = \sum_{\ell \geq 2} \sum_{|m| \leq \ell} \sqrt{\frac{(\ell-2)!}{(\ell+2)!}} a_{\ell m}^E Y_{\ell m}, \quad P_B = \sum_{\ell \geq 2} \sum_{|m| \leq \ell} \sqrt{\frac{(\ell-2)!}{(\ell+2)!}} a_{\ell m}^B Y_{\ell m}$$

$$\langle a_{\ell m}^{Y*} a_{\ell' m'}^{Y'} \rangle = C_\ell^{YY'} \delta_{\ell \ell'} \delta_{m m'}$$

Rotational invariance

$$(\Delta C_\ell^E)^2 \simeq \frac{2}{(2\ell+1) f_{\rm sky}} (C_\ell^E + w_P^{-1} W_\ell^{-2})^2$$

$$W_\ell = \exp[-\ell(\ell+1)/(2\ell_{\rm beam}^2)]$$

$$\ell_{\rm beam} = \sqrt{8 \ln 2} (\theta_{\rm FWHM})^{-1}$$

$$w_T = (\sigma_{{\rm p},T} \theta_{\rm FWHM})^{-2} \quad w_P = (\sigma_{{\rm p},P} \theta_{\rm FWHM})^{-2}$$

$$(\Delta C_\ell^{TE})^2 \simeq \frac{1}{(2\ell+1) f_{\rm sky}} [(C_\ell^T + w_T^{-1} W_\ell^{-2})(C_\ell^E + w_P^{-1} W_\ell^{-2}) + (C_\ell^{TE})^2]$$

Beam (& then window function) reconstruction in flight through planet transits

TABLE I

Input parameters of symmetric and elliptical beam for the considered planet transits. ϵ is the angle between the ellipse principal axis and the axis x_T of the telescope rf. σ =FWHM/$\sqrt{8\ln 2}$ gives the beam width, r is the ratio between the major and minor ellipse axes, r_k is related to the planet brightness temperature (see Section 3.1), and x_T^* and y_T^* are the beam centre coordinates in the telescope rf (see also the text).

Input values

Event	ϵ (deg) circ.	ϵ (deg) ellipt.	σ (arcmin)	r – circ.	r – ellipt.	r_k ‡ (mK)	$x_T^* \cdot 10^2$ –	$y_T^* \cdot 10^2$ –
Jupiter (I)						35.8297		
Jupiter (II)						35.4743		
Saturn (I)	–	0	14.01381	1	1.3	7.8543	−5.76035	7.91971
Saturn (II)						7.8229		

‡ The value r_k depends on the distance between the spacecraft and the planet which slightly varies between different pointing events.

Event	ϵ (deg)	σ (arcmin)	r –	r_k (mK)	$x_T^* \cdot 10^2$ –	$y_T^* \cdot 10^2$ –	χ^2/ DOF –
Elliptical beam: effect of 1′ pointing error							
Jupiter (I)	1.65 ±0.15	14.2003 ±0.0089	1.2723 ±0.0016	35.382 ±0.031	−5.7519 ±0.0004	7.9243 ±0.0003	1.3858
Saturn (I)	−2.57 ±0.57	13.870 ±0.042	1.3374 ±0.0080	7.937 ±0.034	−5.7679 ±0.0020	7.9263 ±0.0014	1.016
Elliptical beam: effect of neglecting spacecraft motion							
Jupiter (I)	0.21 ±0.14	14.0697 ±0.0089	1.2904 ±0.0016	35.584 ±0.032	−5.7602 ±0.0004	7.9198 ±0.0003	0.999
Saturn (I)	−0.40 ±0.69	14.053 ±0.043	1.2964 ±0.0078	7.782 ±0.033	−5.7661 ±0.0020	7.9200 ±0.0015	0.999
Alcatel case1 beam: fit with circular beam – realistic simple scanning strategy, $\alpha = 80°$							
Jupiter (I)	–	14.9583 ±0.0089	–	31.106 ±0.026	−5.5751 ±0.0003	7.2991 ±0.0004	8.094
Alcatel case1 beam: fit with elliptical beam – realistic simple scanning strategy, $\alpha = 80°$							
Jupiter (I)	69.03 ±0.11	15.0102 ±0.0087	1.3602 ±0.0016	31.360 ±0.026	−5.5756 ±0.0003	7.3001 ±0.0004	1.232
Above elliptical beam: fit with elliptical beam – baseline simple scanning strategy, $\alpha = 85°$							
Jupiter (I)	68.99 ±0.10	15.0209 ±0.0083	1.3590 ±0.0015	32.241 ±0.025	−5.5792 ±0.0003	7.2794 ±0.0004	0.997

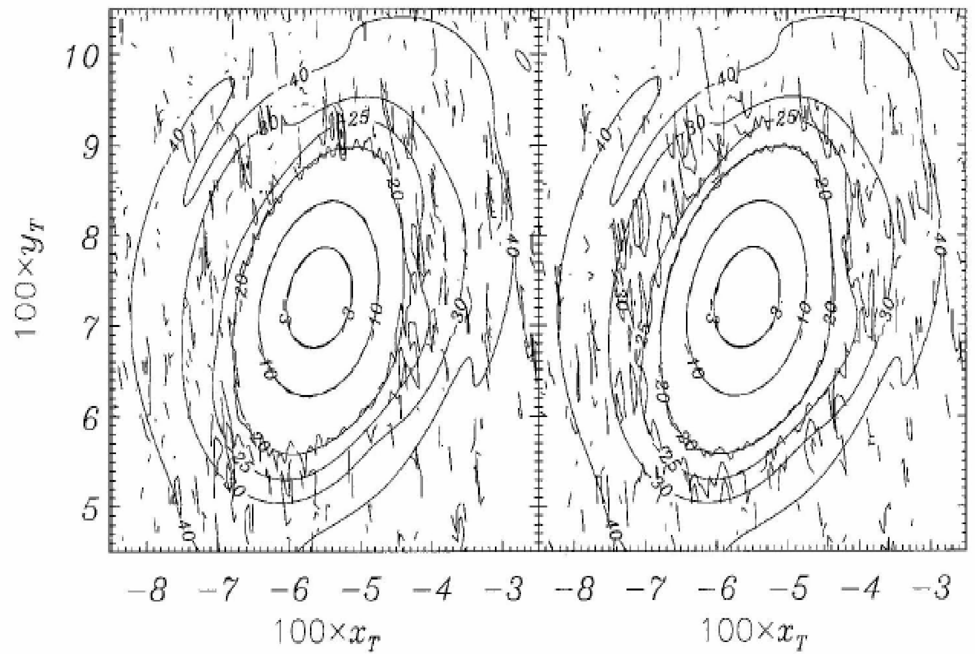

Figure 3. Left panel: contour plot (in dB) of one of the two beams at 30 GHz as simulated through the GRASP8 code for the Alcatel case1 telescope configuration and as reconstructed in flight by using a single Jupiter transit and the sensitivity of the two radiometers connected to the beam. At response levels less than $\simeq -20$ dB the signal to noise ratio of the beam reconstruction is too low and the contours are no longer clearly defined. Right panel: the same as the left panel, but by using three Jupiter transits and by taking advantage from the symmetry of the two "conjugate" 30 GHz beams. In this case the contours are quite well defined up to a response level of about −25 dB. (The beam shape is here reported on the plane x_T, y_T of the telescope rf; note that $x_T = \sin\theta\cos\phi$ and $y_T = \sin\theta\sin\phi$ are dimensionless, but correspond essentially to angular sizes expressed in rad.)

Experimental Astronomy **12:** 87–106, 2001.

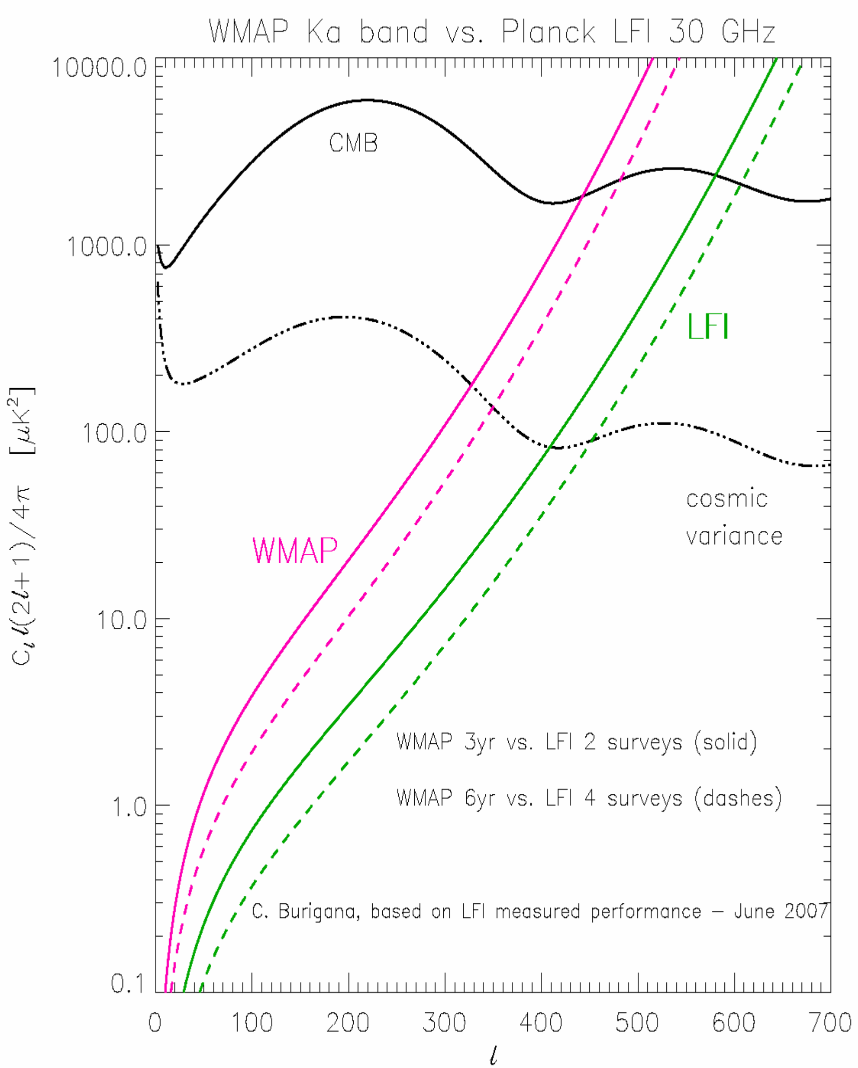
WMAP Ka band vs. Planck LFI 30 GHz
CMB
LFI
WMAP
cosmic variance
WMAP 3yr vs. LFI 2 surveys (solid)
WMAP 6yr vs. LFI 4 surveys (dashes)
C. Burigana, based on LFI measured performance – June 2007
$C_\ell \, \ell(2\ell+1)/4\pi \quad [\mu K^2]$
ℓ

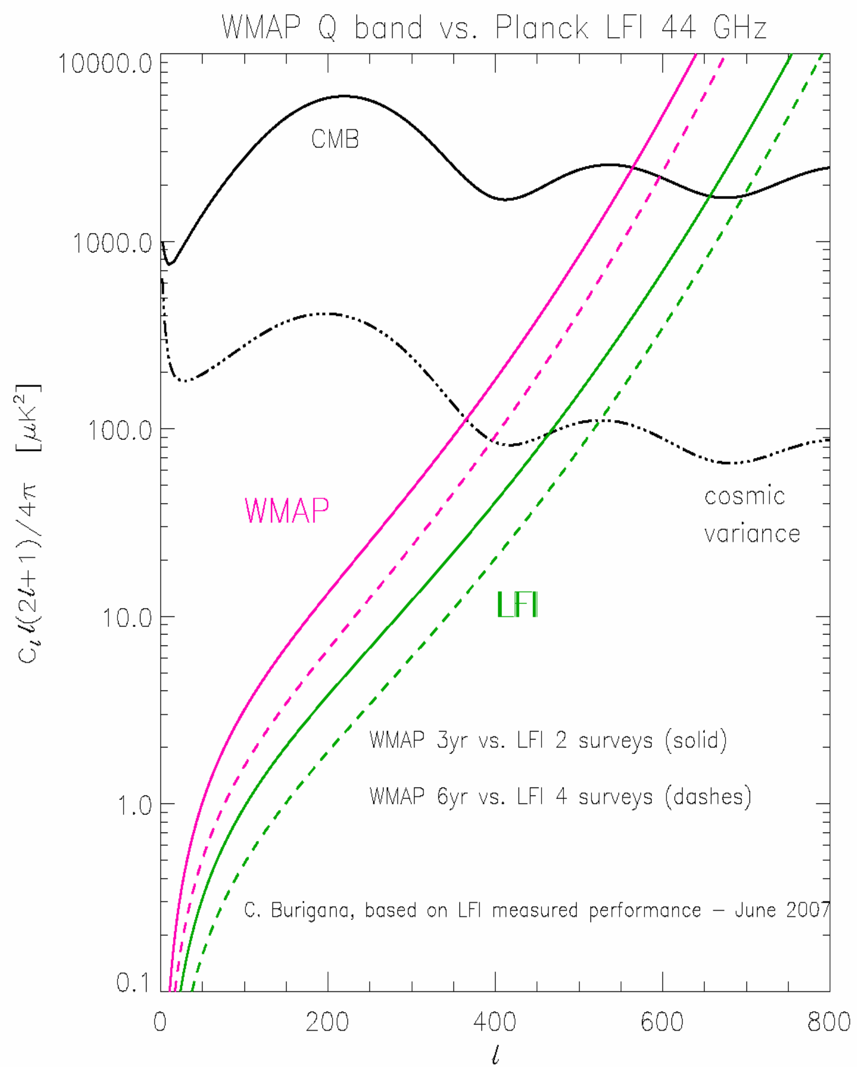
WMAP Q band vs. Planck LFI 44 GHz
CMB
WMAP
LFI
cosmic variance
WMAP 3yr vs. LFI 2 surveys (solid)
WMAP 6yr vs. LFI 4 surveys (dashes)
C. Burigana, based on LFI measured performance – June 2007
$C_\ell \, \ell(2\ell+1)/4\pi \quad [\mu K^2]$
ℓ

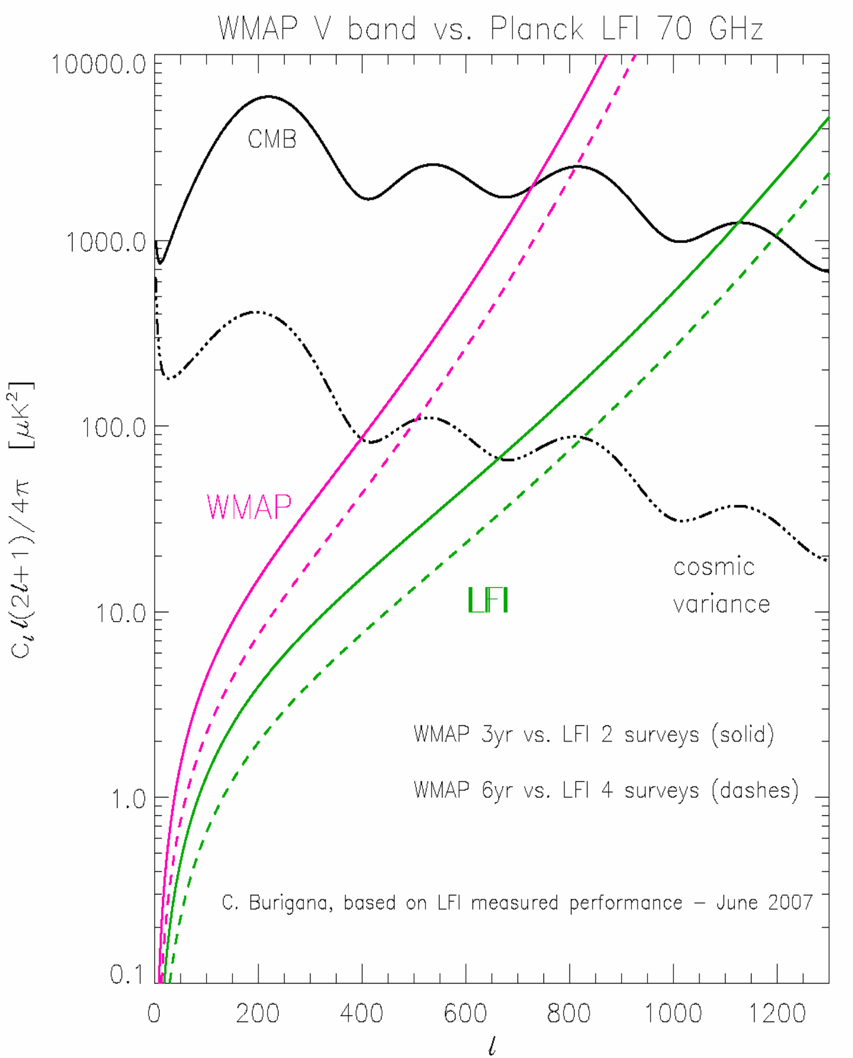
WMAP V band vs. Planck LFI 70 GHz
10000.0
1000.0
100.0
10.0
1.0
0.1
$C_\ell\, \ell(2\ell+1)/4\pi \quad [\mu K^2]$
CMB
WMAP
LFI
cosmic variance
WMAP 3yr vs. LFI 2 surveys (solid)
WMAP 6yr vs. LFI 4 surveys (dashes)
C. Burigana, based on LFI measured performance – June 2007
0
200
400
600
800
1000
1200
ℓ

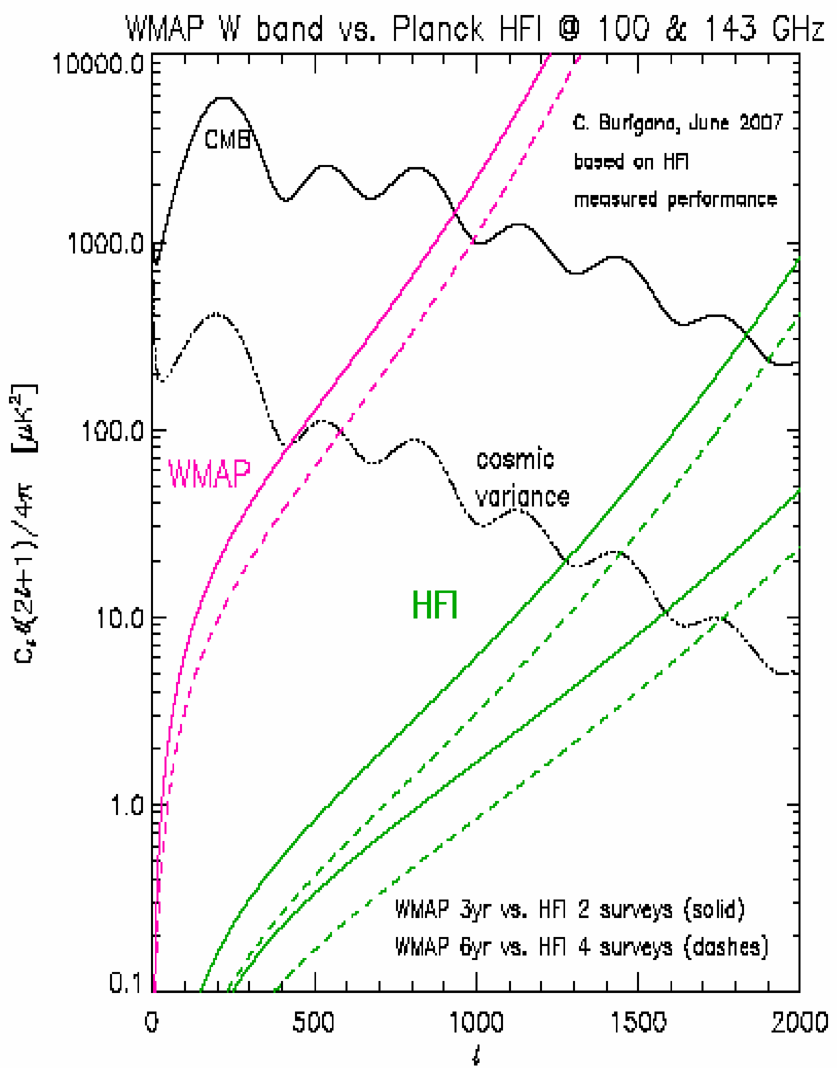
WMAP W band vs. Planck HFI @ 100 & 143 GHz
10000.0
1000.0
100.0
10.0
1.0
0.1
$C_\ell\, \ell(2\ell+1)/4\pi \quad [\mu K^2]$
CMB
C. Burigana, June 2007
based on HFI
measured performance
WMAP
cosmic variance
HFI
WMAP 3yr vs. HFI 2 surveys (solid)
WMAP 6yr vs. HFI 4 surveys (dashes)
0
500
1000
1500
2000
ℓ

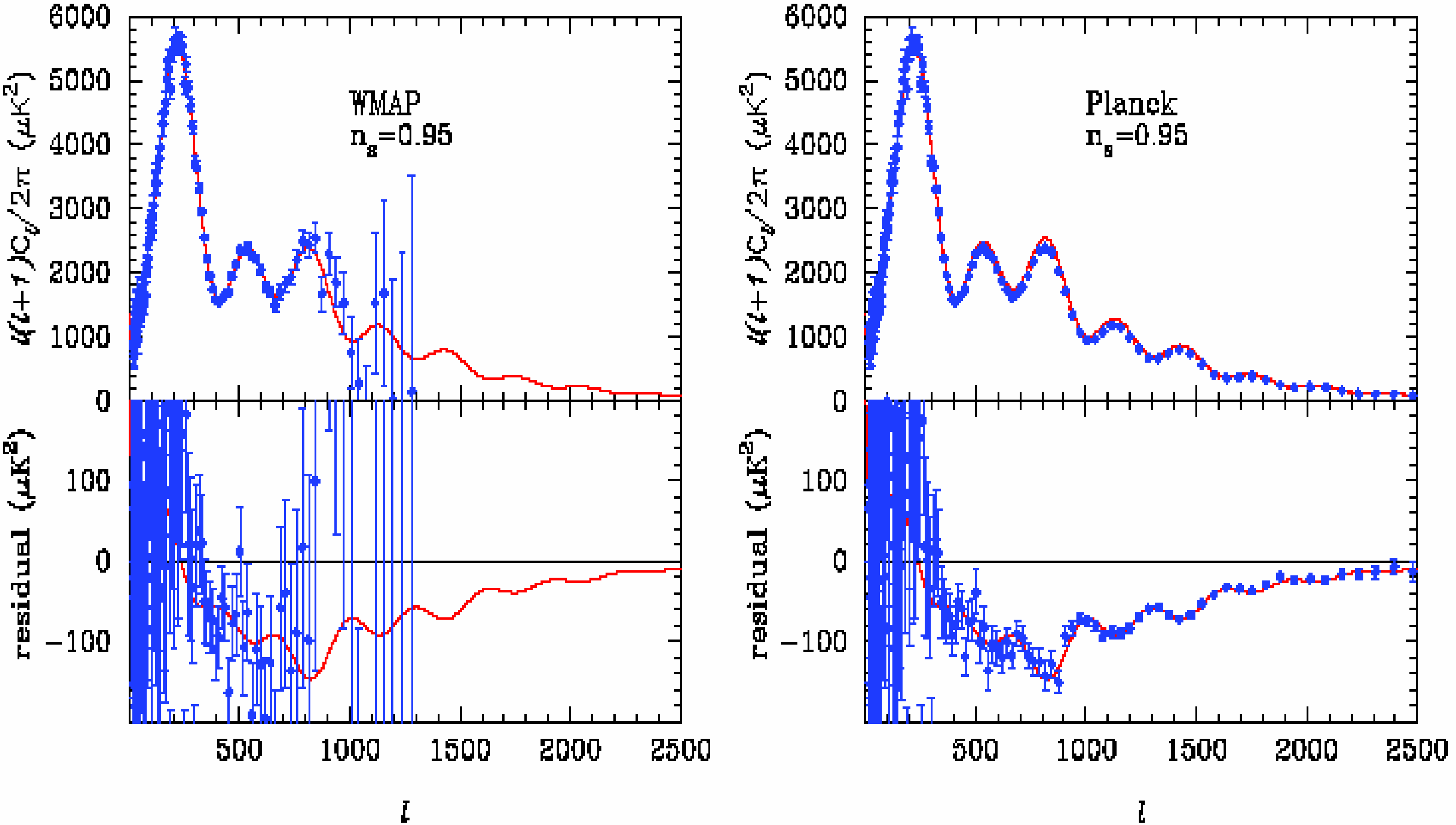

FIG 2.11.—The solid lines in the upper panels of these figures show the power spectrum of the concordance ΛCDM model with an exactly scale invariant power spectrum, $n_S = 1$. The points, on the other hand, have been generated from a model with $n_S = 0.95$ but otherwise identical parameters. The lower panels show the residuals between the points and the $n_S = 1$ model, and the solid lines show the theoretical expectation for these residuals. The left and right plots show simulations for *WMAP* and *Planck*, respectively.

TE (cross) modes

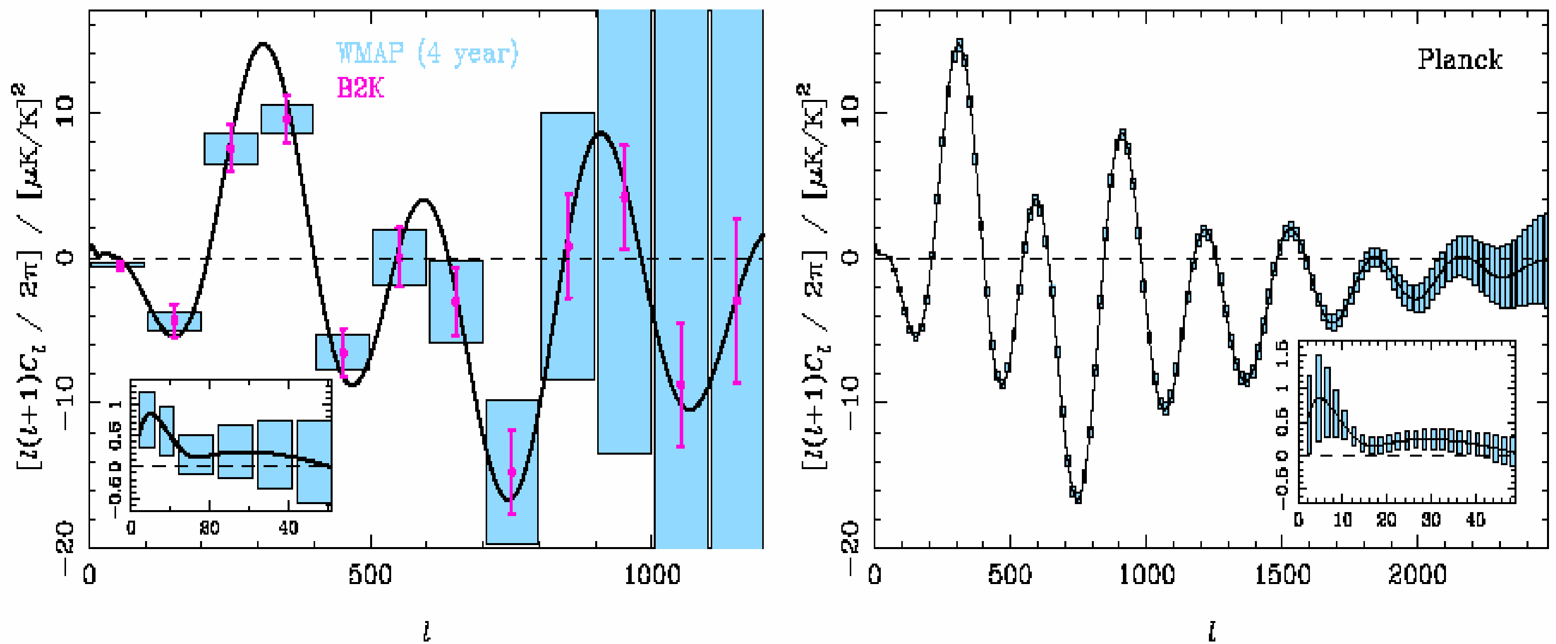

FIG 2.13.—Forecasts for the $\pm 1\sigma$ errors on the temperature-polarization cross-correlation power spectrum C_ℓ^{TE} in a ΛCDM model (with $r = 0.1$ and $\tau = 0.17$) from *WMAP* (4 years of observation) and BOOMERanG2K (left) and *Planck* (right). In the left-hand plot, flat band powers are estimated with $\Delta\ell = 100$ for both experiments for ease of comparison. The inset shows the *WMAP* forecasts on large angular scales with a finer $\Delta\ell$ resolution. For *Planck*, flat band powers are estimated with $\Delta\ell = 20$ in the main plot, but with $\Delta\ell = 2$ in the inset on large scales.

EE polarization modes

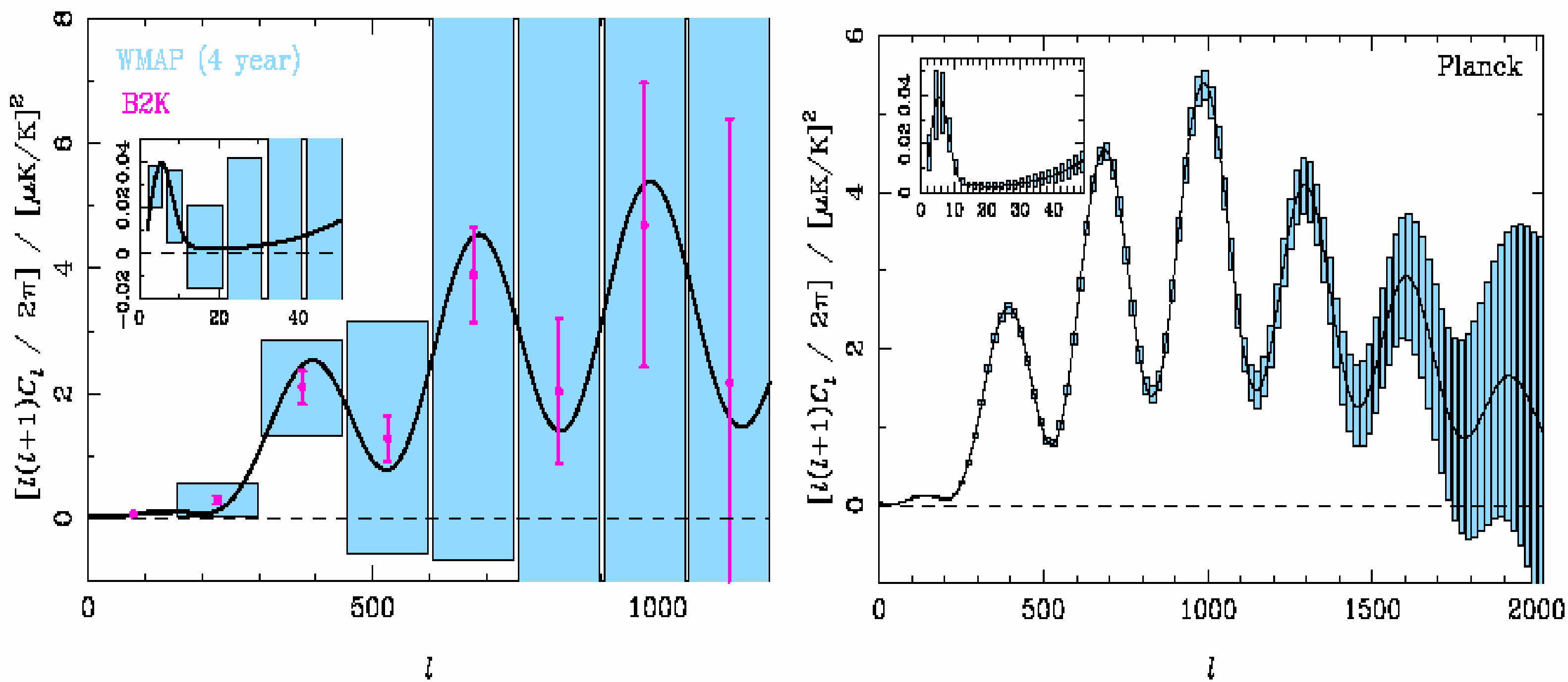

FIG 2.14.—Forecasts for the $\pm 1\sigma$ errors on the E-mode polarization power spectrum C_ℓ^E from *WMAP* and B2K (left) and *Planck* (right). The cosmological model, and the assumptions about instrument characteristics, are the same as in Figure 2.13. For *WMAP* and B2K, flat band powers are estimated with $\Delta\ell = 150$ (with finer resolution on large scales for *WMAP* in the inset). For *Planck* we have used the same ℓ-resolution as in Figure 2.13.

BB mode detection

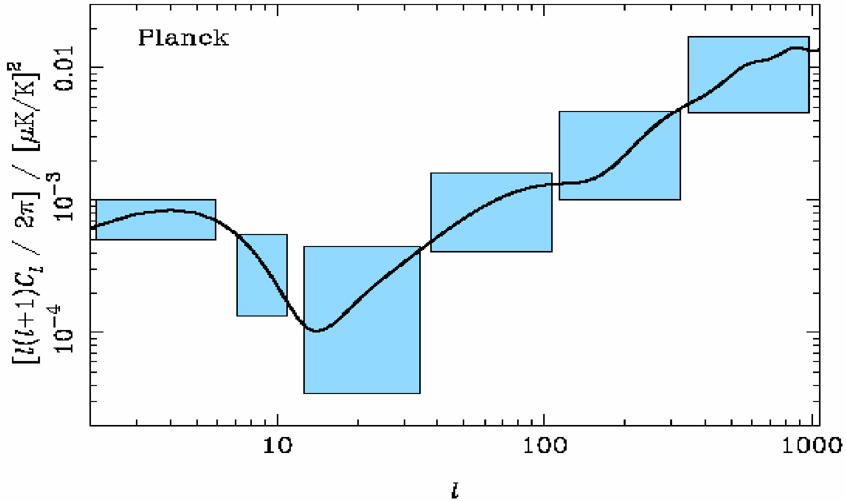

FIG 2.17.—Forecasts for the $\pm1\sigma$ errors on the B-mode polarization power spectrum C_ℓ^B from *Planck* (for $r = 0.1$ and $\tau = 0.17$). Above $\ell \sim 150$ the primary spectrum is swamped by weak gravitational lensing of the E-polarization produced by the dominant scalar perturbations. The cosmological model, and the assumptions about instrument characteristics, are the same as in Figure 2.13.

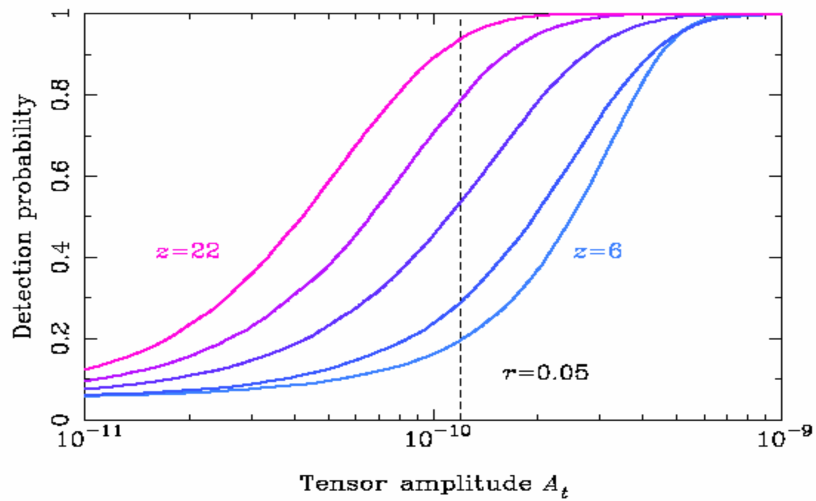

FIG 2.16.—The probability of detecting B-mode polarization at 95% confidence as a function of $A_{\rm T}$, the amplitude of the primordial tensor power spectrum (assumed scale-invariant), for *Planck* observations using 65% of the sky. The curves correspond to different assumed epochs of (instantaneous) reionization: $z = 6$, 10, 14, 18 and 22. The dashed line corresponds to a tensor-to-scalar ratio $r = 0.05$ for the best-fit scalar normalisation, $A_{\rm S} = 2.7 \times 10^{-9}$, from the one-year *WMAP* observations.

Generally …

- Planck could in principle detect primordial B modes for T/S above ~ 0.1 – (some × 0.01)
- B mode induced by lensing @ high l will be identified

- In order to get info on B modes <u>down to low</u> T/S values (B-Pol goal) and on details of cosmological reionization we need extreme sensitivity and excellent separation/subtraction of foregrounds

(at few % accuracy level @ map level

$\approx$ some $\times 10^4$ at APS level) … see the next!

Systematics &
Scanning Strategy

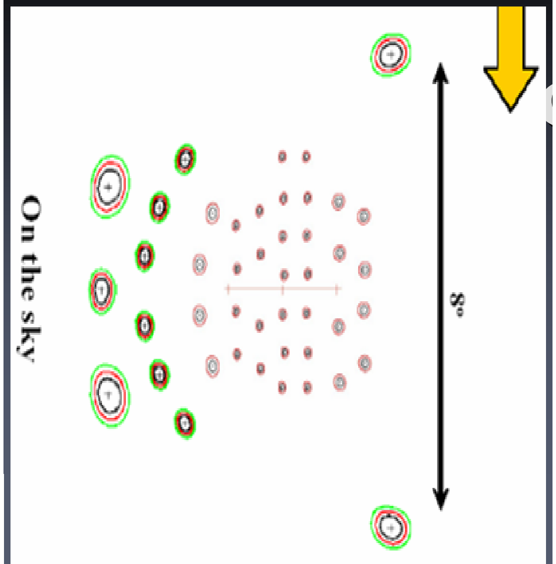

Observing strategy

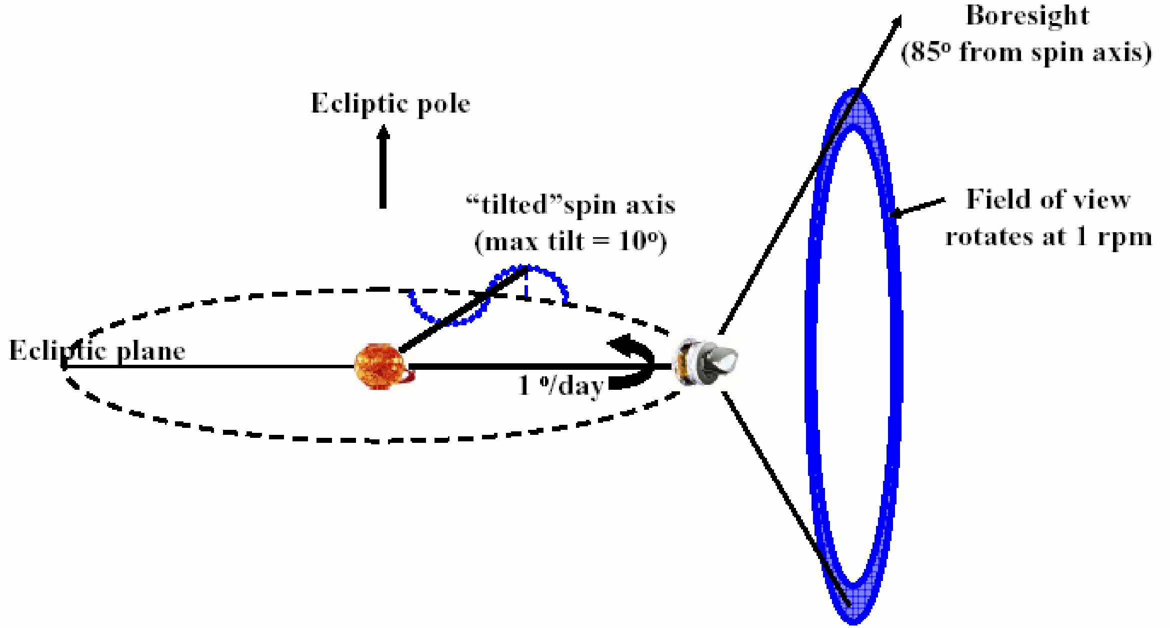

<u>Scanning Strategy (SS):</u> ***kind of SS and SS parameters optimized within constraints to achieve the best scientific output.***

<u>Criteria:</u>

no or minimal systematics, maximization of sky coverage (all-sky), optimization of data analysis:

<u>Nominal</u> or <u>Slow</u> (P=6 months=P_orbit) <u>Spin Axis Precessions (Cycloids)</u>

- 1 parameter: angle between telescope LOS & spin axis = 85º
  - This in order to allow a good destriping with all beams for any SS (90º is degenerate)
- 2 parameter: spin axis spacing between repointings: 2'/48 min
  - ~Nyquist for HFI
  - # manoevres safely enough for 4 surveys
- Cycloids with semi-aperture≥7.5 deg allow all-sky coverage
- Cycloids can be "adjusted" in initial conditions to optimize some data analysis procedure, e.g.:
  - Change of the orientations of the same beam in the subsequent surveys to monitor polarization
  - Optimization of day-by-day LFI calibration with dipole
  - Etc.
- Possible con of cycloids vs nominal:
  - External straylight
- Pro of cycloids vs nominal:
  - better removal of 1/f noise through map-maker/destriper

Straylight

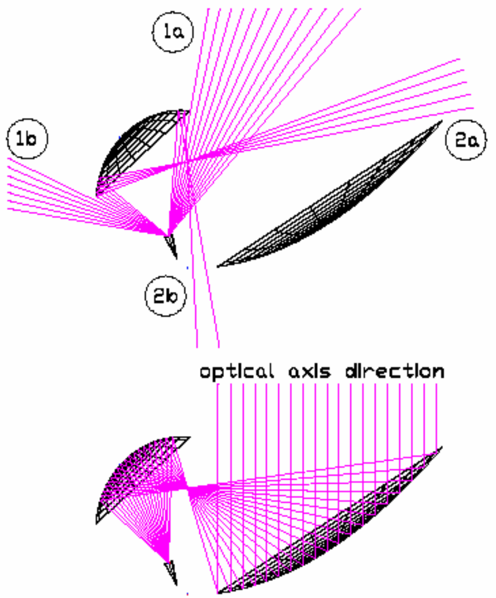

Fig. 1. Sketch of the telescope design in the symmetry plane ($\phi'_{bf} \sim 0$). This figure shows the carrier telescope configuration: a gregorian Dragone-Mizuguchi design with the primary mirror enlarged to 1.5 meter for reducing the main spillover (2a). The upper panel shows the rays coming from unwanted directions and focussed into the feed: (1a) spillover past the subreflector; (1b) spillover past the subreflector redirect by the shields; (2a) spillover past the main reflector; (2b) spillover past the main reflector and redirect by the shields. The bottom drawing shows the telescope with rays coming from the direction of the optical axis and focussed in a feed located at the centre of the focal plane. The spillover blocked by the shield, (1b) and (2b), is redirected close to the main beam as showed on the full-antenna pattern in Fig. 2.

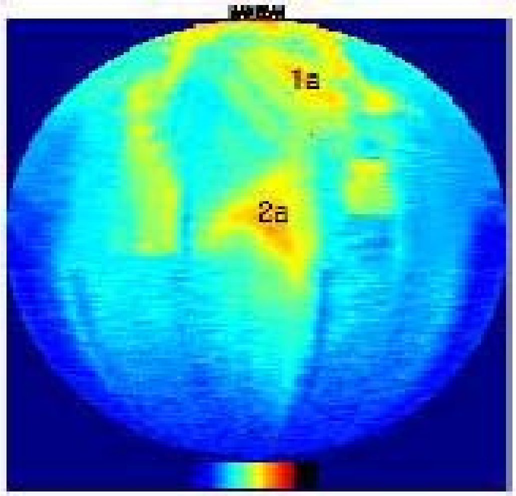

Fig. 2. Full antenna pattern, with response normalized to the maximum, for the carrier configuration. The color table is linear in dB and the true directivity at the maximum is 49.36 dB. Pattern regions related to particular optical structures are identified. See also the text.

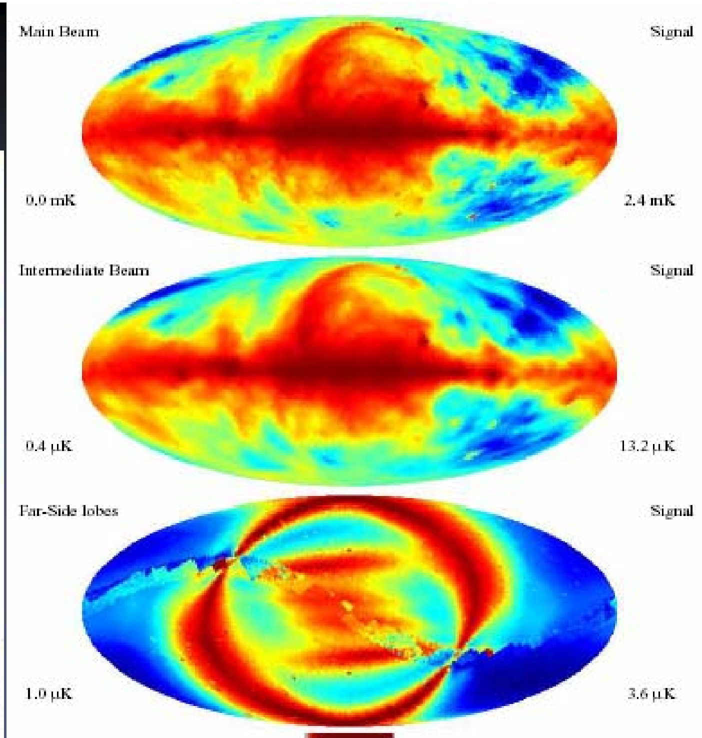

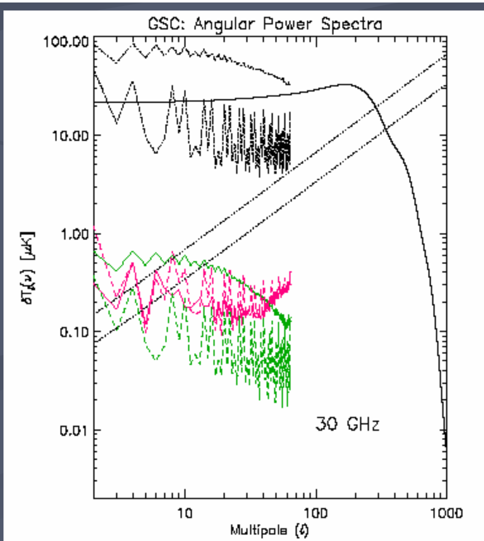

Straylight contamination by the Galaxy:

precise scientific impact evaluation
feedback → optical optimization/trade-off

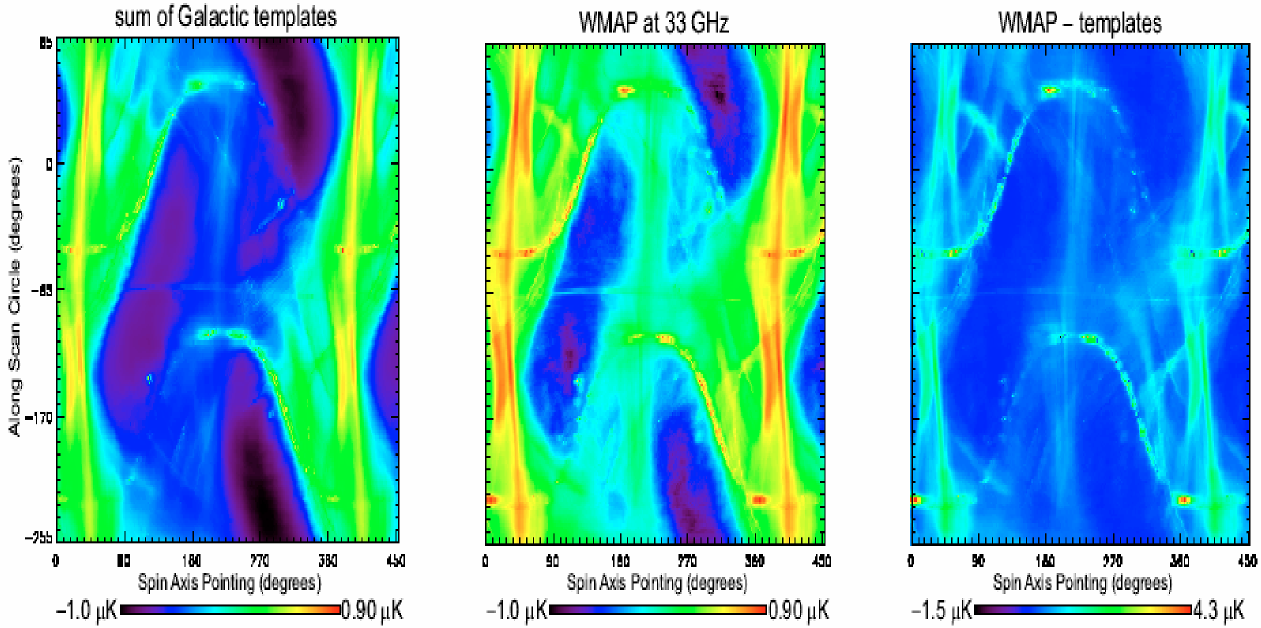

Fig. B.1. The same as in Fig. 2, but for the simulation at 30 GHz and the overall straylight signal. For a better comparison the adopted temperature range is the same in the two panels, although the minimum and maximum values are just different, as it is evident from the different peak-to-peak values reported in Table B.1. The right panel reports (antenna temperature in linear, not logarithmic, scale, in this case) the difference between the middle panel and the left panel (see also the text).

Straylight contamination by the cosmic dipole
Implications: low multipoles, calibration, SS?

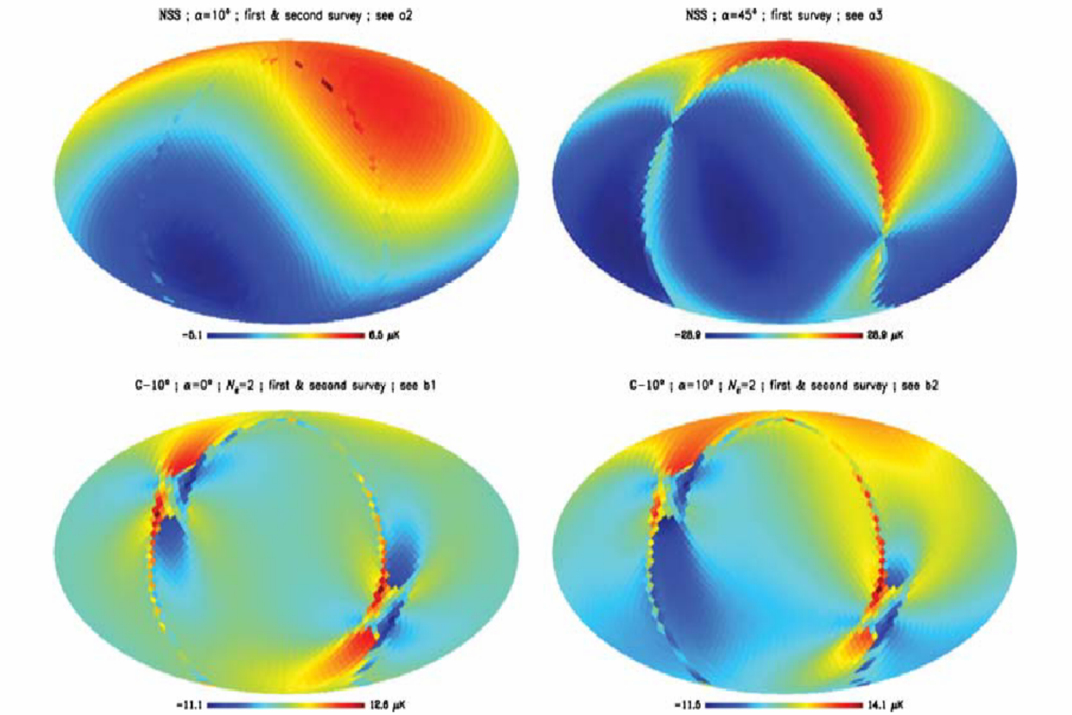

Figure 6. Maps of DSC in the case of the NSS and for $\alpha \neq 0°$ and in the case of a cycloidal scanning strategy (C) with a semi-amplitude of 10° and $\alpha = 0°$ or 10°. The parameters of each case are indicated above each map together with the reference to the panel in Fig. 8 where the corresponding APS is displayed. Galactic coordinates and Mollweide projection are used.

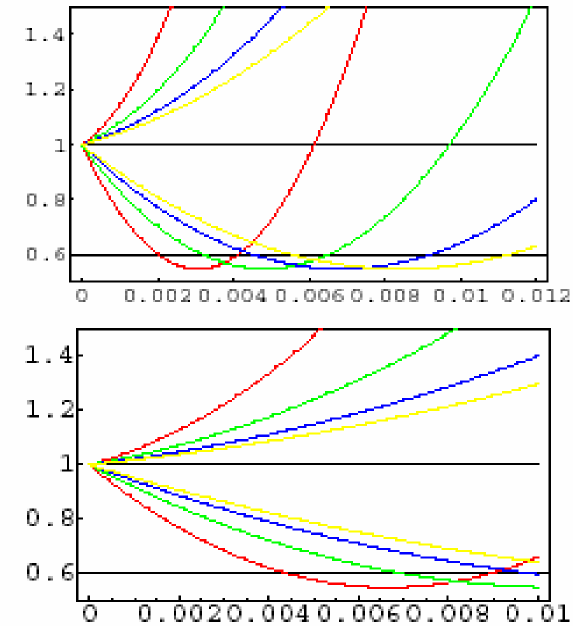

Figure 4. Top panel: $y = y(F_{SL})$ for $C_2^{SKY} = 200\,\mu K^2$ (red line), $C_2^{SKY} = 500\,\mu K^2$ (green line), $C_2^{SKY} = 1000\,\mu K^2$ (blu line) and $C_2^{SKY} = 1500\,\mu K^2$ (yellow line). Lower curves correspond to $(\gamma, f) = (\pi/10, 1/2)$ while upper ones to $(\gamma, f) = (\pi/10 + \pi/2, 1/2)$. Bottom panel is a zoom of top panel but plotted in terms of p instead of F_{SL} (see equation (4.24)): $y = y(p)$ for $C_2^{SKY} = 200\,\mu K^2$ (red line), $C_2^{SKY} = 500\,\mu K^2$ (green line), $C_2^{SKY} = 1000\,\mu K^2$ (blu line) and $C_2^{SKY} = 1500\,\mu K^2$ (yellow line), where $\Delta = \pi/10$. Lower curves correspond to $(\gamma, f) = (\pi/10, 1/2)$ while upper ones to $(\gamma, f) = (\pi/10 + \pi/2, 1/2)$. See also the text.

1/f noise

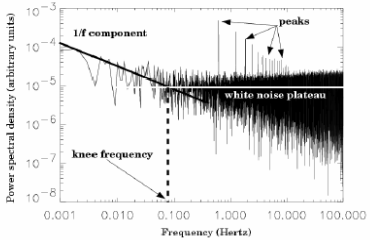

Figure 8: Typical noise power spectrum showing the white noise plateau, a $1/f$ component at low frequencies and periodic peaks.

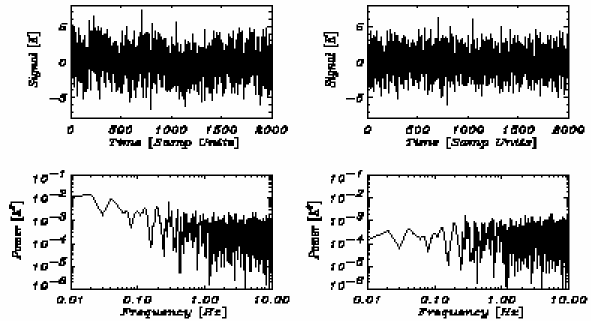

Fig. 2. Comparison between a pure white noise (right) and white+$1/f$ noise (left) in time domain (upper panels) and and Fourier space (bottom panels). Their difference is more clear in Fourier space with a flat spectrum for the white noise and the typical $1/f$ noise spectrum for the low-frequency noise. We used a $f_k = 0.8$ Hz for this illustrative case

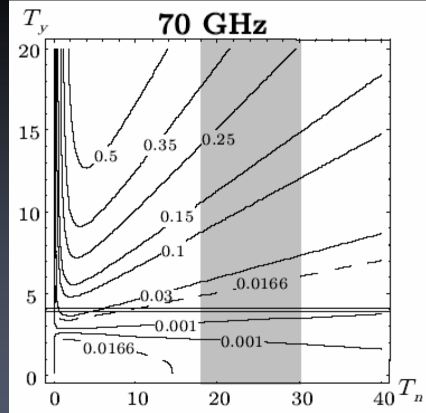

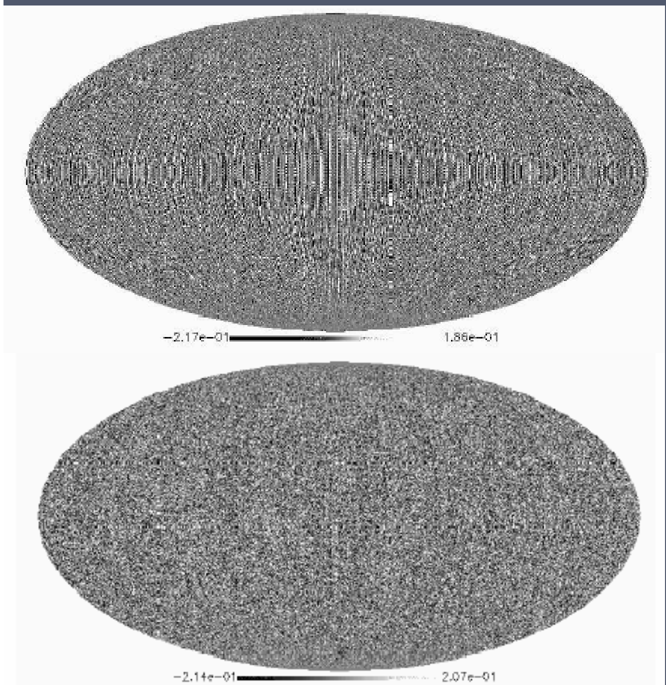

$$f_k^0(T_n) \sim \beta\left[\frac{A\,(1-r)\,T_n}{2\,(T_x+T_n)}\right]^2$$

$$r_0^* = \frac{T_x + T_{ntot}}{T_y + T_{ntot}}$$

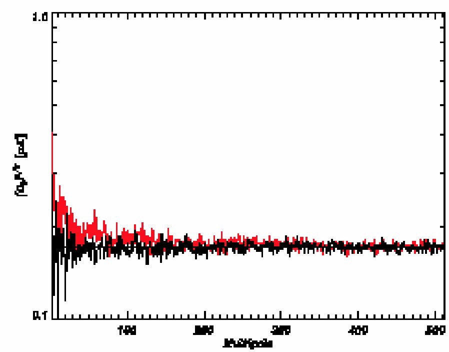

Fig. 9. Noise power spectra at 30GHz after destriping. Simulation parameters are the same of Fig. 8. The added noise is now only 1-2% of the white noise level. White noise spectra are also reported for comparison.

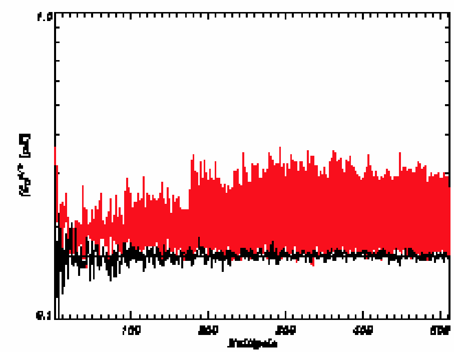

Fig. 10. Noise power spectra at 30GHz Before destriping. Simulation parameters are the same of Fig. 4 but the beam position is now $(\theta_B, \phi_B) = (0°, 0°)$. The added noise is $\sim 42\%$ of the white noise level. White noise spectra are also reported for comparison.

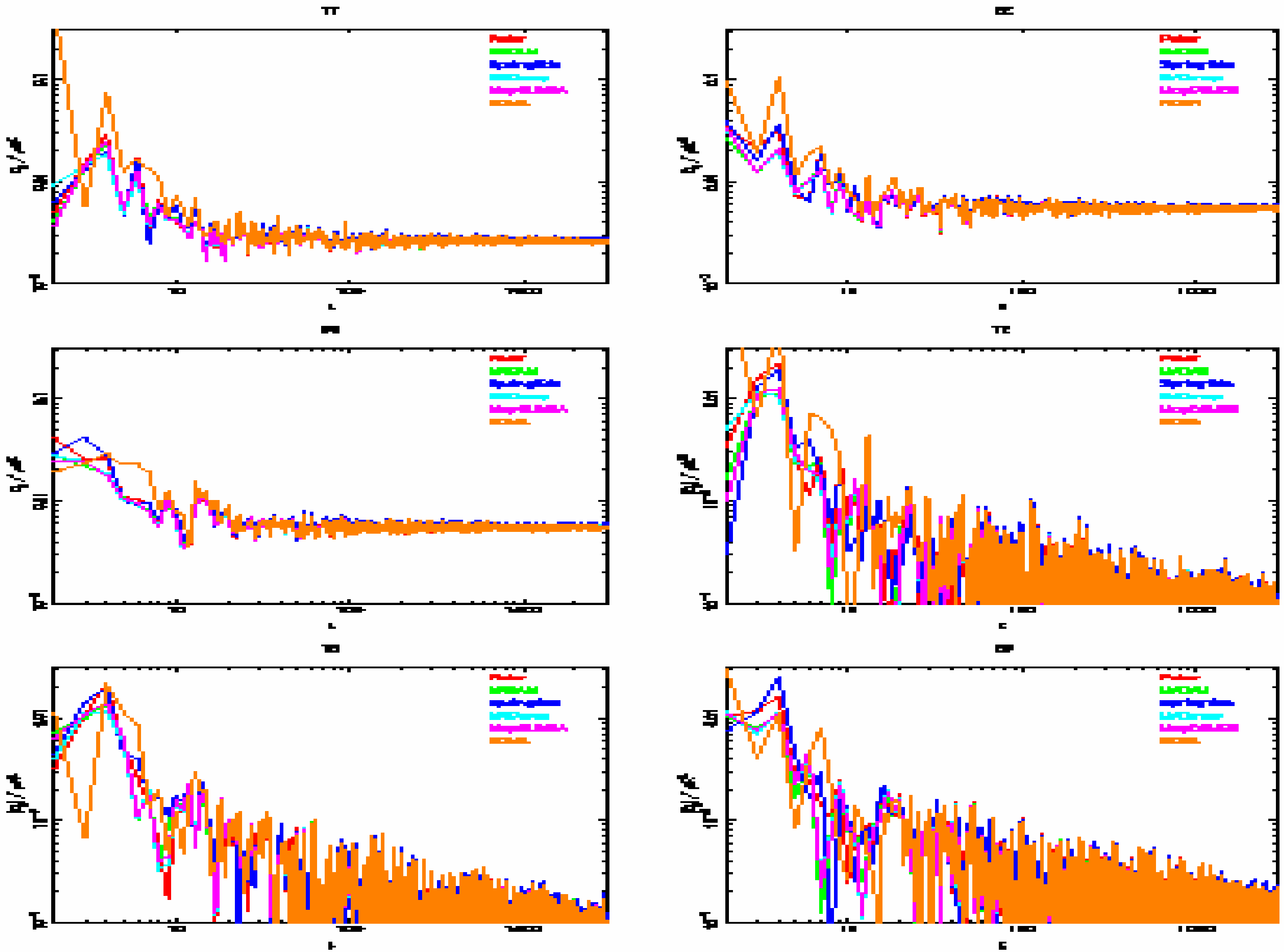

Fig. 2. Spectra of residuals for the polarization simulations with noise in the cycloidal scanning strategy.

M. A. J. Ashdown et al.: Making Sky Maps from Planck Data

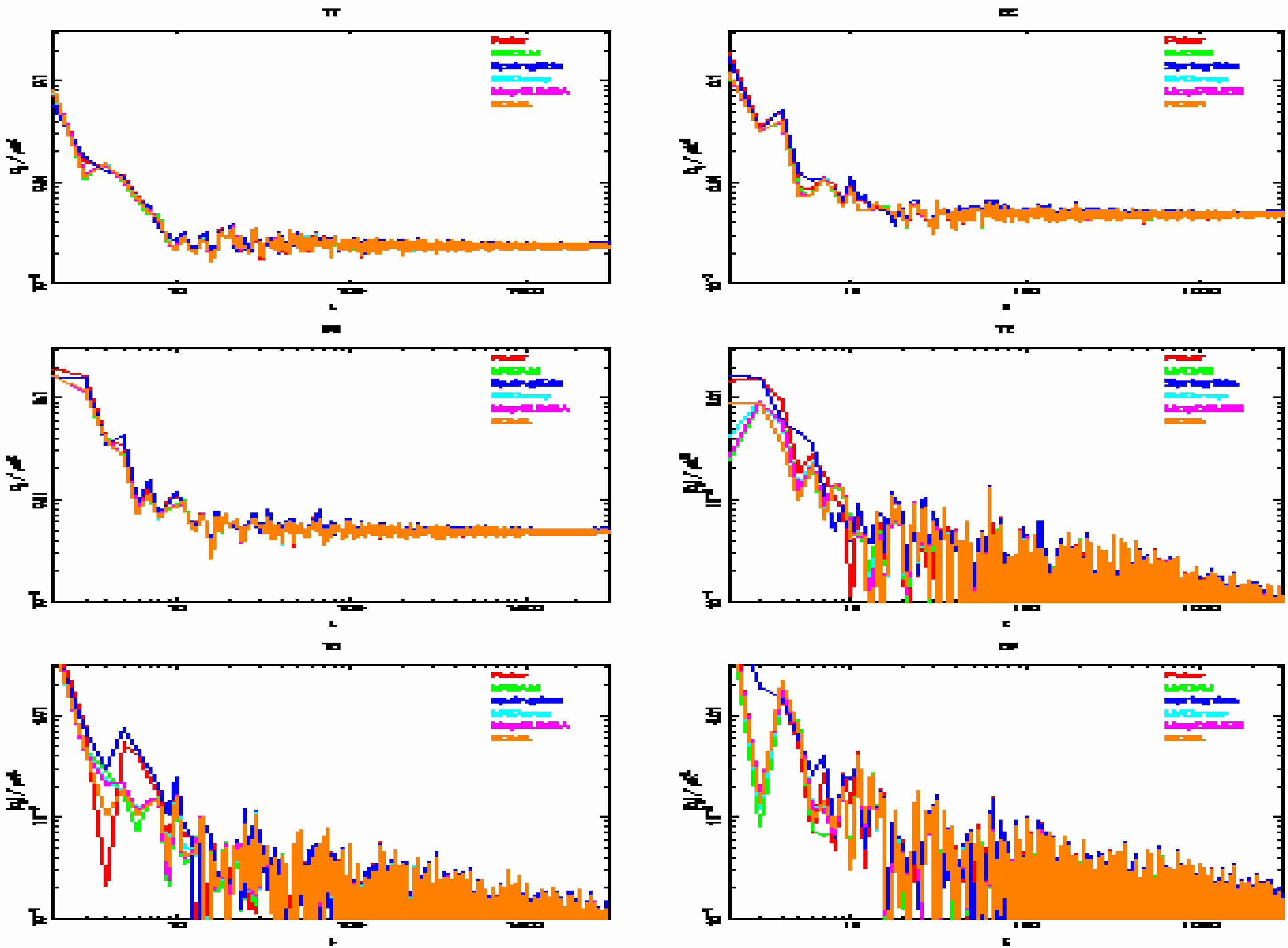

Fig. 3. Spectra of residuals for the polarization simulations with noise in the nominal scanning strategy.

Planck deep fields

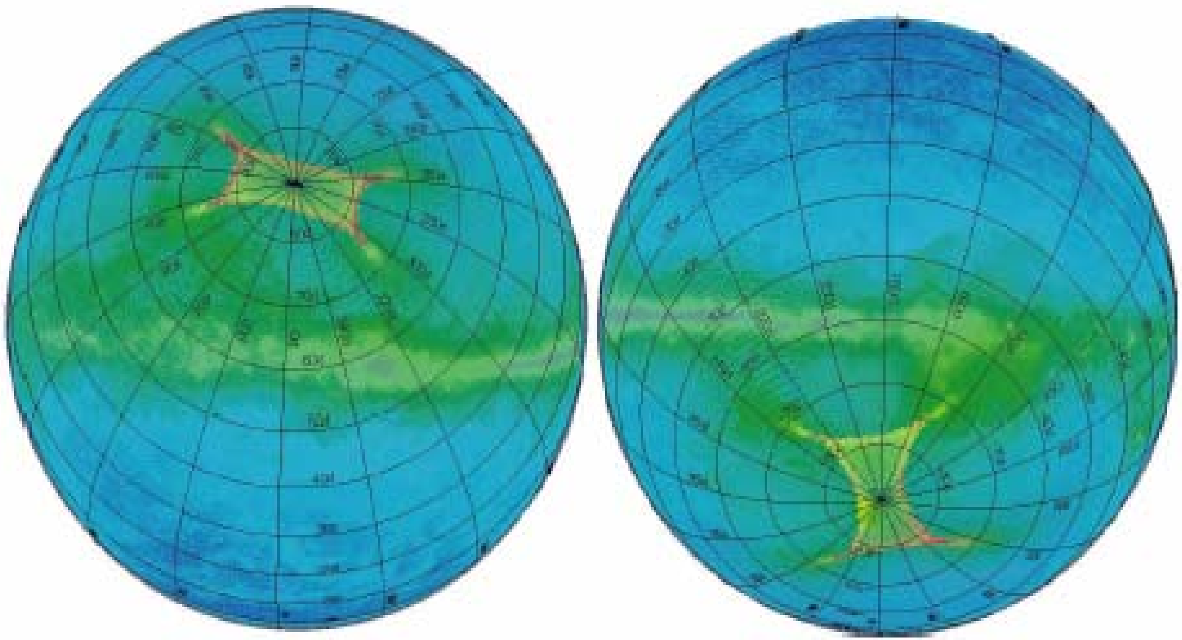

Figure 23: The coverage map at 100 GHz for the selected baseline SS is shown overlaid with the sky at 100 GHz as derived from the Galactic PLANCK sky model.

Planck DPCs

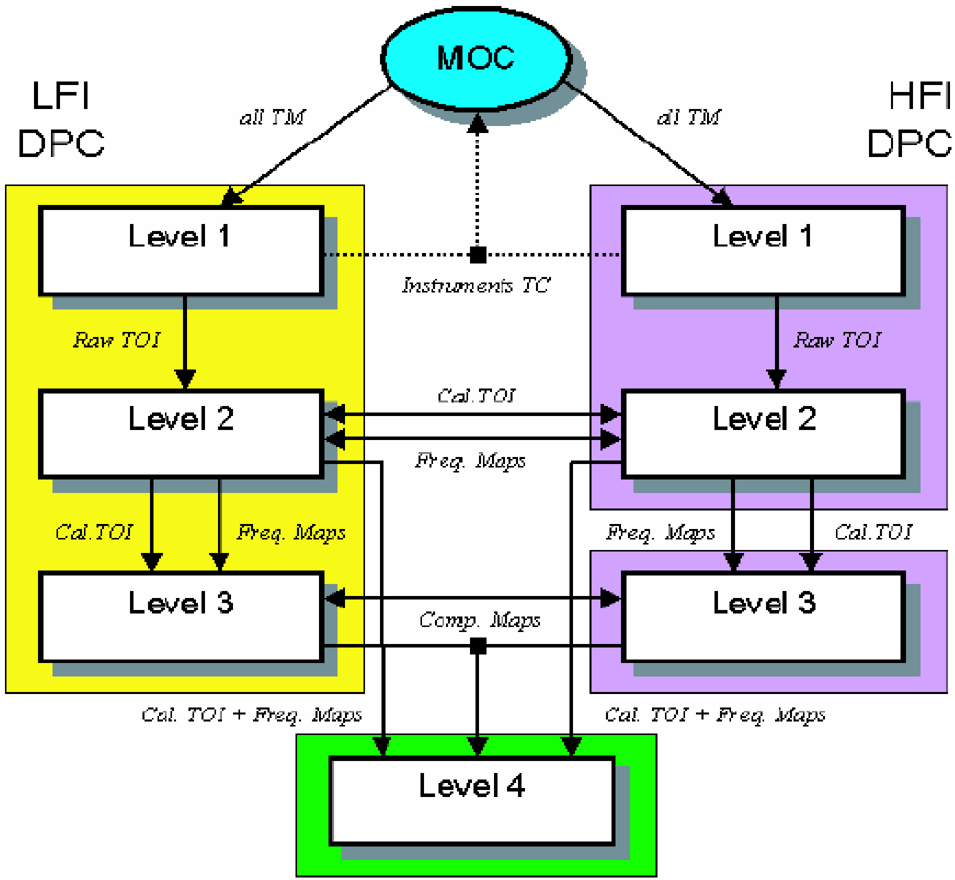

FIG 1.12.—Organization of the DPCs. Each colored box corresponds to a geographically separate location.

LFI DPC Overall Scheme

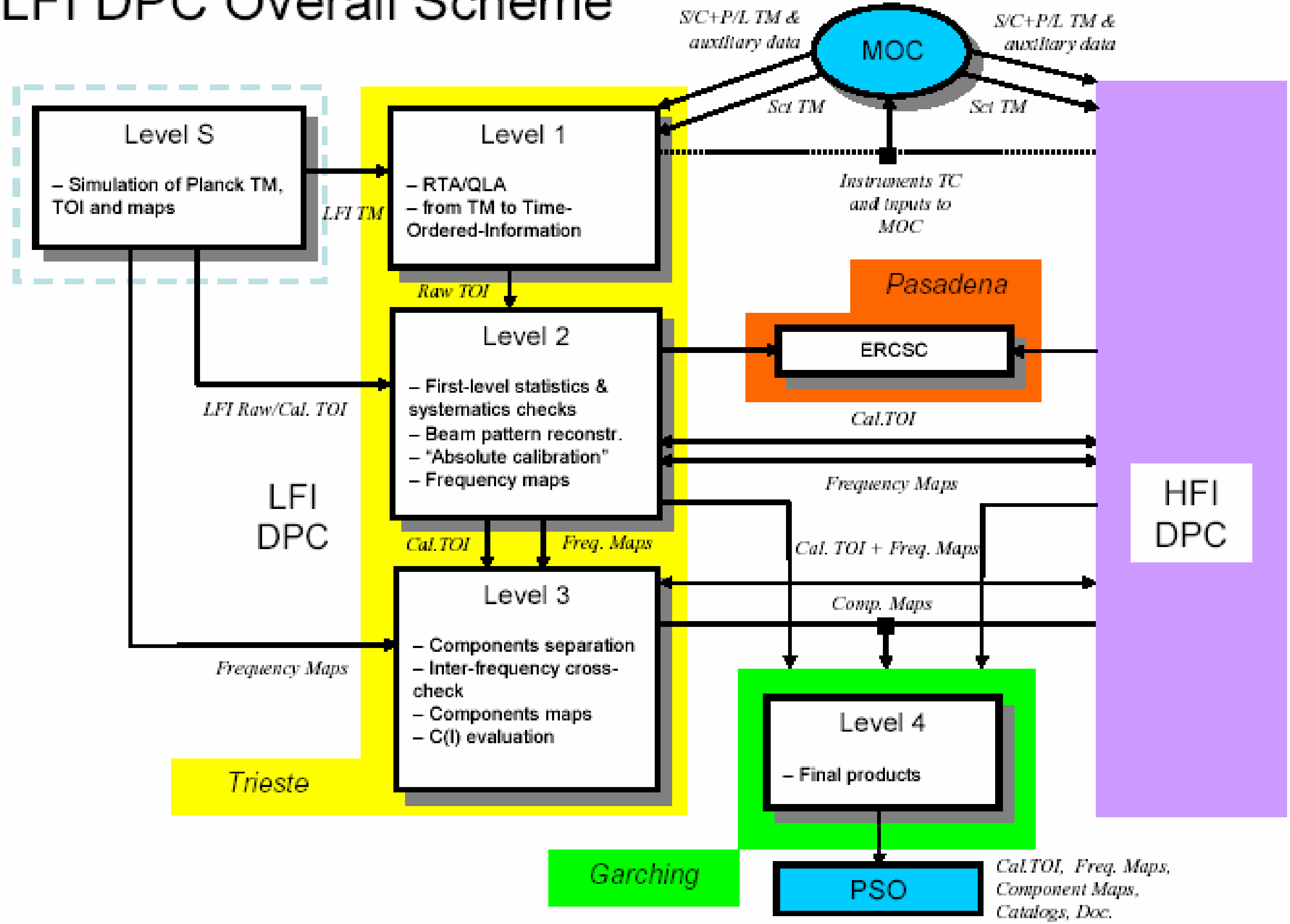

Acquiring and processing time-ordered information

Converting time-ordered data to maps of the sky emission at many frequencies

Converting frequency maps to component maps, e.g. the Cosmic Microwave Background

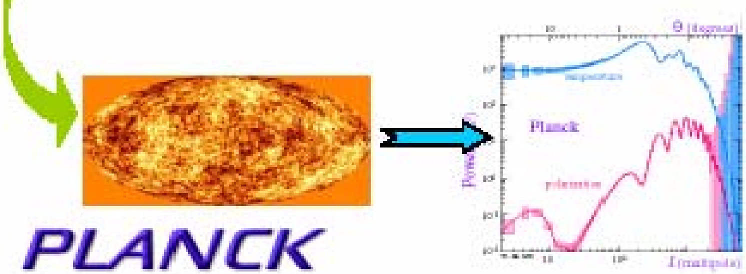

Estimating the CMB angular power spectrum and cosmological parameters

PLANCK

esa ASTROPHYSICS

Planck Sky Model / Foregrounds vs CMB

Microwave sky = CMB + foregrounds
→ it is necessary to understand
& subtract Galactic
& extragalactic foregrounds

in order to recover
CMB anisotropies &
cosmological parameters
at ultimate Planck sensitivity
(≅cosmic variance in TT)

→ foreground studies &
Comp. Sep. Techniques
→ multifrequency
approach

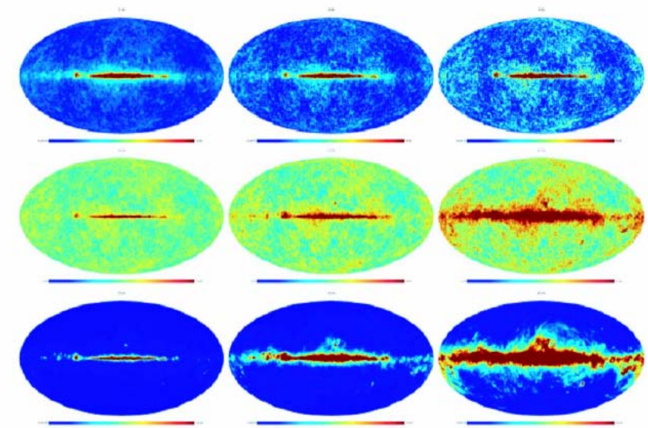

FIG 5.1.— False colour images of the simulated sky in the nine frequency channels of *Planck*, after subtraction of the monopole and dipole CMB components. From top left to bottom right: 30, 44, 70, 100, 143, 217, 353, 545, and 857 GHz channels.

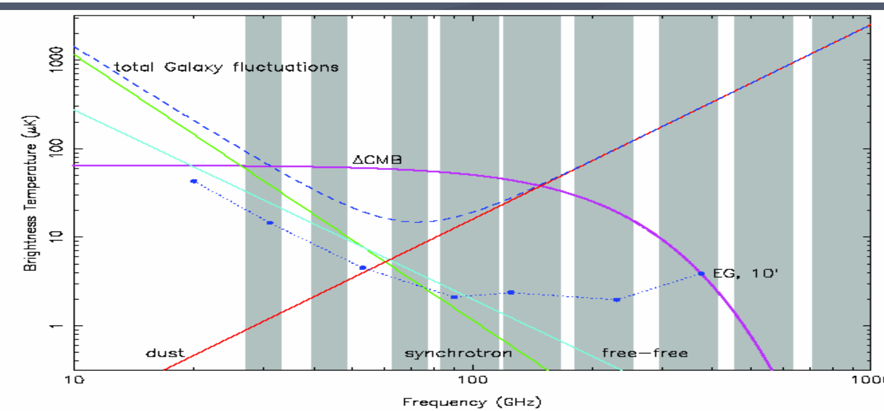

FIG 1.3.— Spectrum of the CMB, and the frequency coverage of the *Planck* channels. Also indicated are the spectra of other sources of fluctuations in the microwave sky. Dust, synchrotron, and free-free temperature fluctuation (i.e., unpolarized) levels correspond to the *WMAP* Kp2 levels (85% of the sky; Bennett et al. 2003). The CMB and Galactic fluctuation levels depend on angular scale, and are shown for ~1°. On small angular scales, extragalactic sources dominate. The minimum in diffuse foregrounds and the clearest window on CMB fluctuations occurs near 70 GHz. The highest HFI frequencies are primarily sensitive to dust.

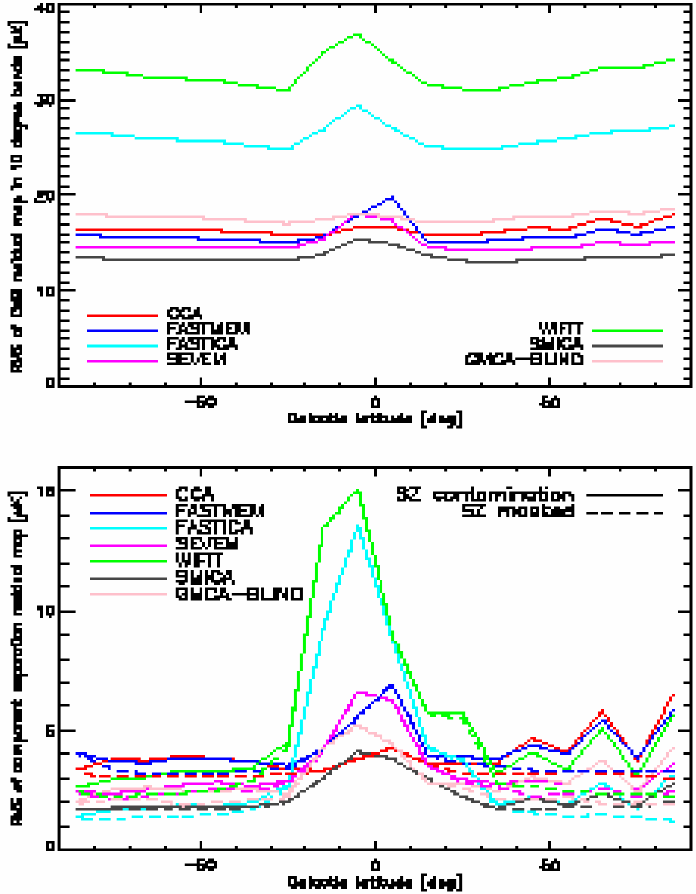

Fig. 4. (Upper) RMS of the residual error of the CMB map, calculated for each of 18 bands of 10 degrees wide in galactic latitude. For comparison, $\sigma_{\rm CMB}$ = 104.5μK and $\sigma_{\rm noise}$ = 29.3μK, for the 143 GHz channel (1.7′ pixels). (Lower) RMS of this residual map calculated at 45′ resolution. For comparison, $\sigma_{\rm CMB}(45') = 69.8\mu$K and $\sigma_{\rm noise}(45') = 0.7\mu$K for the 143 GHz channel. The corresponding residual maps are shown in Figure B.1.

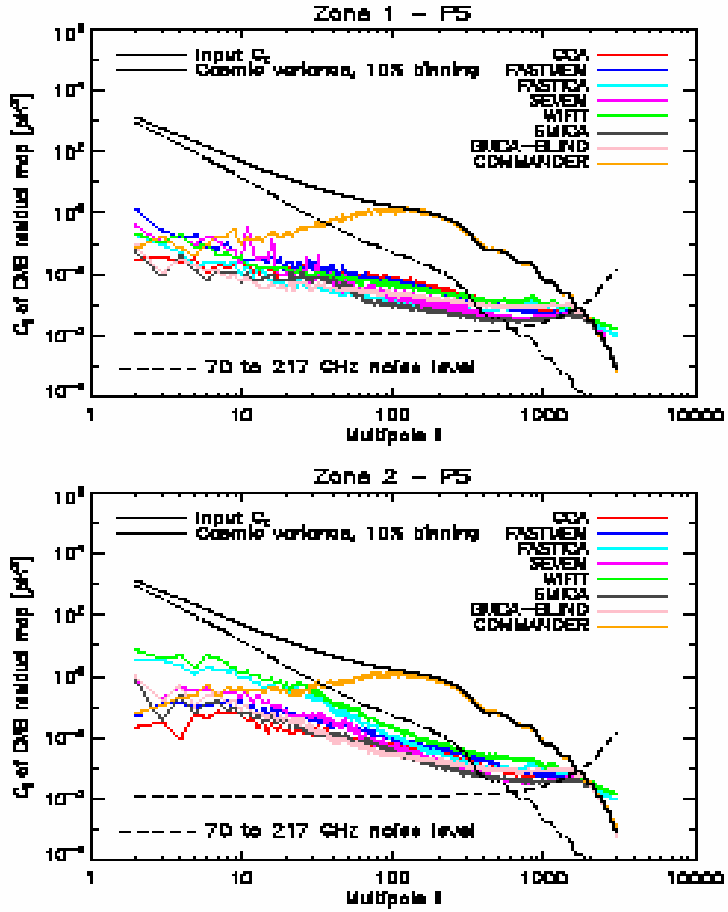

Fig. 5. Spectra of the CMB residual maps, evaluated on Zone 1 (high galactic latitudes) and Zone 2 (low galactic latitudes), both regions with point sources masked. Comparison with Figure 2 shows the extent to which the galactic contamination has been removed from the CMB on large angular scales.

Planck 4 surveys vs next generation (e.g. B-Pol)

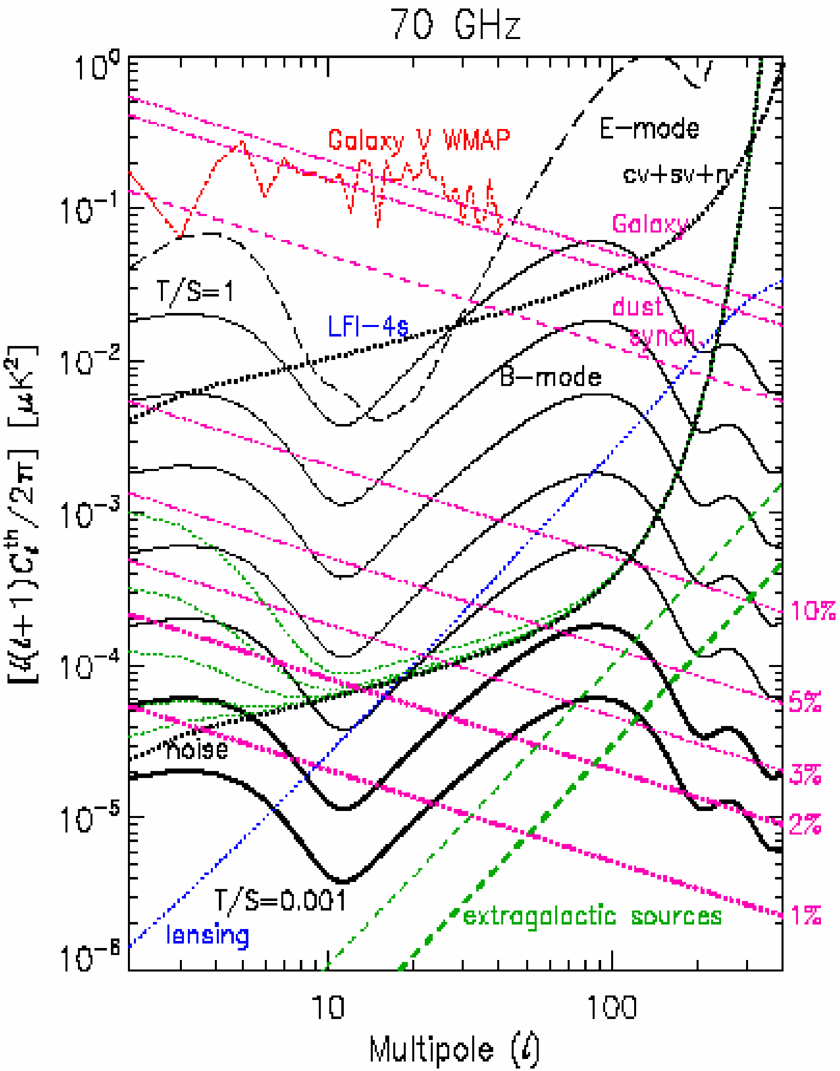

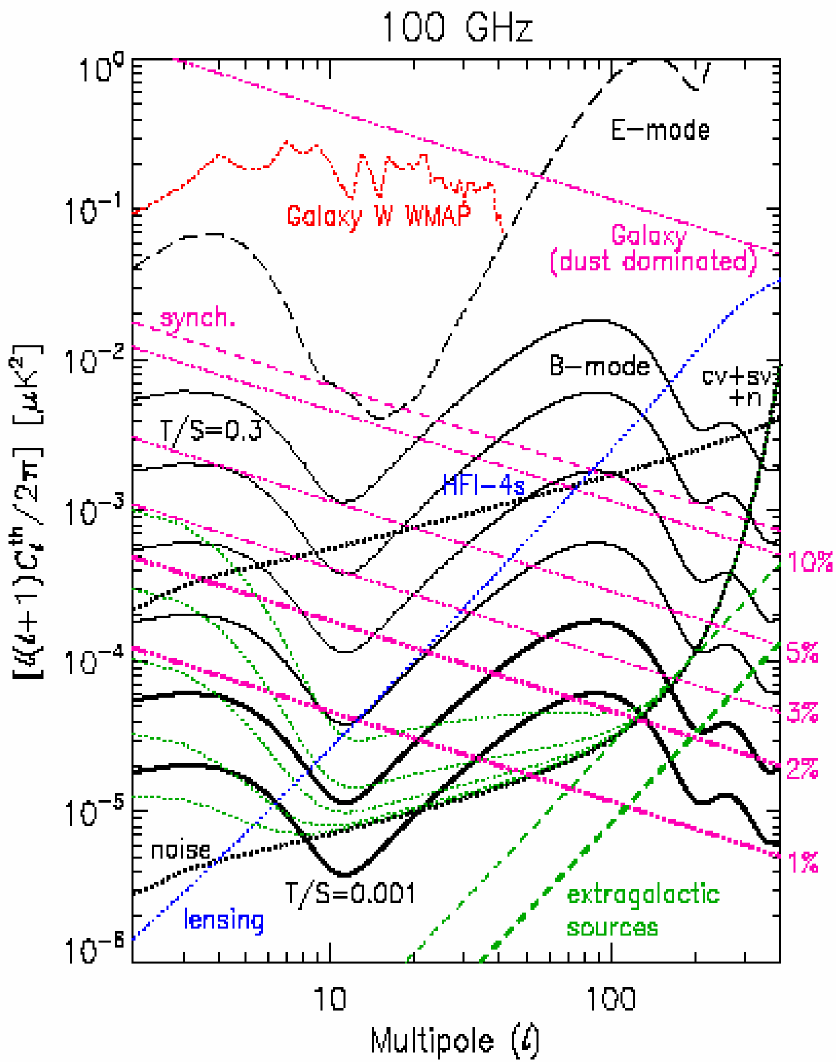

Figure 7: CMB E and B polarization modes compatible with WMAP 3-yr data compared to Galactic and extragalactic polarized (B-mode) foregrounds, the B-mode induced by lensing and their residuals and to the BPOL sensitivity including cosmic and sampling variance plus instrumental noise (black dotted lines labelled with cv+sv+n) assuming a multipole binning of 30%. Two different frequency are considered here. We display the E-mode (black long dashes); the B mode (black solid lines) is reported for different values of T/S (0.1, 0.03, 0.01, 0.003, 0.001 from top to bottom, at increasing thickness). Note that the cosmic and sampling (74% of sky coverage) variance implies a dependence of the overall sensitivity at low multipoles on T/S (again the black dotted lines refer to $T/S = 0.1$, 0.03, 0.01, 0.003, 0.001 from top to bottom). Galactic synchrotron (fuxia dashes) and dust (fuxia dot-dashes) polarized emissions produce the overall Galactic foreground (fuxia three dot-dashes) that is dominated by dust at 100 GHz. WMAP 3-yr power law approximations in the case of uncorrelated dust and synchrotron components are displayed here. For comparison, WMAP 3-yr results derived directly from the foreground maps are shown on a suitable multipole range: note that power law approximations provide (generous) upper limits of the power at low multipoles. Various level of residual contaminations by Galactic foregrounds (fuxia three dot-dashes) are shown for increasing capability to remove them (from 10% to 1% at map level at increasing thickness, labelled on the right). The contribution by extragalactic sources, C_ℓ^{resPS}, and the corresponding uncertainty, $\delta C_\ell^{\mathrm{resPS}}$, assuming $\delta\Pi/\Pi = \delta S_{\mathrm{lim}}/S_{\mathrm{lim}} = 10\%$ are reported (green dashes, thin and thick, respectively). The B-mode induced by lensing and its residual assuming a (conservative) 10% suppression accuracy at APS level are displayed (blue dots, thin and thick, respectively).

Cosmological implications

- Geometrical degeneracy(ies) of TT fluctuations, e.g.:
  - Matter density, vacuum energy, curvature, for models with same P(k), τ_{reion}, $H_0^2\Omega_c$, $H_0^2\Omega_b$, & acoustic peak location

$$\mathcal{R} = \frac{\Omega_{\rm m}^{1/2}}{|\Omega_k|^{1/2}} \sin_k \left[|\Omega_k|^{1/2} y \right],$$

$$y = \int_{a_r}^{1} \frac{da}{[\Omega_{\rm m} a + \Omega_k a^2 + \Omega_\Lambda a^4]^{1/2}},$$

$$\Omega_k \; (\equiv 1 - \Omega_{\rm m} - \Omega_\Lambda)$$

$$\sin_k x = \begin{cases} \sinh x, & \Omega_k > 0; \\ x, & \Omega_k = 0; \\ \sin x, & \Omega_k < 0. \end{cases}$$

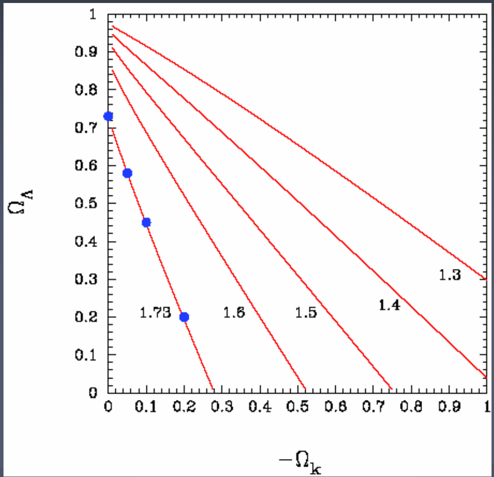

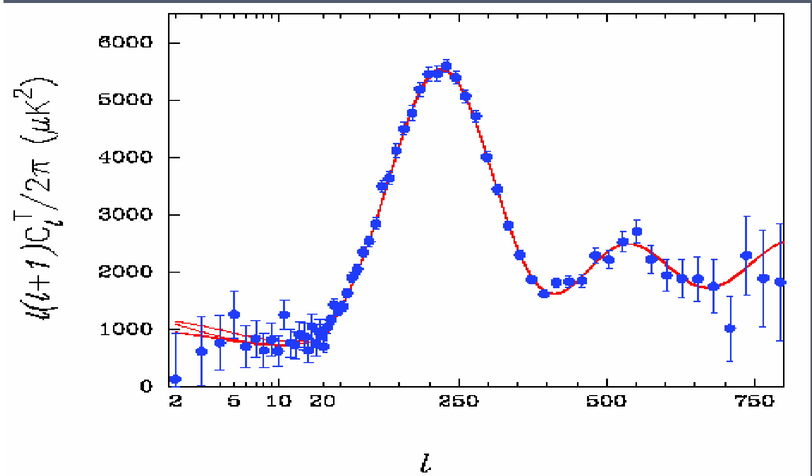

→ Solution(s):
  - → Adding polarization
  - → Adding other cosmological information from LSS, SNe, Lyα, …

The shape of the power spectrum depends sensitively on the value of cosmological parameters

Main Cosmological Parameters

- Ω_0 Cosmological total density parameter
- H_0 Hubble constant
- Ω_b Baryon density
- Ω_c Cold dark matter density
- Λ Cosmological constant
- n_s Spectral index of scalar perturbations
- Q Amplitude of fluctuation spectrum
- r Ratio of Gravitational wave to density perturbations
- τ_r Residual optical depth due to reionisation

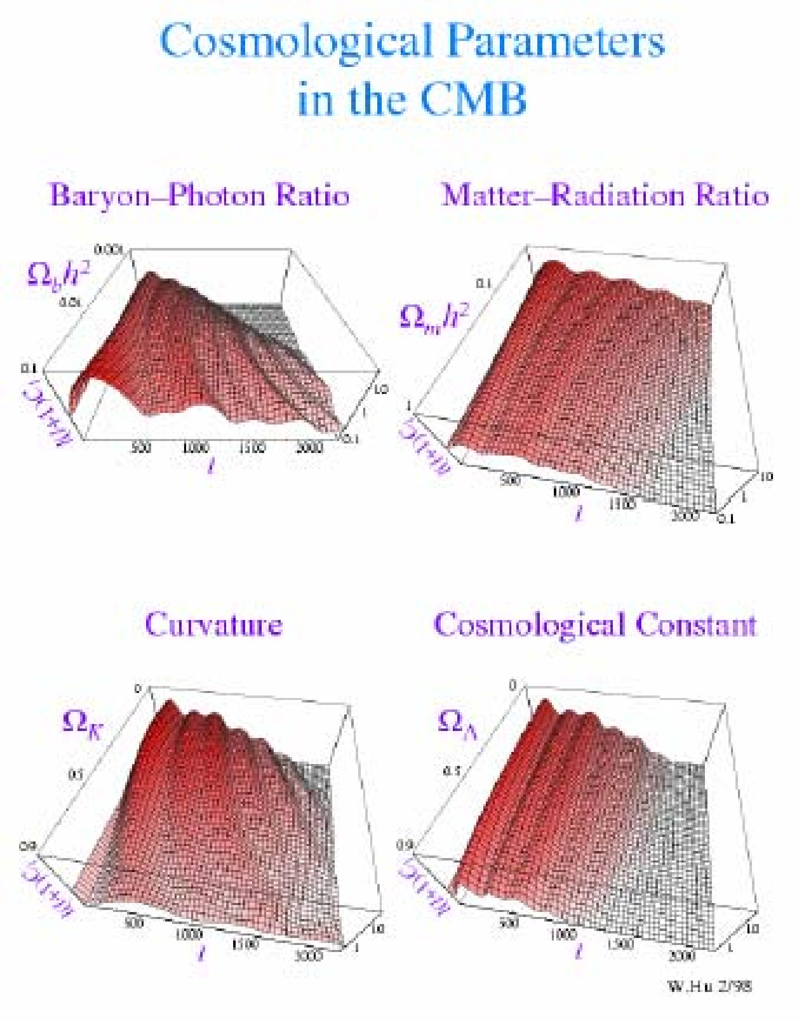

Parameter Forecasts for WMAP and Planck

Parameter	Input Value	June'03	June'03 +2dF	$WMAP_4$	*Planck*	$WMAP_4$ ACT/SPT
Flat+weak priors						
ω_b	0.2240	0.00095	0.00090	0.00047	0.00017	0.00025
ω_c	0.1180	0.011	0.007	0.0039	0.0016	0.0035
n_S	0.9570	0.026	0.024	0.0125	0.0045	0.0080
τ	0.108	0.059	0.056	0.020	0.005	0.021
+running						
ω_b	0.2240	0.00162	0.00090	0.00047	0.00017	0.00025
ω_c	0.1180	0.0158	0.007	0.0039	0.0016	0.0035
$n_S(k_n)$	0.9570	0.055	0.024	0.0125	0.0045	0.0080
n_{run}	0.0	0.033	0.029	0.025	0.005	0.0092
τ	0.108	0.112	0.074	0.019	0.006	0.0266

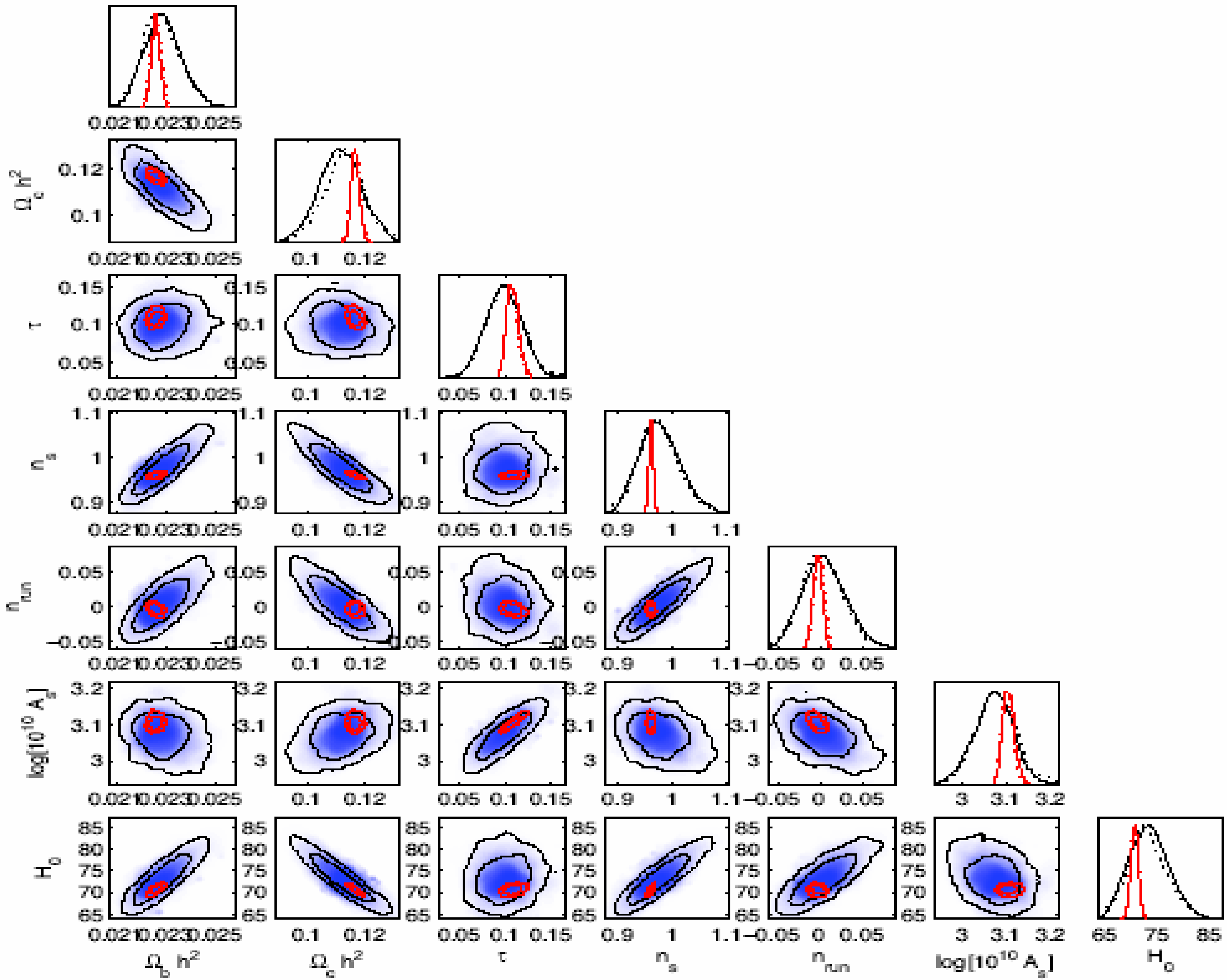

FIG. 2.18.—Forecasts of 1 and 2σ contour regions for various cosmological parameters when the spectral index is allowed to run. Blue contours show forecasts for *WMAP* after 4 years of observation and red contours show results for *Planck* after 1 year of observations. The curves show marginalized posterior distributions for each parameter.

Implication for inflation

$$H^2 = \left(\frac{\dot{a}}{a}\right)^2 = \frac{8\pi G}{3}\rho - \frac{k}{a^2}$$

$$\dot{\rho} = -3\left(\frac{\dot{a}}{a}\right)(\rho + p)$$

$$p = -\rho$$

$$a(t) \propto \exp(Ht), \qquad H \simeq \text{constant}$$

$$\rho = \frac{1}{2}\dot{\phi}^2 + V(\phi), \quad p = \frac{1}{2}\dot{\phi}^2 - V(\phi)$$

ϕ is a real scalar field with potential $V(\phi)$

$$\ddot{\phi} + 3H\dot{\phi} = -\frac{\partial V}{\partial \phi}$$

$$\dot{\phi}^2 \ll V(\phi)$$

$$p \simeq -\rho$$

$$H^2 = \frac{8\pi G}{3}V(\phi) = \frac{8\pi}{3m_{\rm Pl}^2}V(\phi)$$

$$\epsilon = \frac{m_{\rm Pl}^2}{16\pi}\left(\frac{V'}{V}\right)^2, \quad \eta = \frac{m_{\rm Pl}^2}{8\pi}\left(\frac{V''}{V}\right)$$

$$P_S(k) \simeq \left(\frac{H^2}{16\pi^3\dot{\phi}^2}\right)_{(k=aH)} \qquad \text{(scalar perturbations)},$$

$$P_T(k) \simeq \left(\frac{H^2}{4\pi^2 m_{Pl}^2}\right)_{(k=aH)} \qquad \text{(tensor perturbations)}$$

$$r \equiv \frac{C_\ell^T}{C_\ell^S} \sim 10\epsilon$$

$$n_S - 1 \simeq -6\epsilon + 2\eta,$$

$$n_T \simeq -2\epsilon.$$

$$\frac{dn_S}{d\ln k} \simeq -16\epsilon\eta + 24\epsilon^2 + 2\xi^2$$

$$\xi^2 = \frac{m_{Pl}^4}{(8\pi)^2}\left(\frac{V'V'''}{V^2}\right)$$

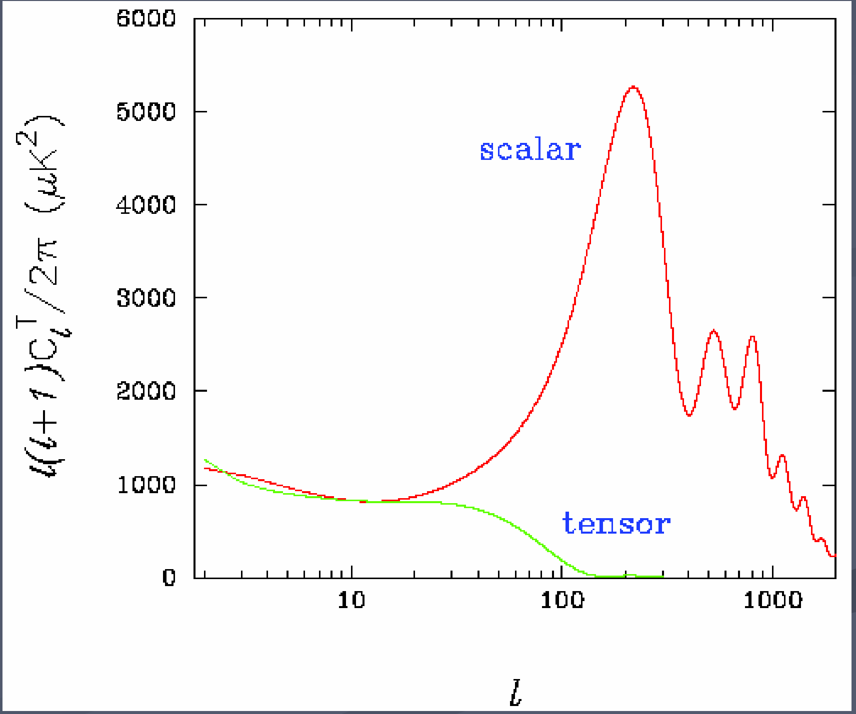

Large field models (e.g. Linde '83)

$$(|\epsilon| < \eta)$$

$$V(\phi) = \frac{\lambda}{4}\phi^4$$

$$\epsilon \simeq 0.02, \quad \eta \simeq 0.03, \quad n_S \simeq 0.06, \quad \frac{dn_S}{d\ln k} \simeq 0.001, \quad r \simeq 0.2$$

$$N = 50 \ \text{e-foldings}$$

Small field models

(e.g. Linde '82, Albrecht & Steinhardt '82)

$$(\eta < -\epsilon)$$

$$V(\phi) = V_0(1 - \mu\phi^p)$$

Hybrid models

$$(0 < \epsilon < \eta)$$

$$V = V_0 + \frac{1}{2}m^2\phi^2 - \frac{1}{2}m_\psi^2\psi^2 + \frac{1}{4}\lambda\psi^4 + \frac{1}{2}\lambda'\psi^2\phi^2$$

(e.g. Linde '91; see also Lyth & Riotto '99)

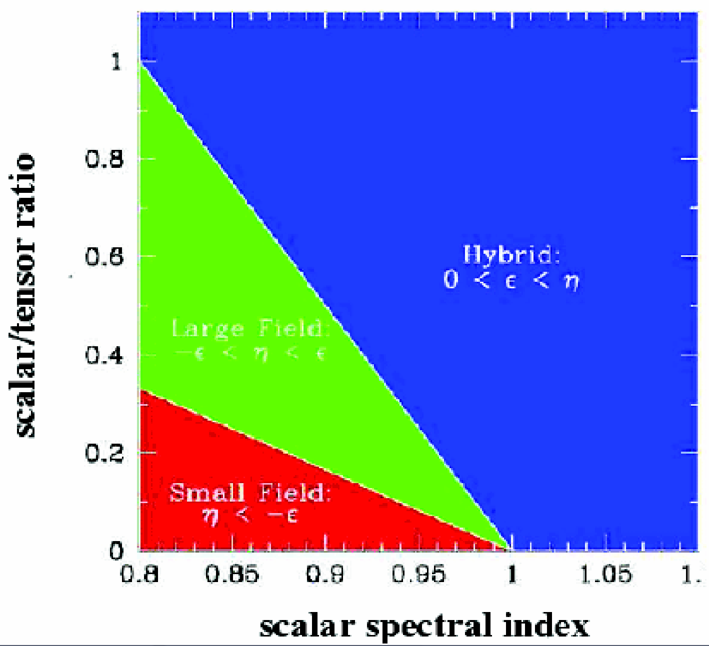

FIG 2.10.—The three classes of inflationary models discussed in the text, delineated in the plane of the tensor-to-scalar ratio r (Eq. 2.14) versus scalar spectral index n_S (adapted from Kinney, Melchiorri and Riotto, 2001)

$$C_\ell = (1-\alpha)C_\ell^{\rm ad} + \alpha C_\ell^{\rm iso} + 2\beta\sqrt{\alpha(1-\alpha)}C_\ell^{\rm corr}$$

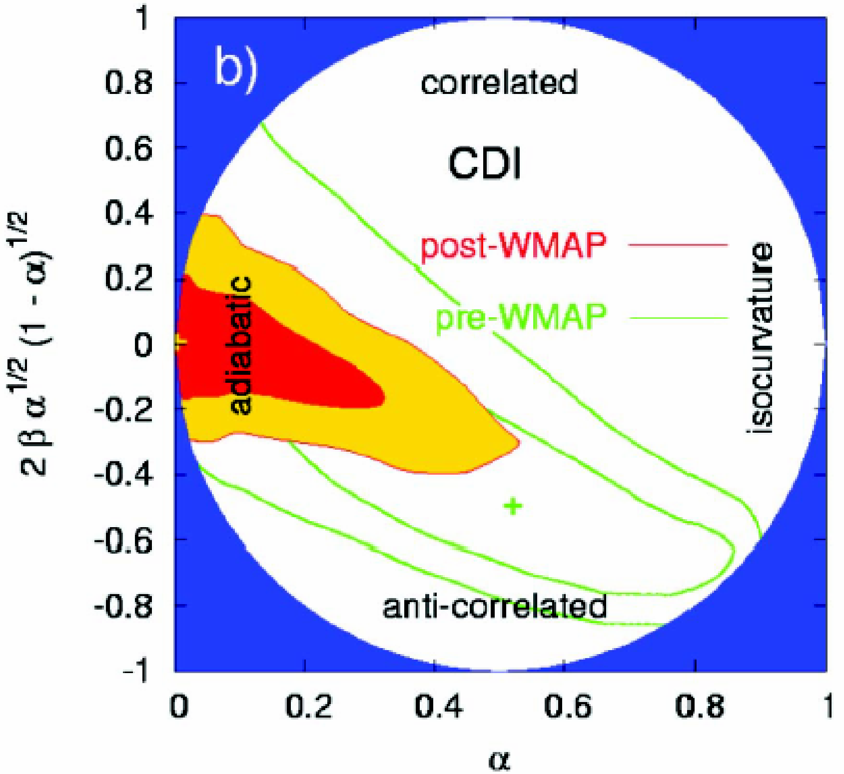

Amendola et al. 2002

Isocurvature vs adiabatic modes

FIG 2.23.—1σ and 2σ contours on the parameters α and the cross-correlation coefficient $2\beta\sqrt{\alpha(1-\alpha)}$ for an admixture of adiabatic and CDM isocurvature modes. These constraints use CMB anisotropy data combined with the 2dF galaxy survey. The green contours show the constraints using CMB data prior to *WMAP* and the filled contours show the post-*WMAP* constraints. (From Crotty et al. 2003).

Testing Isocurvature Modes with WMAP and Planck

	WMAP T adia only	*WMAP* TP adia only	*WMAP* T all modes	*WMAP* TP all modes	*Planck* T adia only	*Planck* TP adia only	*Planck* T all modes	*Planck* T+P all modes	*Planck* TP all modes
$\delta h/h$	12.37	7.42	175.74	20.40	11.50	3.71	94.67	7.75	4.53
$\delta\Omega_b/\Omega_b$	27.76	13.34	325.21	28.57	22.89	7.34	182.01	15.44	8.98
$\delta\Omega_k$	9.79	82.72	75.30	4.55	5.93	1.86	50.58	3.95	2.30
$\delta\Omega_\Lambda/\Omega_\Lambda$	12.92	85.02	123.61	18.53	2.67	1.20	9.79	2.36	1.48
$\delta n_S/n_S$	7.02	81.62	89.87	6.53	0.74	0.37	4.89	0.87	0.70
τ	37.39	81.81	104.83	2.23	10.16	0.41	72.53	0.77	0.57
$\langle$NIV, NIV$\rangle$	...	...	114.34	11.47	...	...	80.87	1.36	1.14
$\langle$BI, BI$\rangle$	...	...	573.46	29.71	...	...	56.72	6.31	4.27
$\langle$NID, NID$\rangle$	...	...	351.72	29.87	...	...	42.05	4.73	2.40
$\langle$NIV, AD$\rangle$	...	...	434.70	44.06	...	...	212.80	8.19	4.69
$\langle$BI, AD$\rangle$	...	...	1034.79	59.25	...	...	94.11	14.97	9.05
$\langle$NID, AD$\rangle$	...	...	1287.47	67.49	...	...	179.17	13.68	5.85
$\langle$NIV, BI$\rangle$	...	...	601.83	32.29	...	...	79.07	7.63	3.68
$\langle$NIV, NID$\rangle$	...	...	743.93	46.46	...	...	133.88	7.42	2.98
$\langle$BI, NID$\rangle$	...	...	534.33	39.11	...	...	115.54	7.68	4.70

1σ errors (given as percentages of input model values) on cosmological parameters and isocurvature mode amplitudes anticipated for the *WMAP* and *Planck* satellite. In the column headers, 'T' denotes constraints inferred from temperature measurements alone, 'TP' those from the complete temperature and polarization measurements, and 'T+P' those inferred if temperature and polarization information is used separately without including the cross-correlation. Here the spectral indices for isocurvature modes have been fixed to their scale-invariant values, which would yield a flat CMB spectrum asymptotically at low ℓ. 'AD' refers to adiabatic modes, 'NIV' and 'NID' to neutrino velocity and density isocurvature modes, and 'BI' to baryon isocurvature modes. (Adapted from Bucher et al. 2001).

Implication for Dark Energy

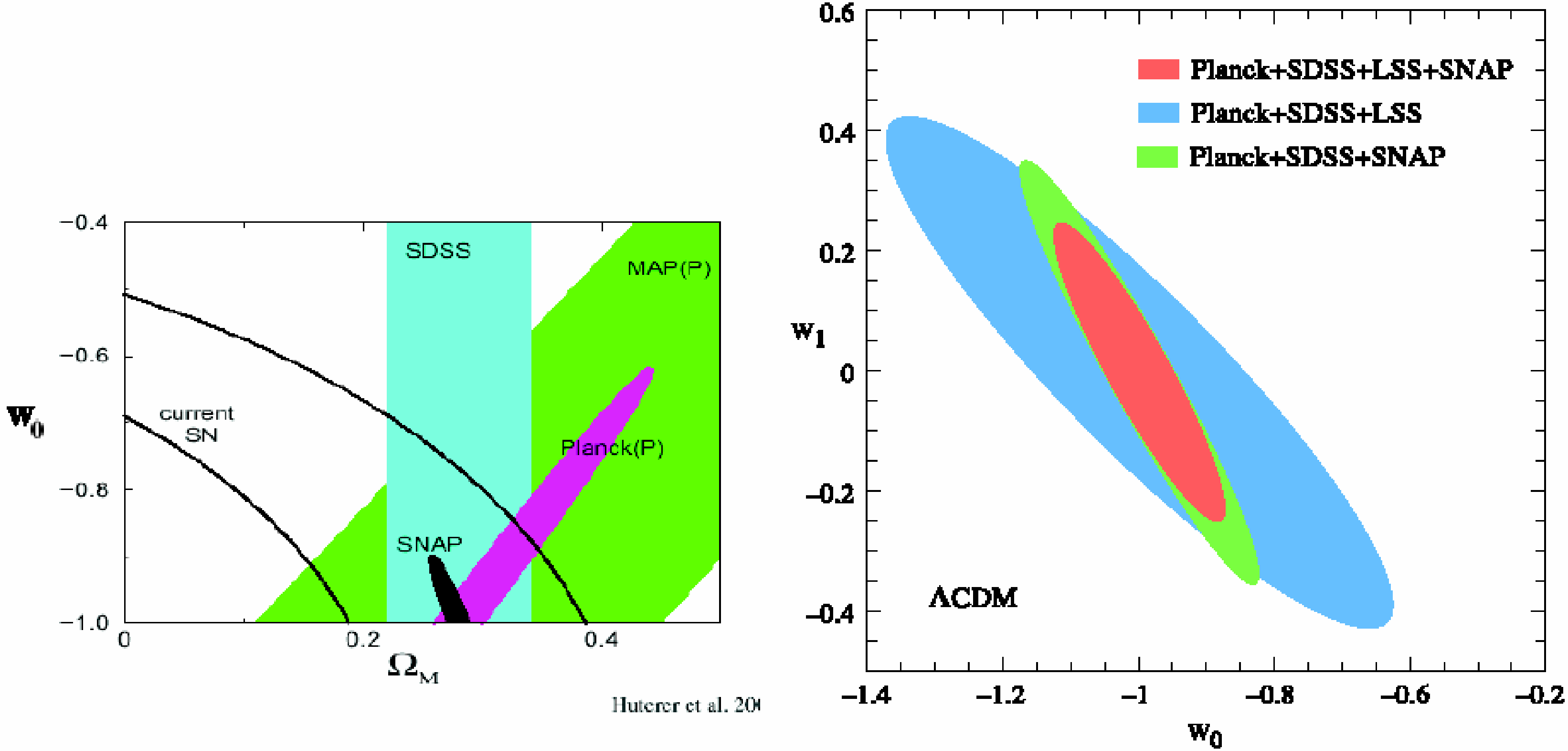

FIG 2.22.—The left panel (from Huterer & Turner 2001) shows forecasts of constraints on the dark energy equation of state parameter w and Ω_m for various experiments including *Planck*. The right panel (from Seo & Eisenstein 2003) shows forecasts of constraints on the time evolution of w, parameterised through $w \equiv w_0 + w_1 z$, for *Planck* combined with various redshift surveys and SNe observations from SNAP (see text for details).

$$w_0 + w_1 z.$$

Towards "astrophysical cosmology" with CMB - E mode & Reionization

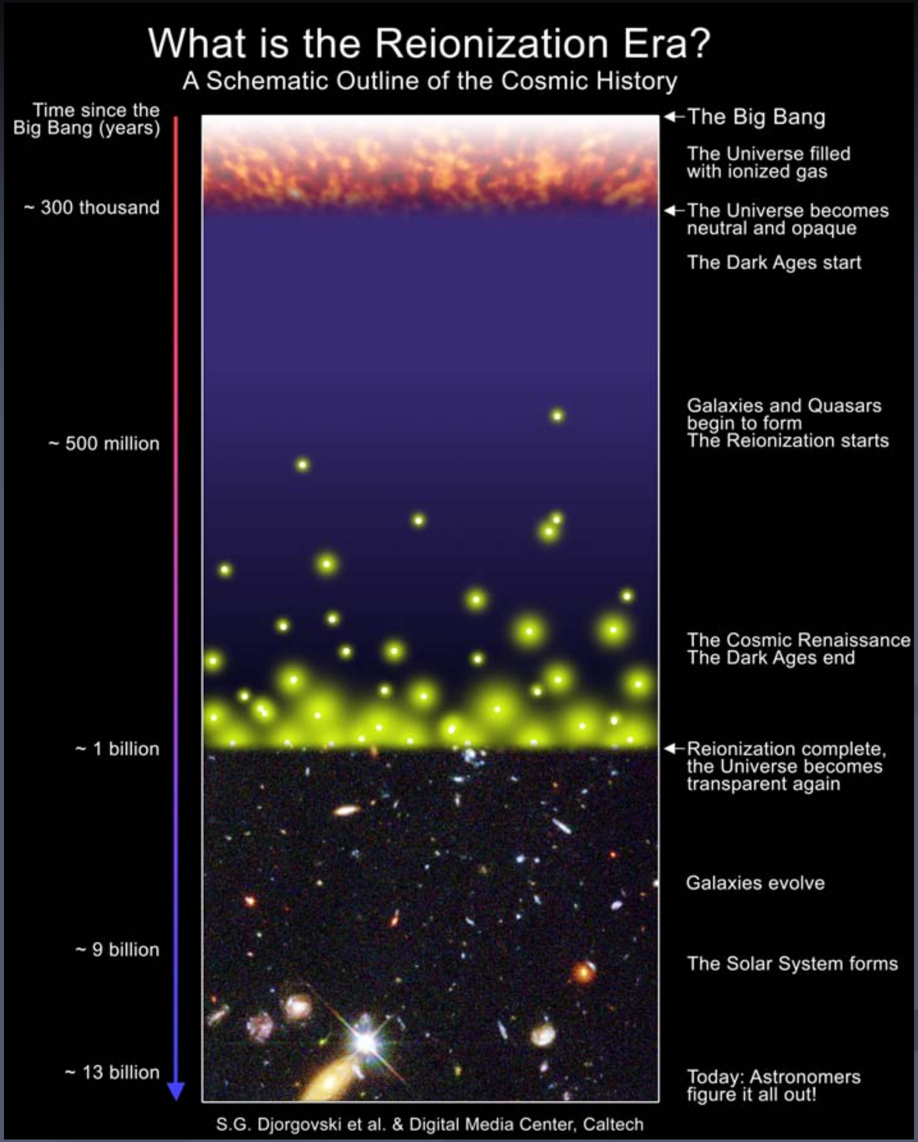

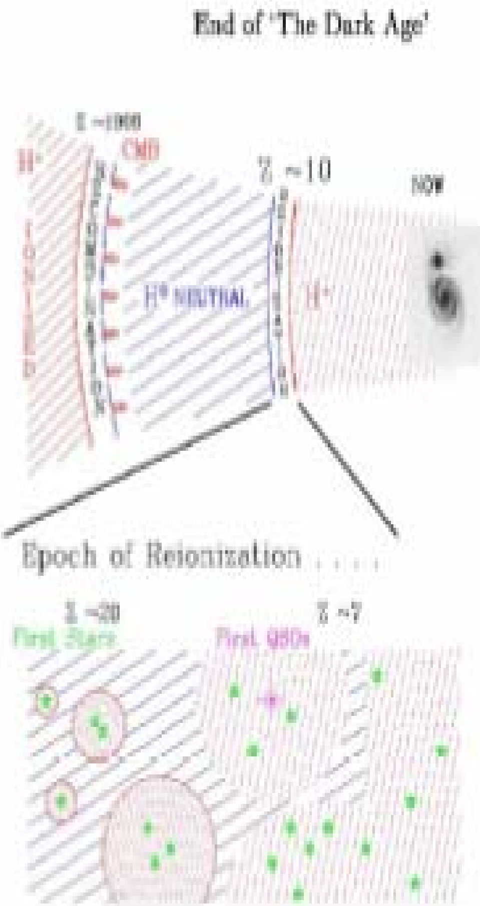

Figure 2.1 Cartoon of the likely development of the early Universe. About 500,000 years after the Big Bang ($z \sim 1000$) hydrogen recombined and remained neutral for a few hundred million years (the "dark ages"). At a redshift, $z \sim 10$, the first stars galaxies and quasars began to form, heating and reionizing the hydrogen gas. LOFAR will be able to observe the global spectral signature of neutral hydrogen close to this epoch of reionization (E-o-R).

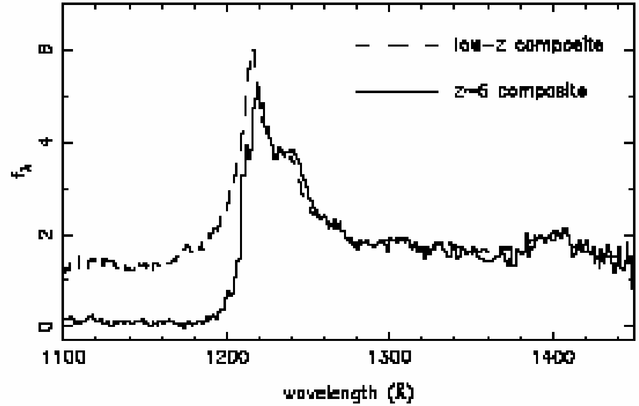

Fig. 3.— The composite spectrum of eleven $z \sim 6$ quasars (solid line). The spectrum of SDSS J0006-0002 was not included because of its low S/N. The spectrum of each quasar is redshifted, scaled according to its m_{1450} magnitude, and averaged with equal weighting. For comparison, we also plot the low-redshift quasar spectral composite from Vanden Berk et al. (2001). The effective redshift in the 1000 – 1200Å range in the Vanden Berk et al. composite is about 2. The quasar intrinsic spectrum redward of Lyα emission shows no detectable evolution up to $z \sim 6$, in terms of both the continuum shape and emission line strengths. On the blue side of Lyα emission, the strong IGM absorption at $z \sim 6$ removes most of the quasar flux.

A Survey of $z > 5.7$ Quasars in the Sloan Digital Sky Survey III: Discovery of Five Additional Quasars[1]

Xiaohui Fan[2,3], Joseph F. Hennawi[3,4], Gordon T. Richards[4], Michael A. Strauss[4], Donald P. Schneider[5], Jennifer L. Donley[2], Jason E. Young[2], James Annis[6], Huan Lin[6], Hubert Lampeitl[6], Robert H. Lupton[4], James E. Gunn[4], Gillian R. Knapp[4], W. N. Brandt[5], Scott Anderson[6], Neta A. Bahcall[4], Jon Brinkmann[7], Robert J. Brunner[8], Masataka Fukugita[7], Alexander S. Szalay[9], Gyula P. Szokoly[10], Donald G. York[11]

$\tau\_reion \geq 0.06$

EXPLORING THE UNIVERSE WITH THE LOW FREQUENCY ARRAY

A SCIENTIFIC CASE

Version 1.00 – 25-September-2002

3 SIGNATURES ON THE CMB

The cosmological reionization leaves imprints on the CMB depending on the (coupled) ionization and thermal history. They can be divided into three categories:[2] (i) generation of CMB Comptonization and free–free spectral distortions associated to the IGM electron temperature increases during the reionization epoch, (ii) suppression of CMB temperature anisotropes at large multipoles, ℓ, due to photon diffusion and (iii) increasing of the power of CMB polarization and temperature-polarization cross-correlation anisotropy at various multipole ranges, mainly depending on the reionization epoch, because of the delay of the effective last scattering surface.

The imprints on CMB anisotropies are mainly dependent on the ionization history while CMB spectral distortions strongly depend also on the thermal history.

[2] Inhomogeneous reionization also produces CMB secondary anisotropies that dominate over the primary CMB component for $l \gtrsim 4000$, and can be detected by upcoming experiments, like the Atacama Cosmology Telescope or Large Millimeter/submillimeter Array (Salvaterra et al. 2005; Iliev et al. 2007).

WMAP 1yr vs 3yr

WMAP 3 yr: τ

for the 4 cases

(WMAP only – All data;

ΛCDM – ΛCDM + run)

$\tau_{best\ fit} \sim 0.07 - 0.1$

$\Delta\tau \sim \pm 0.03$

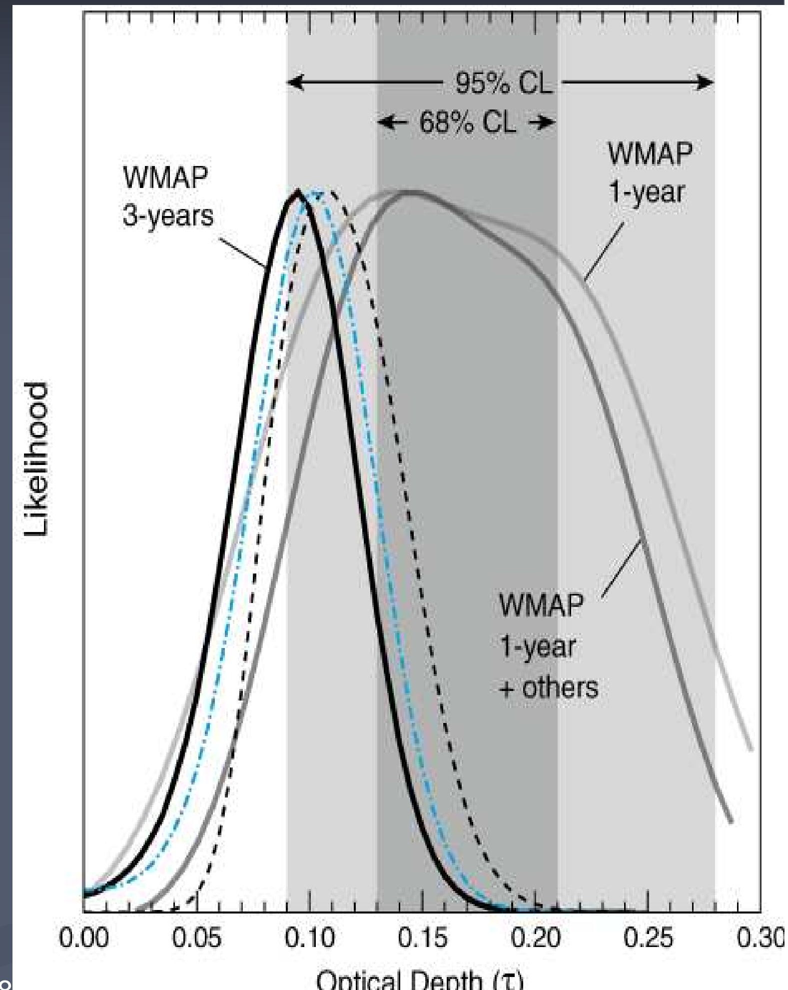

WMAP 5 yr: τ

	WMAP only	~All data
ΛCDM	0.087± 0.017	0.094± 0.016
ΛCDM + run	0.092± 0.018	0.098+0.017– 0.018

for the 4 cases reported here

$\tau_{best\ fit} \sim 0.087 - 0.098$ $\Delta\tau \sim \pm 0.017$

Radiative feedback from reionization

The increase of temperature in ionized region leads to a dramatic suppression of the formation of low-mass galaxies.

Suppression model (CF06): radiative feedback is effective in dark matter haloes with circular velocity below a critical value $v_{crit} \sim (2k_B T/\mu m_p)$ where T is the average temperature of ionizing regions [~ 30 km/s for $T=3\times10^4$ K]

Filtering model (G00): the average baryonic mass within haloes in photoionized regions is a fraction of the universal value (Gnedin 2000):

$$\frac{M_b}{M} = \frac{\Omega_b / \Omega_m}{[1+(2^{1/3}-1)M_C / M]^3}$$

where M_C is the mass of haloes that retain 50% of their gas mass.

Radiative feedback from reionization
has important consequences on structure formation
Different prescriptions for cosmic radiative feedback
produce different reionization history

Reionization model

We implemented these two radiative feedback prescription in a well tested reionization model (Choudhury & Ferrara 2006).

The main features of the model are:

- **Inhomogeneous reionization** assuming lognormal overdensity distribution
- **Sources of reionization**:
  - PopIII stars: Salpeter IMF but metal free (Schaerer 06)
  - PopII stars: Salpeter IMF, Bruzual & Charlot
  - Quasars: important for z<6
- **Chemical feedback** governs the transition from PopIII to PopII stars ($Z_{crit}=10^{-5+/-1}\ Z_{sun}$): the two populations are coeval and PopIII stars can form also at relatively low-z.

Table 1. Best-fitting parameters for models CF06 and G00 shown in Figs 2 and 3. For the same models, we also report the residual volume-averaged neutral hydrogen fraction at redshift six, $x_{\mathrm{H\,I}}(6)$, the volume-averaged electron fraction at redshfit 10, $x_e(10)$ and the Thomson scattering optical depth τ_{el} (see the text).

Model	$\epsilon_{*,\mathrm{II}}$	$f_{\mathrm{esc,II}}$	$\epsilon_{*,\mathrm{III}}$	$f_{\mathrm{esc,III}}$	$x_{\mathrm{H\,I}}(6)$	$x_e(10)$	τ_{el}
CF06	0.10	0.01	0.03	0.68	4×10^{-4}	0.85	0.1017
G00	0.10	0.01	0.01	0.12	3.9×10^{-4}	0.16	0.0631

Observables interpreted by the models

- (a) the volume-averaged electron and HI fraction. The arrows show an observational lower limit from QSO absorption lines at z=6 and upper limit from Ly-alpha emitters at z=6.5
- (b) the cosmic star formation history, with the contribution of Pop III and Pop II stars. Observational data are taken from the compilation of Nagamine et al. (2004)
- (c) the number of source counts above a given redshift, with the observational upper limit from NICMOS HUDF (Bouwens et al. 2005)
- (d) the electron scattering optical depth, with observational constraints from 3-yr WMAP data
- (e) Ly-alpha effective optical depth with data from Songaila (2004)
- (f) Ly-beta effective optical depth with data from Songaila (2004}
- (g) the evolution of Lyman-limit systems with observational data from Storrie-Lombardi et al. (1994)
- (h) photoionization rates for neutral hydrogen, with estimates from numerical simulations - points with errorbars, Bolton et al. (2005)
- (i) temperature evolution of the mean density IGM, with observational data from Schaye et al. (1999)

Gas temperature

Reionization history

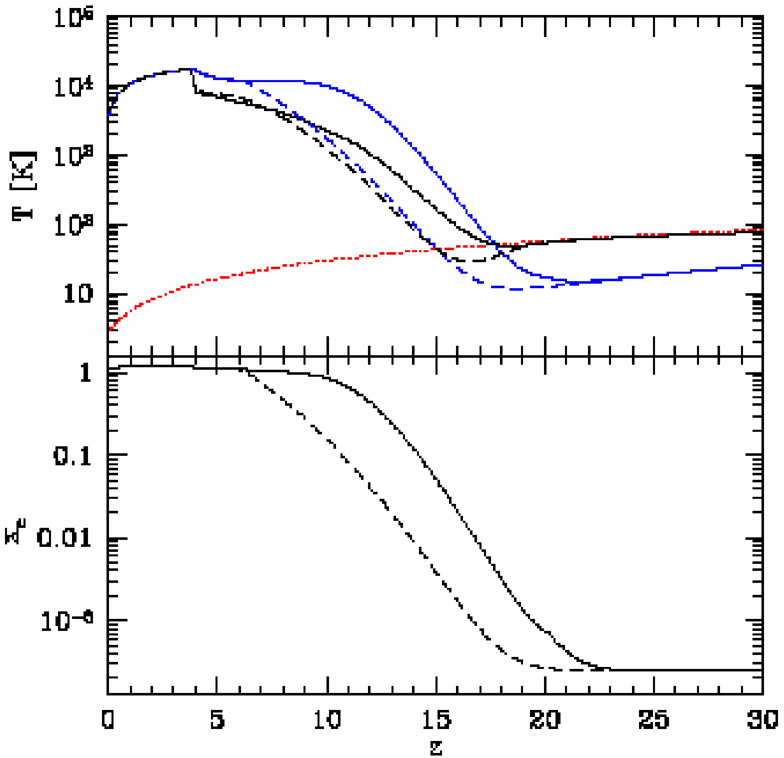

Fig. 1. *Top panel:* redshift evolution of the spin (thick lines) and gas kinetic (thin lines) temperatures predicted by the two models. Solid (dashed) lines refer to suppression (filtering) model. For comparison, we also show the evolution of the CMB temperature T_γ (dotted line). *Bottom panel:* corresponding evolution of the free electron fraction.

Reionization history and temperatures [temperature of gas: kinetic (for CMB) & spin (for 21 cm) & CMB temp.]

CMB anisotropy signal

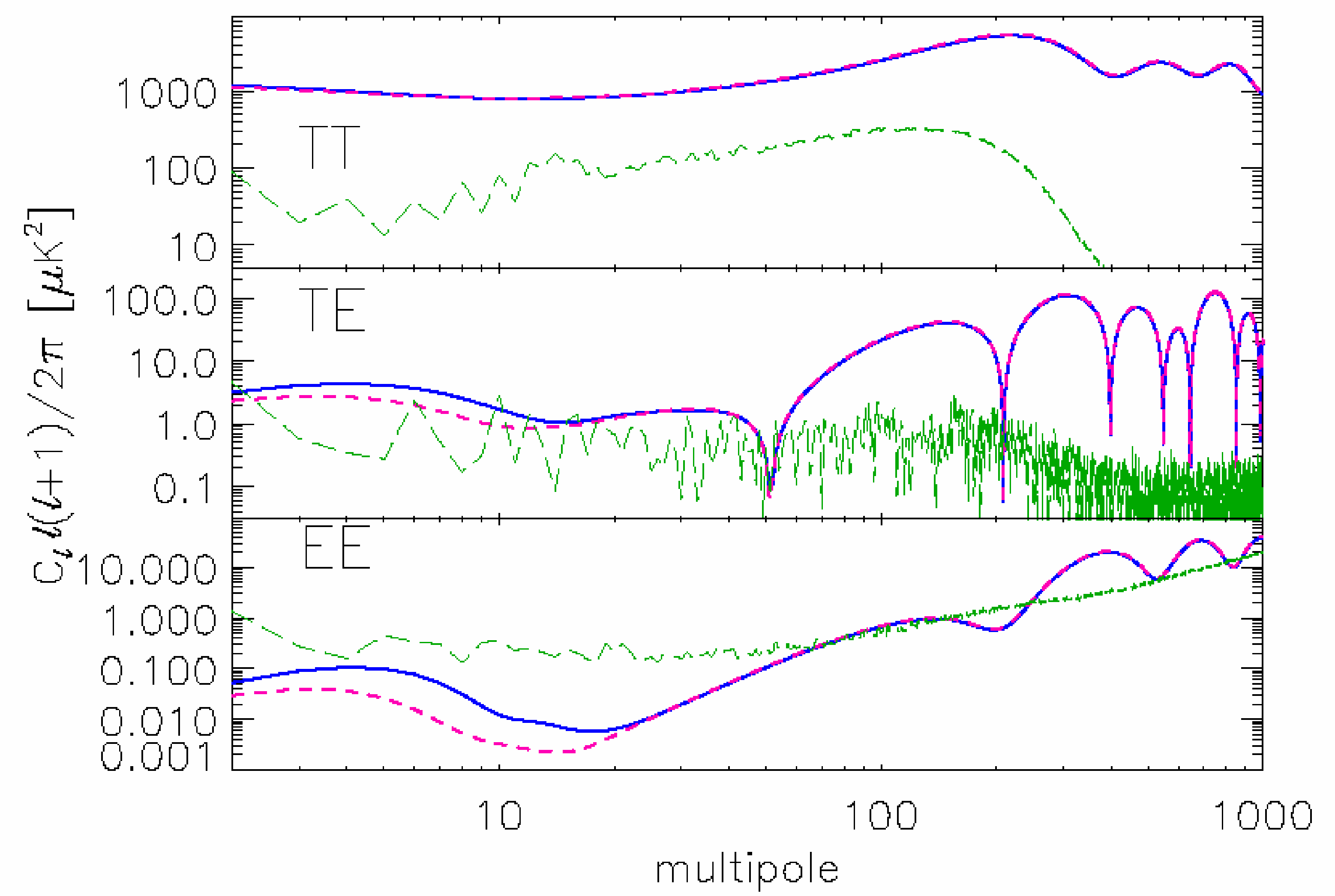

CMB signal (TT, TE): detectability

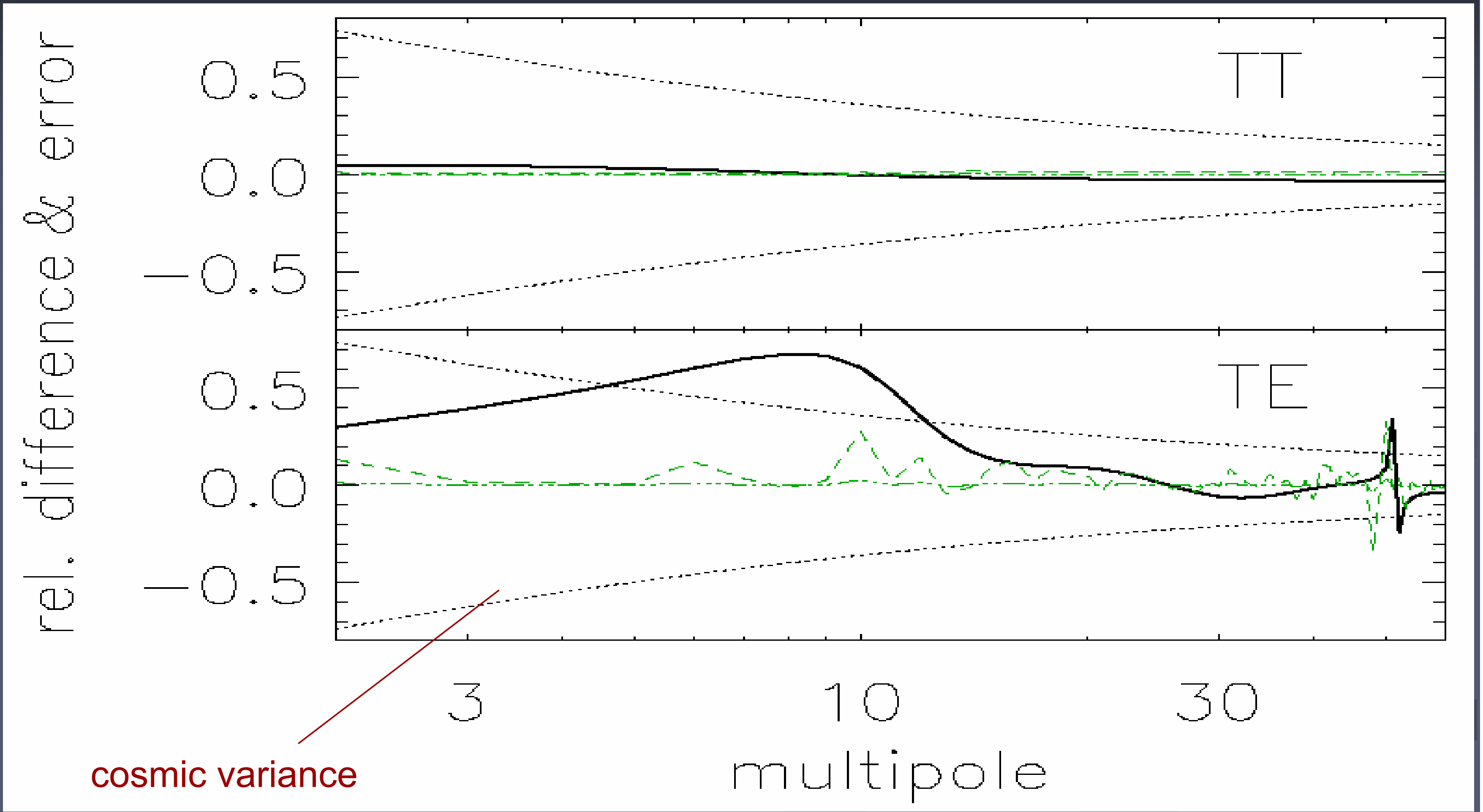

CMB signal (EE): detectability

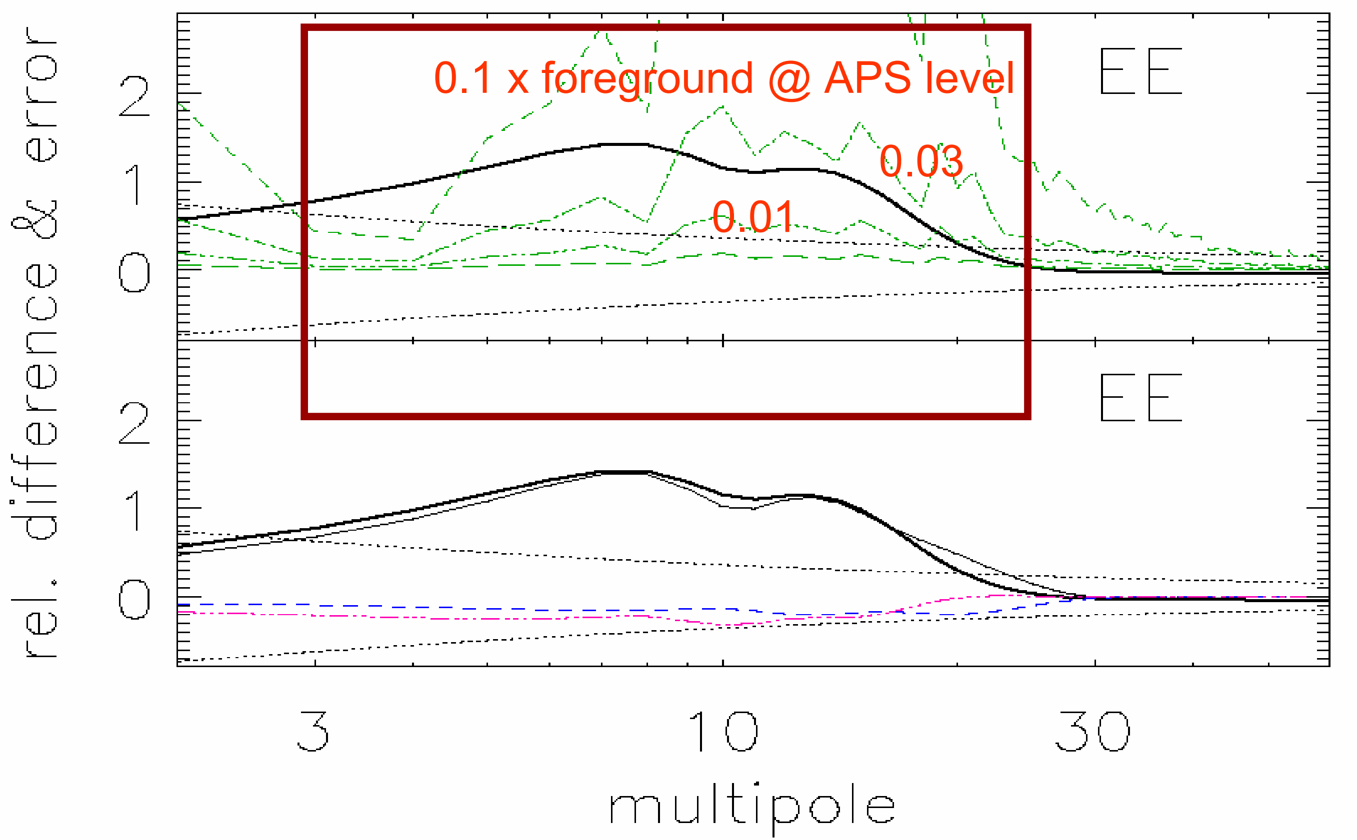

Mon. Not. R. Astron. Soc. 385, 404–410 (2008)
doi:10.1111/j.1365-2966.2008.12845.x

Cosmic microwave background polarization constraints on radiative feedback

C. Burigana,[1,2]★ L. A. Popa,[1,3]★ R. Salvaterra,[4]★ R. Schneider,[5]★ T. Roy Choudhury[6]★ and A. Ferrara[7]★

- WMAP “marginally supports” models closer to the suppression model (τ~0.09)

- <u>Planck</u> with its sensititivy in polarization could firmly discriminate among different radiative feedback models, <u>together with future 21cm observations</u>

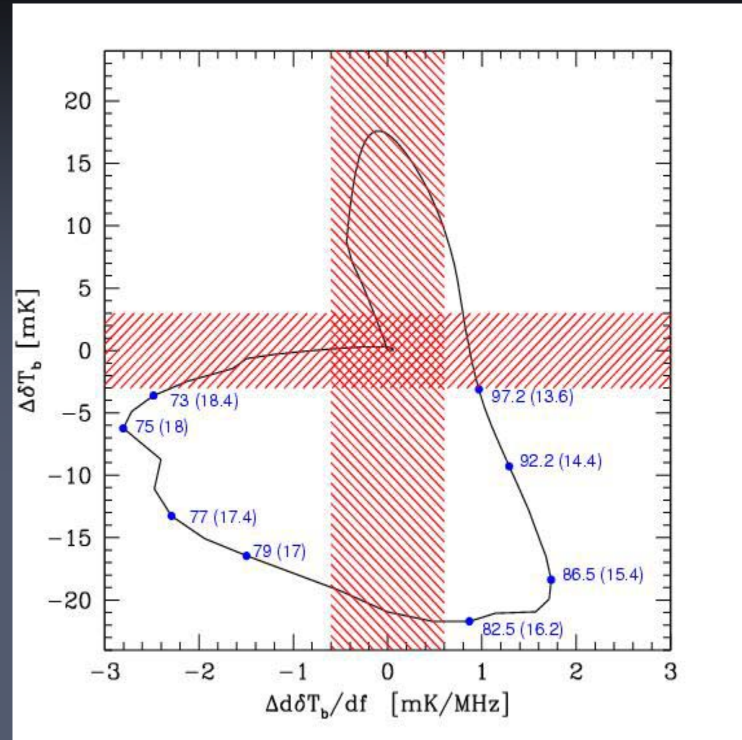

Mon. Not. R. Astron. Soc. 384, 1525–1532 (2008)

Detectable signatures of cosmic radiative feedback

R. Schneider,[1*] R. Salvaterra,[2] T. Roy Choudhury,[3] A. Ferrara,[4] C. Burigana[5,7] and L. A. Popa[5,6]

- Foregrounds should be subtracted at % level in the APS (EE mode) (~10% at map level) to firmly discriminate between the suppression and the filtering model

Clusters & thermal & kinetic SZ effect

Let $I_0 = (2h_P/c^2)(k_B T_{CMB}/h)^3$; n_e=electron density; $x = h_P\nu/k_B T_{CMB}$=dimensionless photon frequency. Neglecting relativistic corrections (Zeldovich Ya.B., Sunyaev R.A., 1969, Ap. Space Sci., 4, 301):

$$\Delta I_{th} = I_0 y g(x) \quad (1)$$

$$\Delta I_k = -I_0 (V_r/c)\tau_e h(x)\,, \quad (2)$$

$$\tau_e = \int n_e \sigma_T dl \quad \text{Thomson optical depth} \quad (3)$$

$$y = \int (k_B T_e/m_e c^2) n_e \sigma_T dl \quad \text{Comptonization parameter} \quad (4)$$

$$h(x) = x^4 e^x/(e^x - 1)^2 \quad (5)$$

$$g(x) = h(x)[x(e^x + 1)/(e^x - 1) - 4]\,, \quad (6)$$

Different frequency dependence $\longrightarrow$ separation through multi-frequency observations

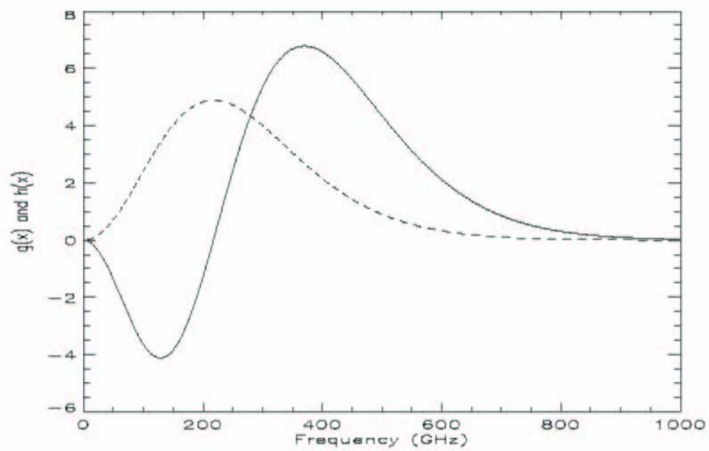

Functions g (solid line) and h (dashes) describing the frequency dependence of the thermal and kinetic SZ effect.

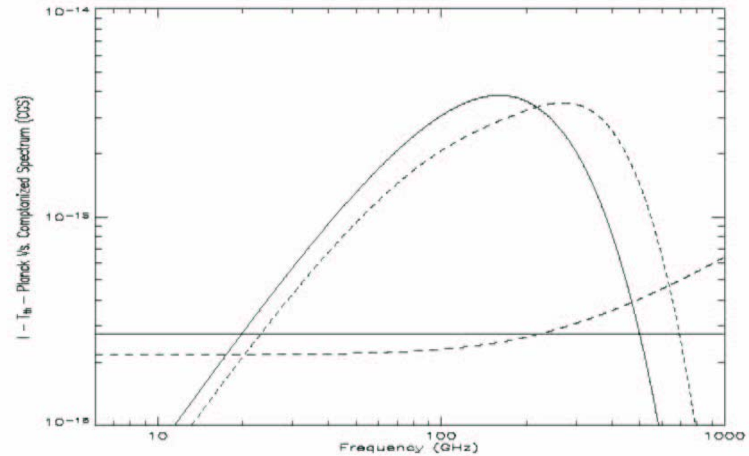

Thermal SZ effect in terms of intensity and equivalent thermodynamic temperature ($y = 0.1$ to "amplify" the effect).

NB:

~ null therm SZ effect @ 217 GHz,
one of the HFI frequency channels

decrement @ lower frequencies
excess @ higher frequencies

FIG 3.4.— Spectrum of the thermal Sunyaev-Zel'dovich effect (red curve, arbitrary units), overlaid with *Planck*'s frequency channels (grey bands). The CMB intensity is increased at frequencies above 217 GHz (i.e., to the right of the vertical blue line) at the expense of lower frequencies. In other words, galaxy clusters cast shadows below 217 GHz and shine above.

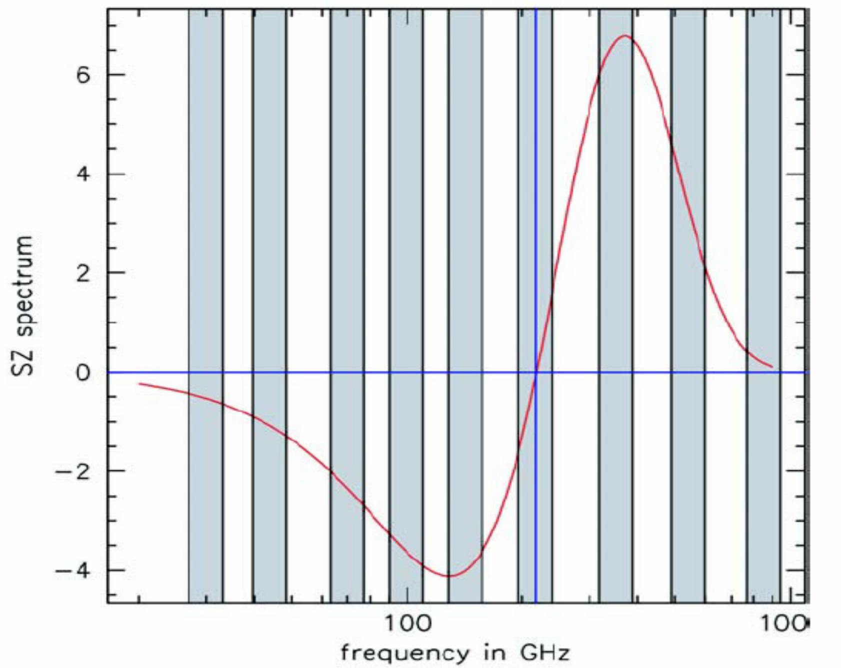

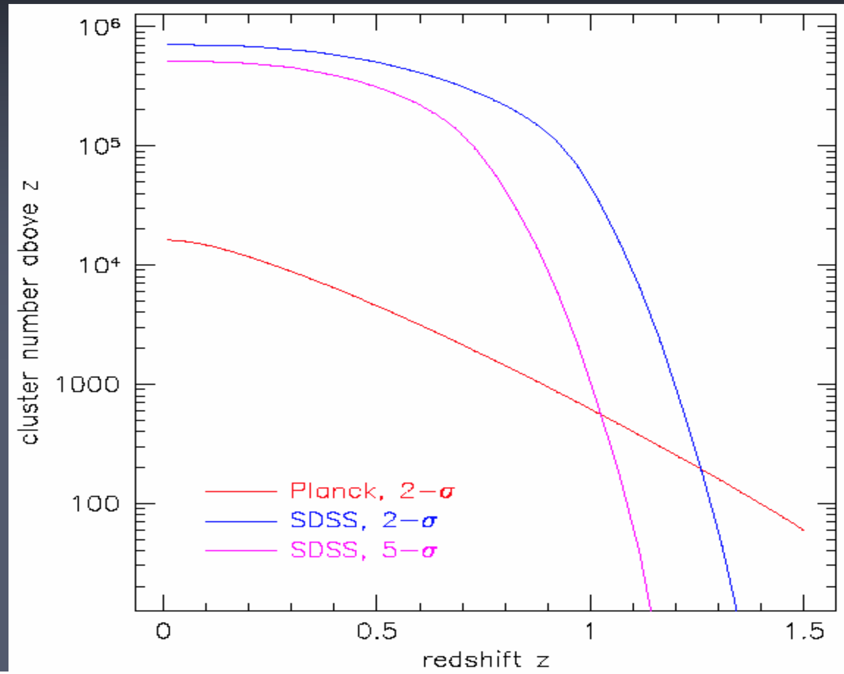

FIG 3.8.—The number of clusters expected to be visible in the optical for the Sloan Digital Sky Survey and in the microwave regime for *Planck* is shown as a function of cluster redshift. In the SDSS area, *Planck* should detect more than 10^4 clusters, almost all of which will also be detected by SDSS. Those *Planck* clusters which will not appear in the SDSS will be at high redshift (adapted from Bartelmann and White 2002).

Up-date estimate: about 5000 new clusters with Planck using its multifrequency

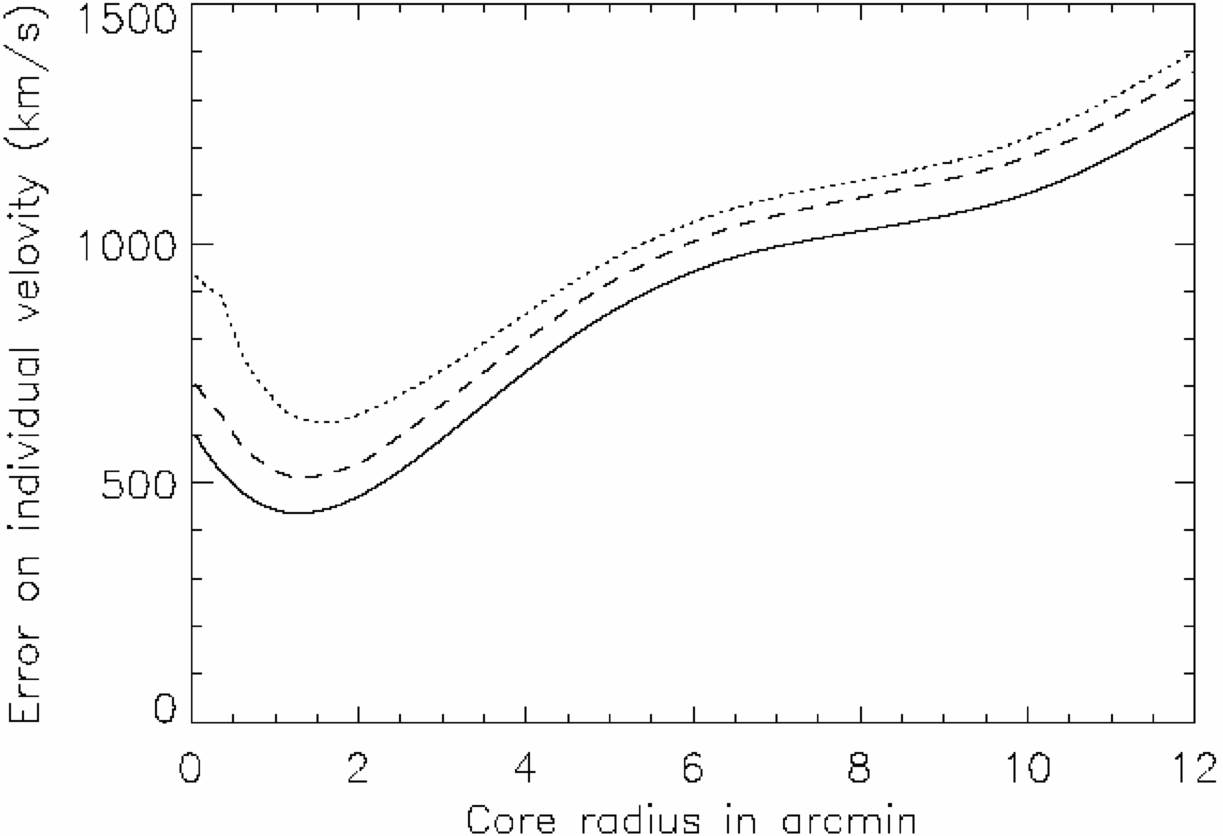

FIG 3.11.—The total rms error in individual cluster velocities, including all contributions (primary CMB, background kinetic SZ, residuals from component separation, Planck-like instrumental noise). The solid, dotted, and dashed lines represent SCDM, OCDM and ΛCDM models, respectively (Aghanim, Górski, and Puget 2001)

Using the adaptive spatial filter, the uncertainty expected in individual velocity measurements on bright clusters falls between 500 and 1000 $\mathrm{km\,s^{-1}}$, depending on the cluster core radius (cf. Figure 3.11). The main sources of error are the CMB itself, instrumental noise, and residuals from component separation. The latter currently appear to dominate, but may be reduced by better foreground-separation techniques.

Extragalactic radiosources detection/extraction

Methods tested on real data!

One Step further: NEWPS 5yr Blind + Non-Blind Approach

Combine the power of both techniques, the Blind and Non-Blind approach

– Application to WMAP –

Simple Blind Detection (SB):

Divide the sky into flat patches
Filter with the MHW2
Detect objetcs SNR > 5 and estimate S
Make histogram of the fluxes of sources
Flag area around 5% brightest sources
Flag a border around the patch
Estimate noise from unflagged pixels

Non-Blind Detection (NB)

Using a list of known positions:
For every object, a patch centered in this posiiton is obtained
Filter with the MHW2
Detect objetcs SNR > 5 and estimate S
Make histogram of the fluxes of sources
Flag area around 5% brightest sources
Flag a border around the patch
Estimate noise from unflagged pixels ONLY in a CORONA around the object

courtesy M. Lopez-Caniego et al.

Combined Blind (CB): First a SB and Second a NB in the Positions of the SB

Summary of the properties of the NEWPS-5yr 5σ catalogue

Areas with σ_{pixel} > 1.5 σ_{median} have been excluded.

	Total	23 GHz	33 GHz	41 GHz	61 GHz
σ_{median} (mJy)		169	206	196	250
Area selected [sr]		10.66	11.12	11.24	11.25
Simple blind detections		405	281	275	147
Additional non-blind detections		28	26	26	14
Total number of objects $\lvert b \rvert > 5°$	516	433	307	301	161
Total number of objects with $\lvert b \rvert < 10°$	51				
Total number of objects within the LMC boundaries	10				
Total number of identified Galactic objects	20	10	12	16	6
Total number of identified extragalactic objects	480	416	287	278	151
Total number of objects missing a consistent counterpart	16	7	8	7	4
Number of sources in WMAP_5yr	352				
Number of sources only in WMAP_5yr	36				

516 different sources: 480 EPS, 20 GS, 16 unidentified - at least 96.9% reliable

In the region covered by NEWPS, WMAP has 388 PS: 356 SNR >5 and 32 SNR < 5

NEWPS-5yr has 164 new sources not in WMAP-5yr: from them, only 14 may be false

We recover the 64 objects of Chen & Wright (08) and the objects by Nie & Zhang (07)

NEWPS-5yr Number Counts

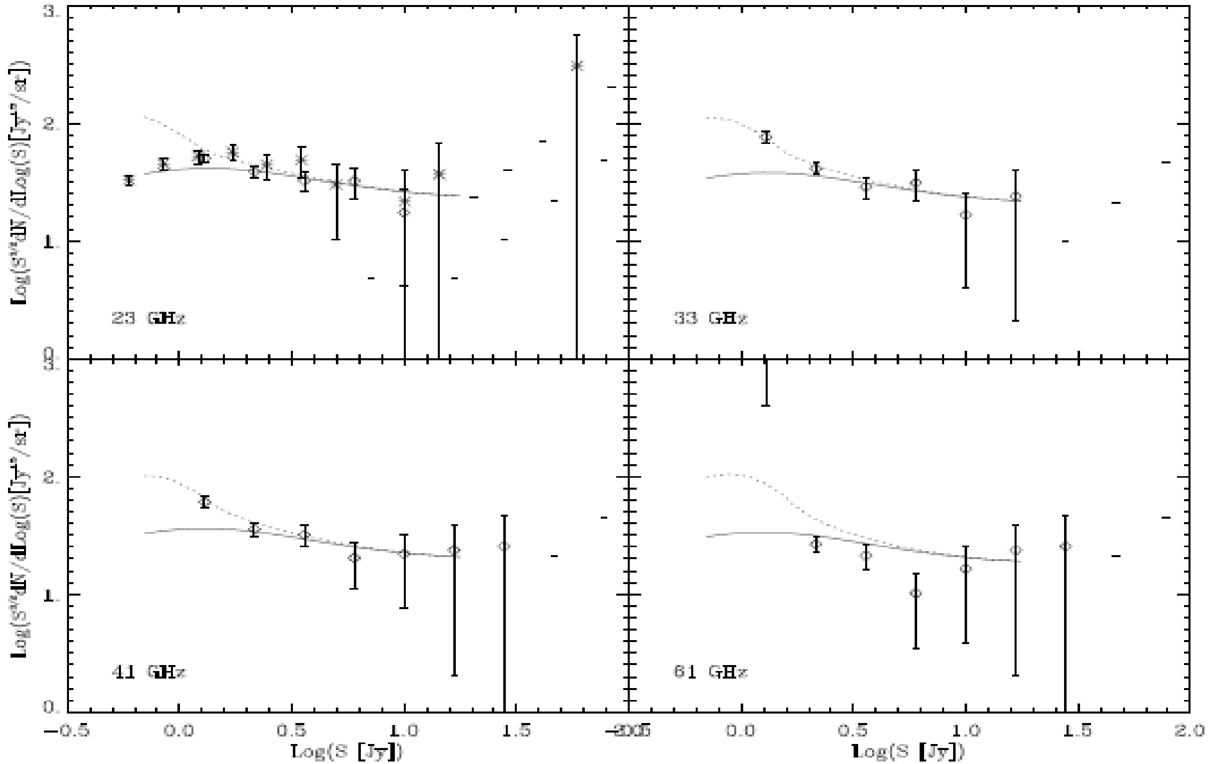

Figure 7. Differential WMAP counts, normalized to $S_{\rm Jy}^{-2.5}$, estimated from the WMAP data (diamonds). The 23 GHz counts are compared with the ATCA 20 GHz ones (asterisks). The solid line shows the predictions of the model by De Zotti et al. (2005). The dotted line illustrates the effect of the Eddington bias by showing the model counts convolved with a Gaussian error distribution with $\sigma = 0.34$, 0.42, 0.4, 0.5 Jy at 23, 33, 41, and 61 GHz, respectively. The value of σ at 23 GHz was obtained by comparison with the BSS measurements. At higher frequencies we assumed that the true errors on flux measurements are twice the median errors yielded by the simple blind approach, as found at 23 GHz. The convolution has been computed integrating down to a minimum flux equal to $S/10$.

courtesy M. Lopez Caniego et al.

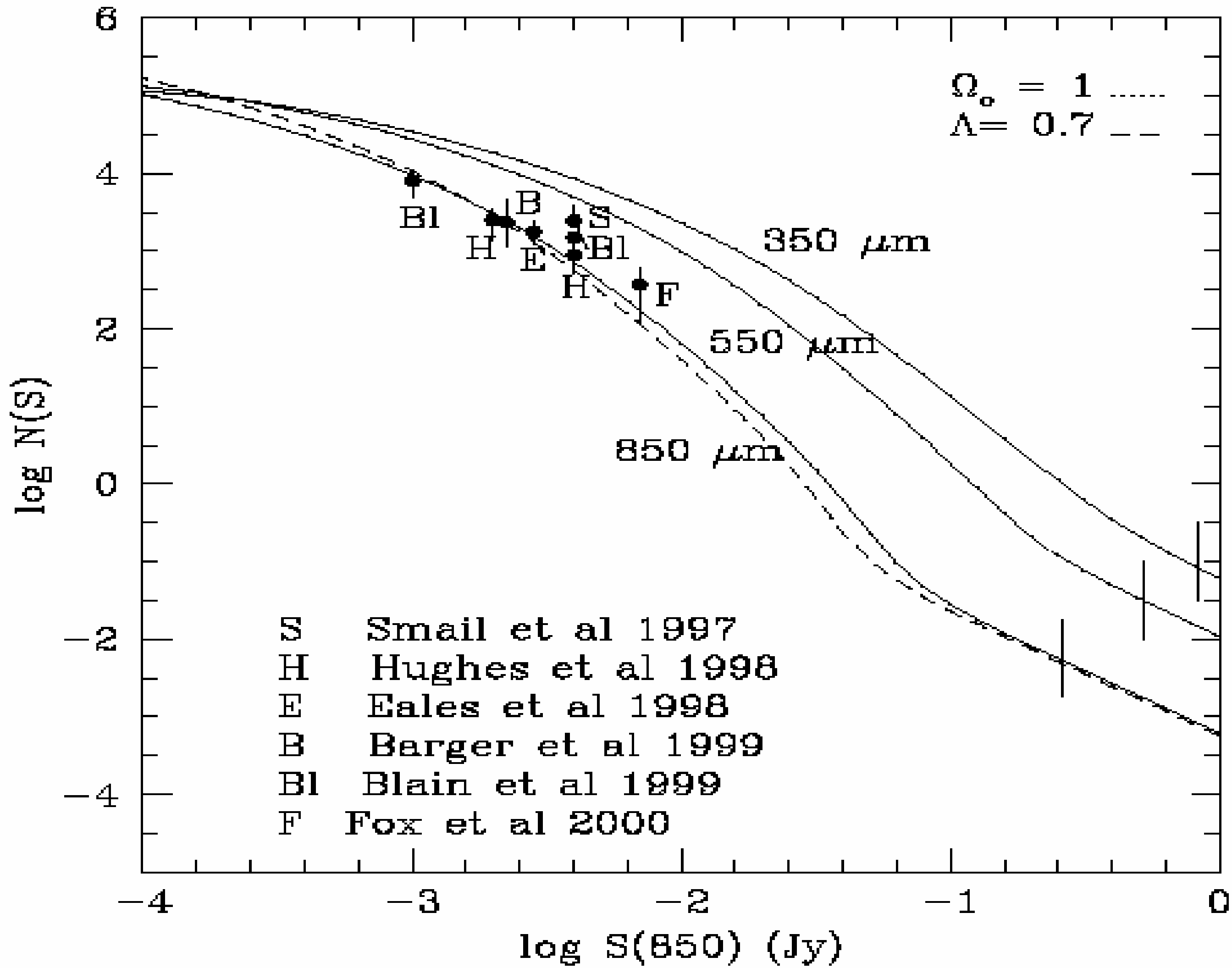

FIG 4.11.— Predicted counts at 350, 550 and 850 μm (Rowan-Robinson 2001). Observed counts at 850 μm are shown, and the *Planck* sensitivity is indicated by the vertical bars.

Extra-galactic radio-sources (LFI)

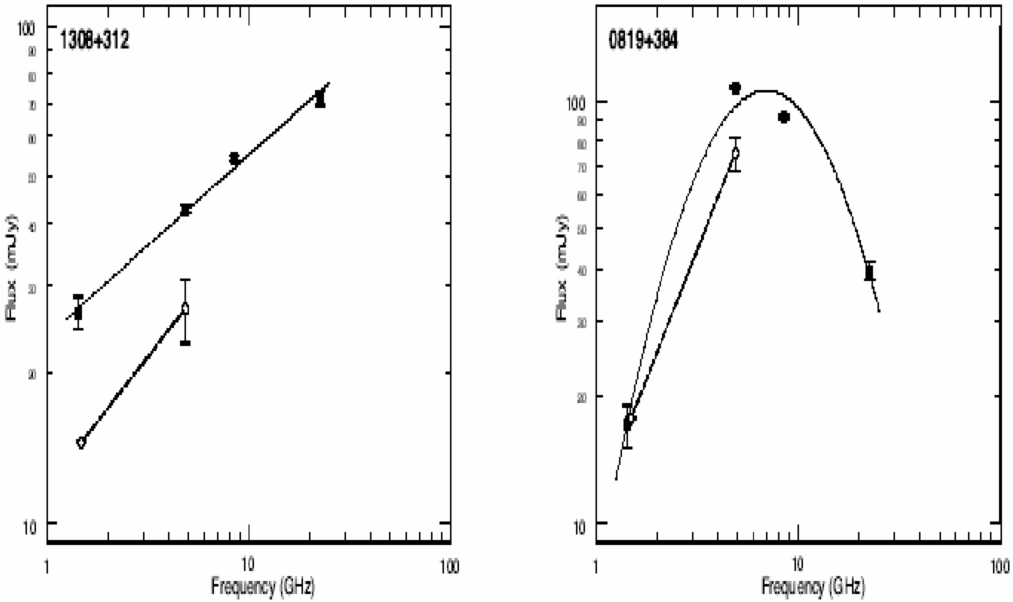

FIG 4.2.— Radio frequency spectra of two atypical radio sources. One is a GPS source.

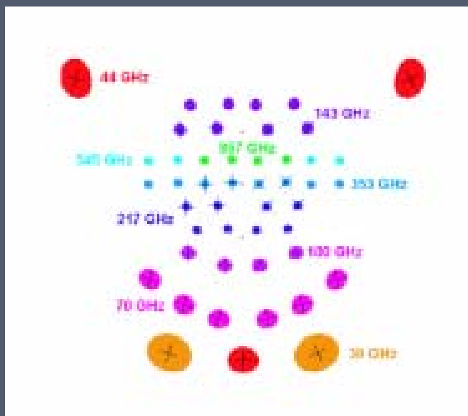

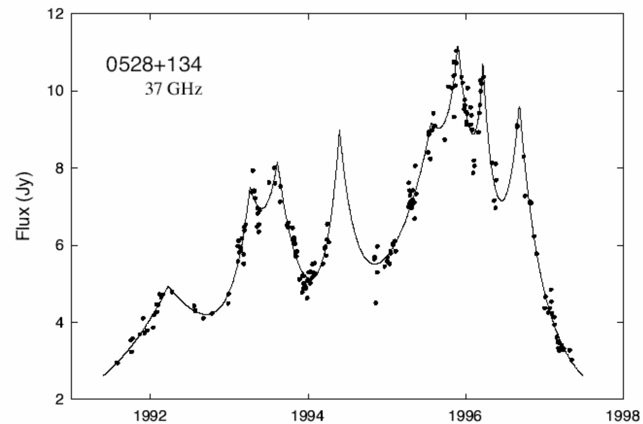

FIG 4.6.— Observations of a highly variable radio source, compared with a fitted model based on exponential flares. From Valtaoja et al. 1999.

Extragalactic far-IR sources (HFI)

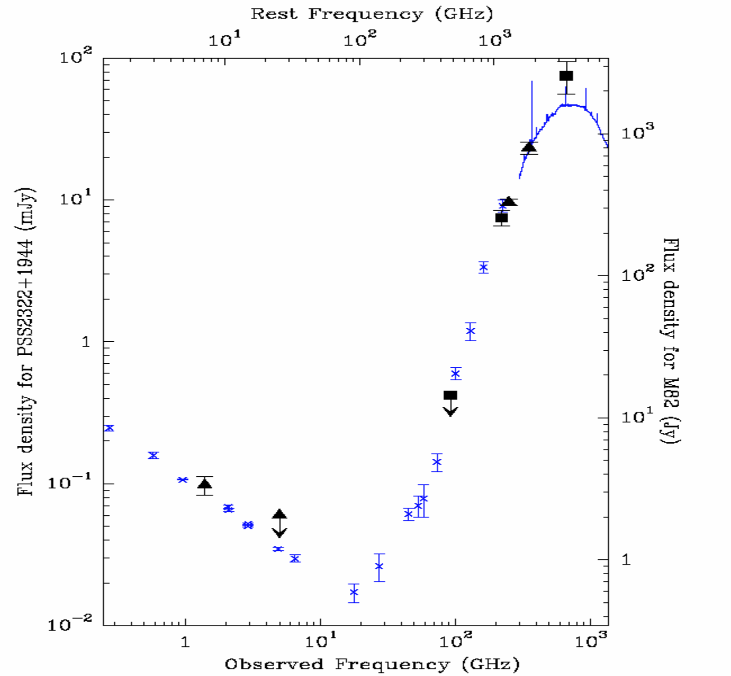

FIG 4.8.— Spectral energy distribution of PSS 2322+1944 (black points, from Cox et al. 2002). For comparison, the radio-to-infrared spectral energy distribution of the starburst galaxy M 82 is shown, redshifted to $z = 4.12$ and normalized to the flux density of PSS 2322+1944 at the observed wavelength of 850 μm. The crosses show all the currently available photometric data, and the continuous line represents the ISO LWS spectrum. The left- and right-hand flux density scale are adapted for PSS 2322+1944 and M 82, respectively.

PLANCK GALAXY SURVEYS

	FREQUENCY [GHz]				
	143	217	353	550	850
Confusion limit [mJy, 3σ]	6.3	14.1	44.7	112	251
Planck All Sky Survey sensitivity [mJy, 3σ]	26	37	75	180	300
Planck Deep Survey sensitivity [mJy, 3σ]	10	18.4	49	170	280
Number of galaxies [all sky]	570	860	1700	4400	35000

Galactic diffuse foreground maps

Ancillary Surveys (to be used in the analysis of *Planck* maps)

Survey type	Survey	Resolution [′]	Coverage	Status
CO	Composite CFA ^{12}CO[a]	8′	$-10° < b < +10°$	Completed
	FCRAO(CGPS) ^{12}CO[b]	0.′8	$+74° < l < +147°$ $-3°6 < b < +5°6$	In progress
	Nagoya U. $^{12/13}$CO[c]	2.′7	$-10° < b < +10°$	In progress
HI	Dwingeloo/NFRA[d]	30′	Full Sky	Completed
	CGPS/DRAO[e]	1′	$+74° < l < +147°$ $-3.°6 < b < +5.°6$	In progress
	HIPASS/HIJASS	15′	Full Sky	In progress
IR	2MASS 1.25/2.2 μm	0.06′	Full Sky	Completed
	IRAS 12/100 μm[f]	4′	Full Sky	Completed
	DIRBE 1.25/240 μm	30′	Full Sky	Completed
	MSX 4/26 μm[g]	0.′3	$-5° < b < +5°$	Completed
	ISO Serendipitous 170 μm[h]	2′	15% sky	Completed
	IRIS/ASTRO-F 50/200 μm[i]	0.′8	Full Sky	Future
	SIRTF 24/160 μm[j]	0.′27	Maps	In progress
	ELISA-balloon 200/600 μm[k]	3′	$-20° < b < +20°$	Future
	Herschel 100/600 μm	0.′5	1000 deg^2	Future
H-alpha	WHAM-Fabry-Perot[l]	60′	Northern sky	In progress
	SHASSA-filter[m]	5′	Southern sky	In progress
	Manchester WFC-filter[n]	5′		Future
Radio	Stockert/Bonn 1.4 GHz[o]	34′	Northern sky	Completed
	Halslam 408 MHz[p]	50′	Full Sky	Completed
	FIRAS 100/1000 μm	420′	Full Sky	Completed
	DMR 90/30 GHz	420′	Full Sky	Completed
	WMAP 22/90 GHz	20′	Full Sky	In progress
	Bonn MLS 1.4/2.7 GHz[q]	10′	$-10° < b < +10°$	In progress
	HatRAO 2.3 GHz[r]	20′	Southern sky	In progress
	CGPS/DRAO 408/1420 MHz[s]	1′	$+74° < b < +147°$ $-3.6° < b < +5.6°$	In progress
	Green Bank 8.35/14.35 GHz[t]	5′	$-5° < b < +5°$	In progress
X-ray	ROSAT 0.1-4 keV[u]	12′/2°	Full Sky	Completed
γ-ray	CGRO >100 MeV[v]	120′	Full Sky	Completed
	INTEGRAL <10 MeV	60′	$-15° < l < +15°$	Future

[a] Dame et al. 2001, ApJ, 547, 792
[b] Heyer et al. 1998, ApJ Supp., 115, 241
[c] Fukui et al., www.a.phys.nagoya-u.ac.jp
[d] Burton, W. B. 1985, AA S., 62, 365
[e] English et al. 1998, PASA, 15, 56
[f] Wheelock, S. et al. 1994, JPL Pub. 94-11
[g] Price S., 1995, Space Sci. Rev., 74, 81
[h] Bogun et al., 1996, A&A, 315L, 96
[i] Murakami H., et al., 1994, ApJ , 428, 354
[j] sirtf.caltech.edu
[k] Ristorcelli 2001, in *The Promise of FIRST*
[l] Reynolds et al. 1998, PASA 15, no. 1, 14
[m] Gaustad, J. et al. 1998 IAU Symp. 190, 58
[n] Boumis P et al. 2000, MNRAS 320, 61
[o] Reich P. & Reich W., 1986 A&A S 63, 205
[p] Haslam C.G.T. et al. 1982 A&A 100, 209
[q] Reich et al. 1997 A&A Suppl 126, 413
[r] Jonas J.L. et al. 1998 MNRAS 297, 977
[s] English et al. 1998, PASA, 15, 56
[t] Langston et al. 2000, AJ, 119/6, 2801
[u] Snowden et al., 1997, 485, 125
[v] Hunter, S. D., et al. 1997, ApJ., 481, 205

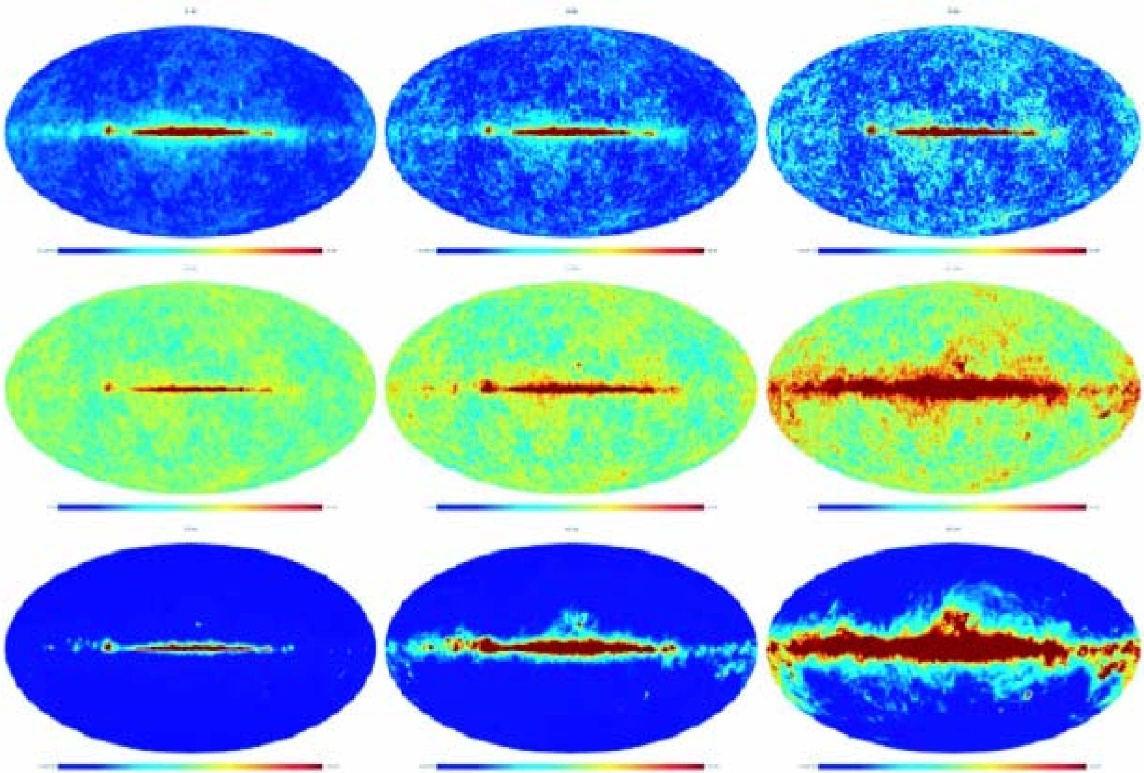

FIG 5.1.— False colour images of the simulated sky in the nine frequency channels of *Planck*, after subtraction of the monopole and dipole CMB components. From top left to bottom right: 30, 44, 70, 100, 143, 217, 353, 545, and 857 GHz channels.

Detailed characterization of Galactic diffuse components

- 1. Synchrotron: pattern, spectral behaviour
- 2. Free-free: its relevance in particular close to the Galactic plane
- 3. Thermal dust: cold, warm components
- 4. Anomalous emission (spinning dust?)
- 5. (?) DM annihilation
- → Galactic magnetic fields

  (ordered vs turbolent components)
- Dust grain properties
- ISM history

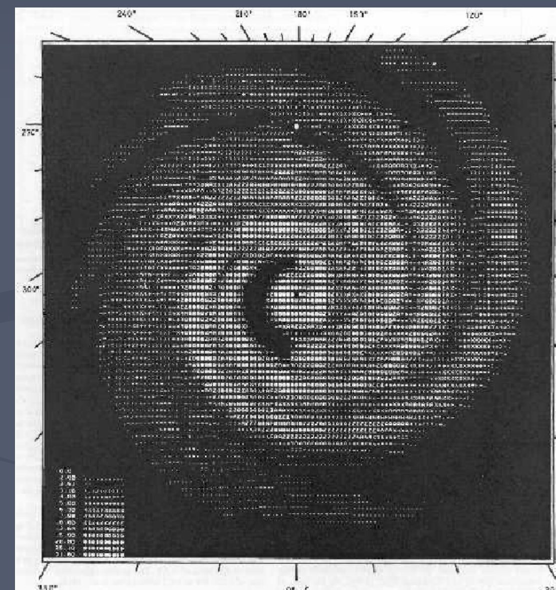

FIG 5.7.— Top view of the 3-D model of synchrotron emissivity derived from the Haslam map by Beuermann et al. (1985). The model contains assumptions on the Galactic magnetic field orientation and degree of alignment along the spiral arm, and therefore can be used to synthesize a map of synchrotron polarisation around the Sun (filled circle).

Synchrotron Polarization

- info from radio surveys
- info from WMAP
- Relevance of Planck

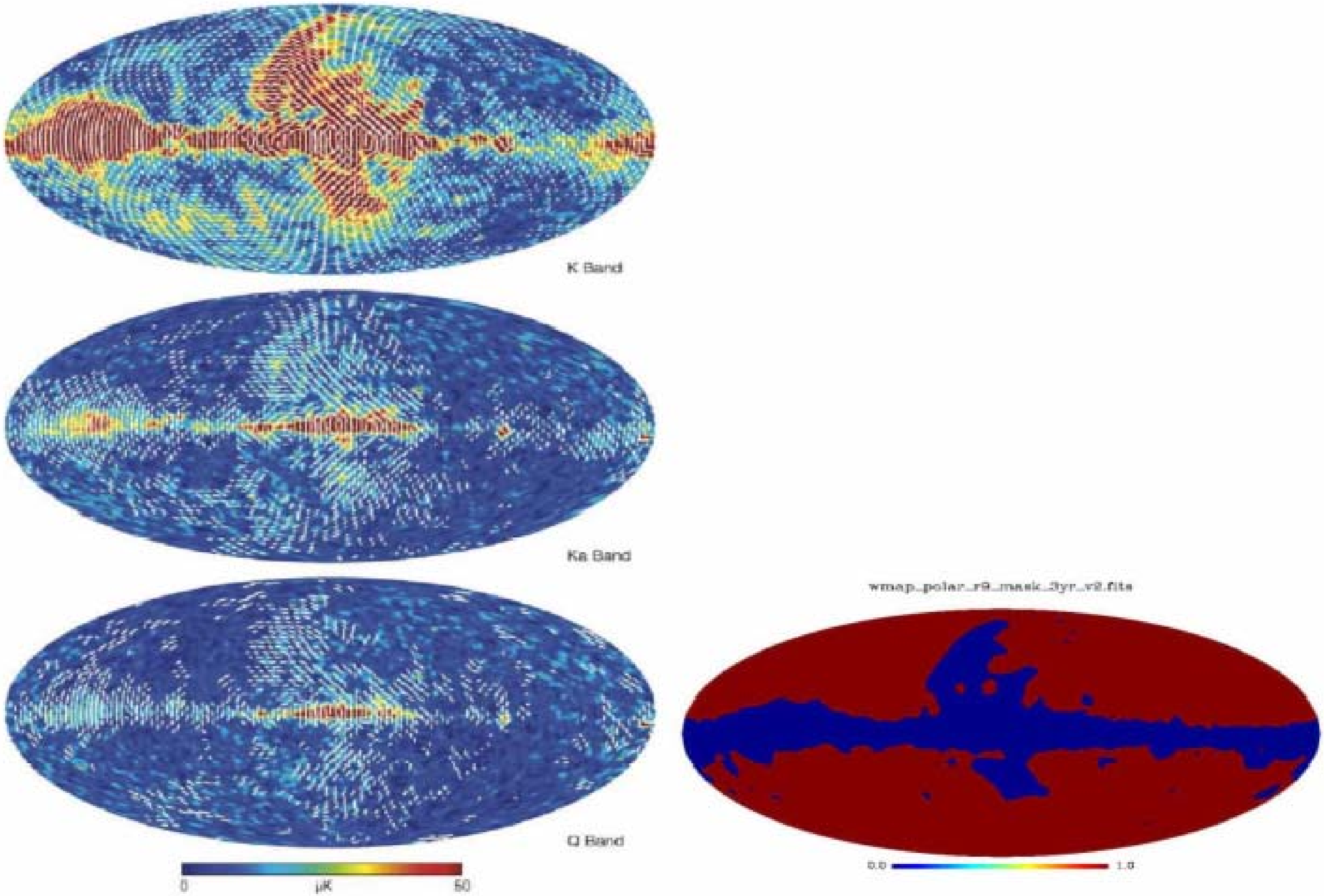

WMAP 3 yr Pol. maps and mask.

Polarization: Comparison of radio 1.4 GHz surveys with WMAP

PI @ 1420 MHz (n_{side}=512)

Polarized Intensity

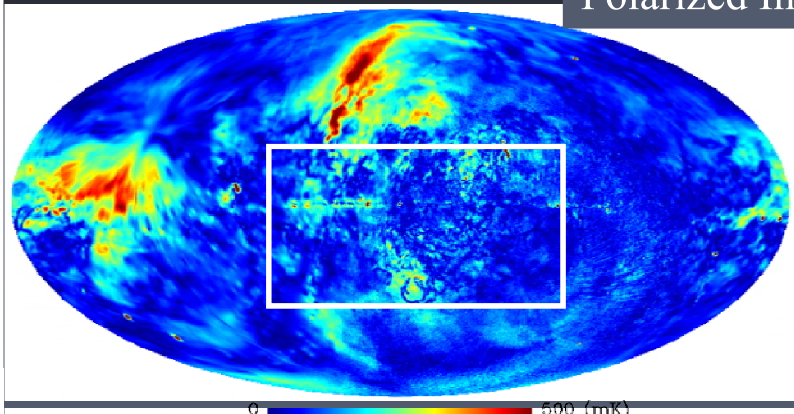

Polarized Intensity

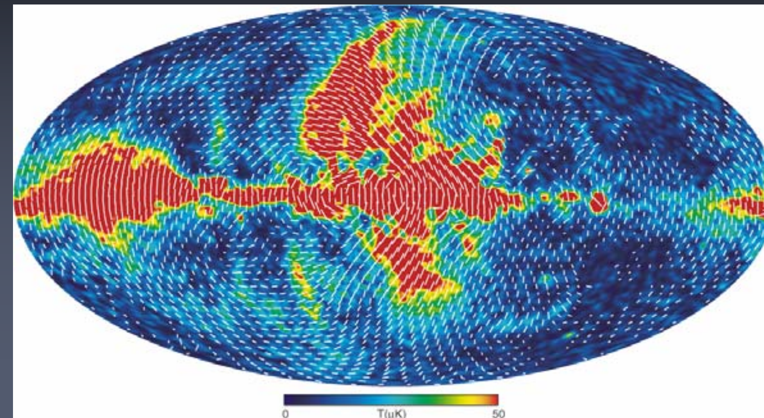

Polarization Angle @ 1.4 GHz

Polarization Angle

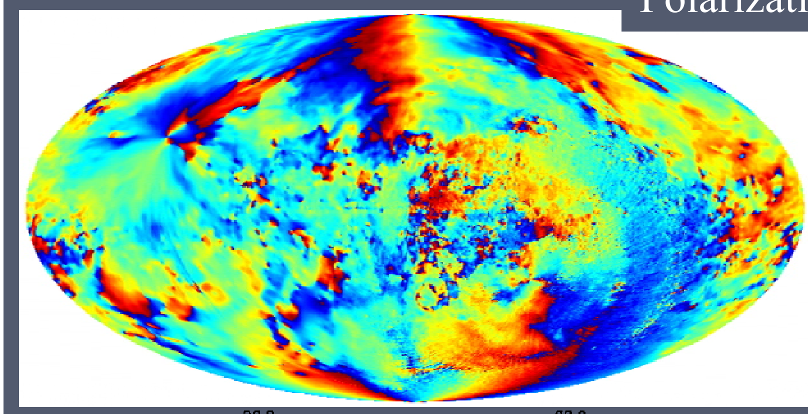

Polarization Angle + 90°

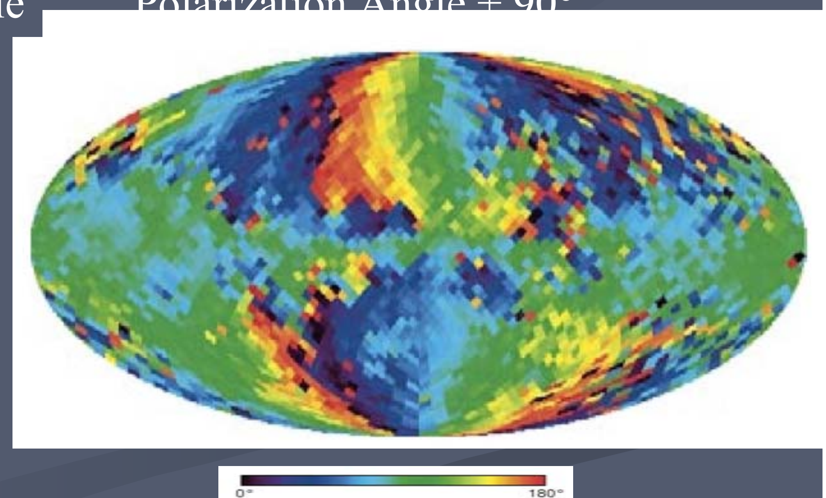

1.4 GHz *[Reich et al., in preparation]*

WMAP 23 GHz
[Page et al. 2006]

Polarization: Comparison with WMAP

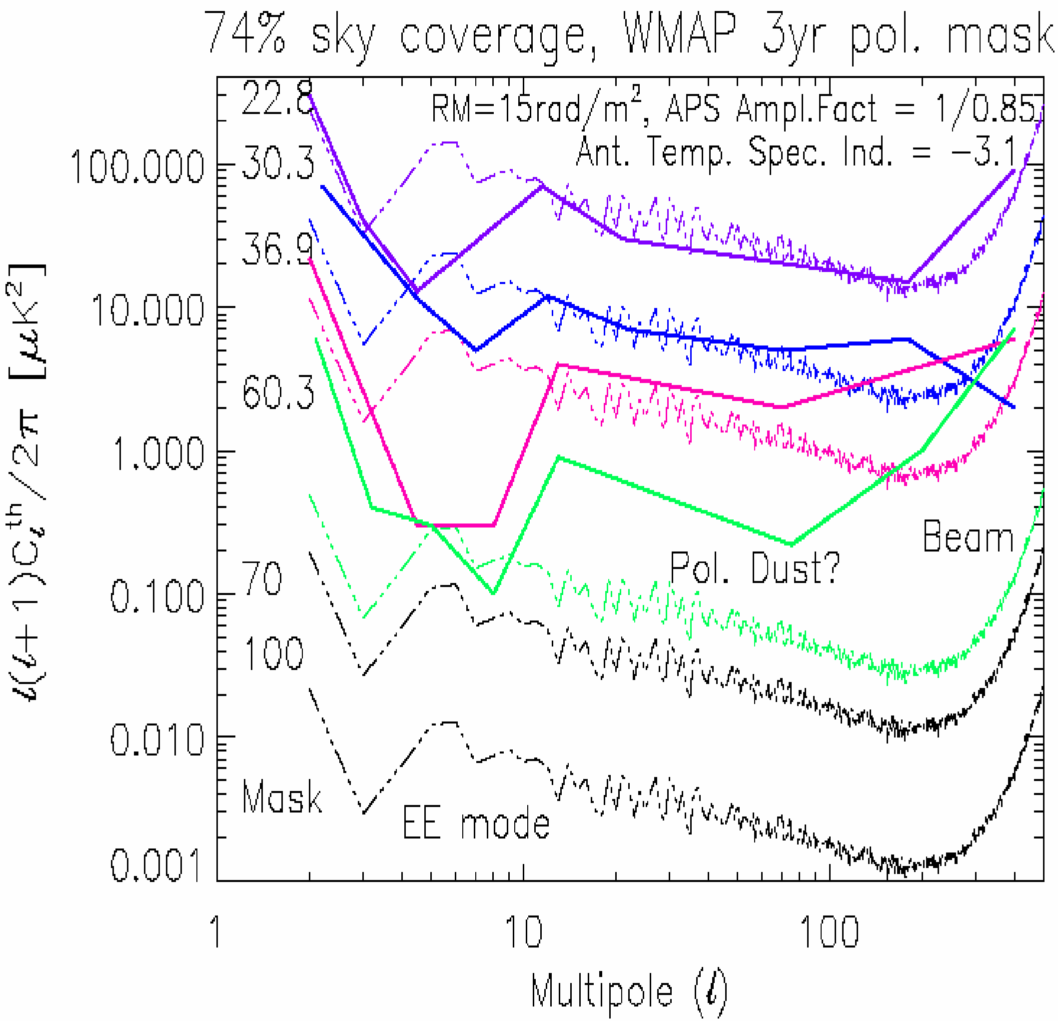

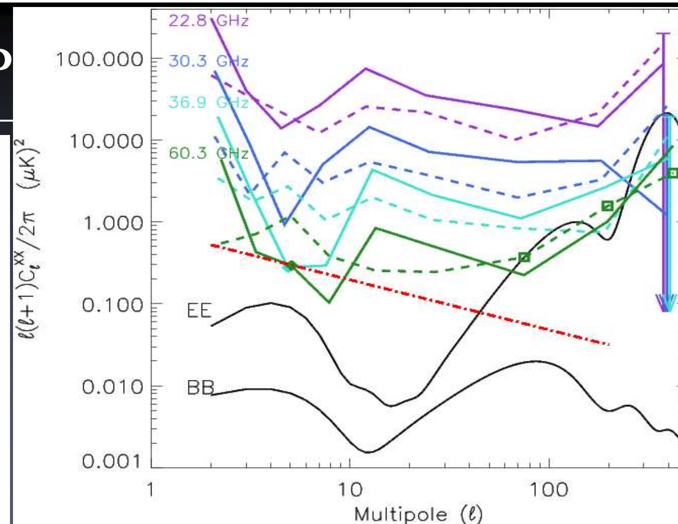

In agreement with WMAP results at intermediate ℓ (~ 10-100) within a factor ~ 2 or better, @ ν ≤ of about 40 GHz. Dust important @ higher ν

1.4 GHz new polarization maps good template of the large scale synchrotron emission

Burigana et al. 2006, PoS(CMB2006)016

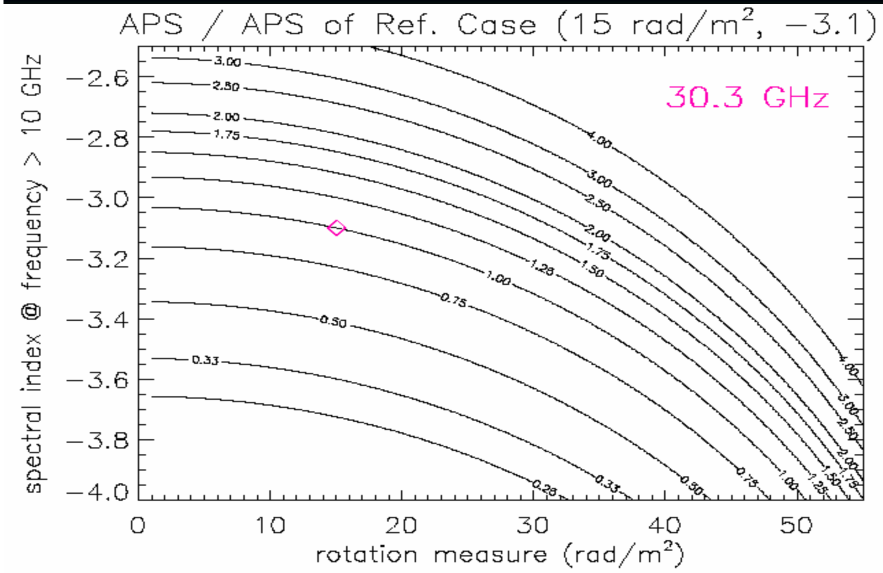

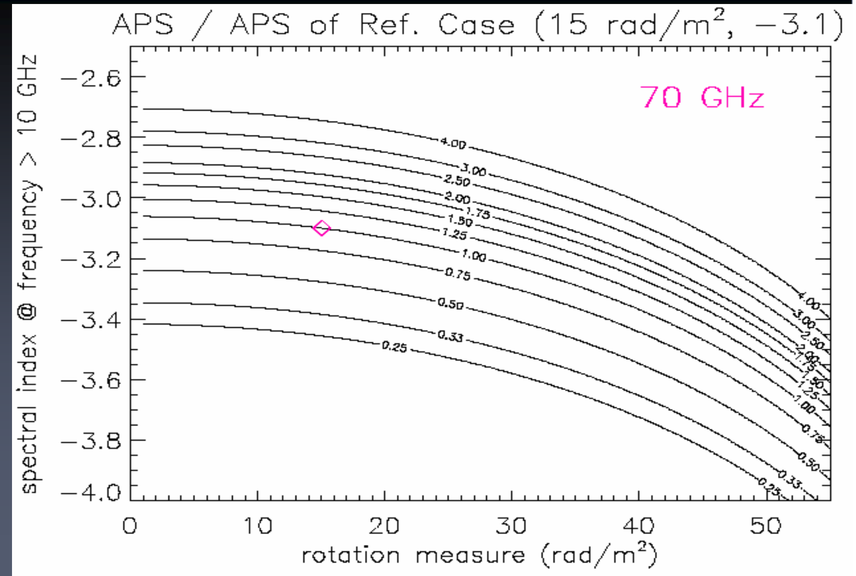

"Averaged" Faraday depolarization vs spectral index steepening

- **Assume "spatial" (i.e. average of cells within beam & along line of sight) depolarization to be almost the same at the radio & microwave ν**
- **Consider "average" Faraday depolarization at APS level**
- **Assume a possible steepening of synchrotron frequency spectrum above a certain ν**

<u>Relevance of multifrequency:</u>

certainly at higher frequency the accuracy on synchrotron degrades,

but the "parameter space" compatible with observations within a certain factor decreases

DM annihilation & synchrotron?

Modelling synchrotron emission by DM annihilation

- Dark matter may consist of some new particle
- (SUSY) provides a good candidate
  - neutralino χ,
  - lightest supersymmetric stable particle,
  - linear combination of higgsino, Z-ino photino states
  - fermion
  - WIMP

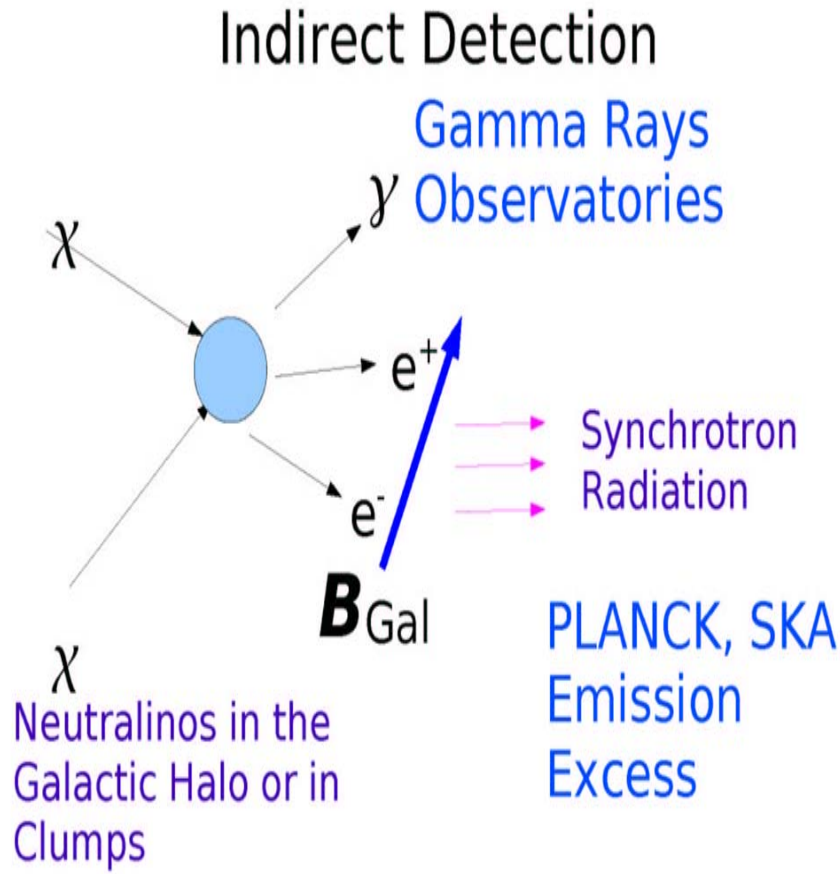

Simulation of Clumps at Planck Frequencies

- Model of DM Clumps
- Spectrum of Neutralinos from DarkSUSY software
- Diffusion of electrons in the Galactic Magnetic field
- Brightness integral of Sync. Emission
- Work by Blasi et al. 2003

Detectability of Clumps

- Comparison with Sync. Emission in the Reference Sky Model plus Planck noise.
- Simple detection mechanism: localized excess of emission respect to the neighbor background (open photometry).
- For simple detection, detection probability between 70% and 90% at 44 GHz
- Much lower at 30 GHz and 70 GHz.

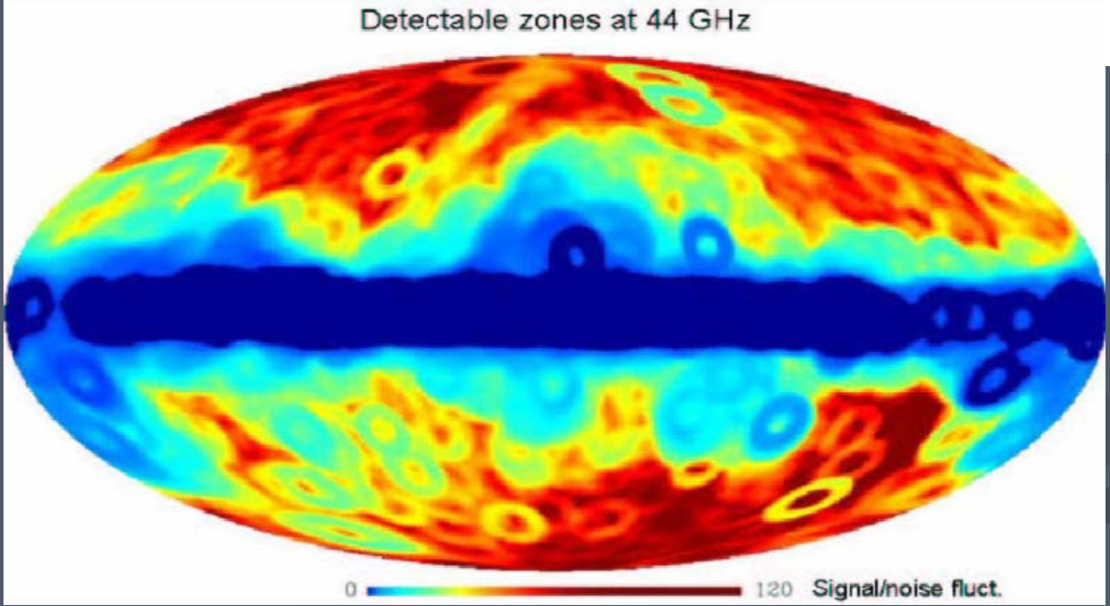

Galactic sources

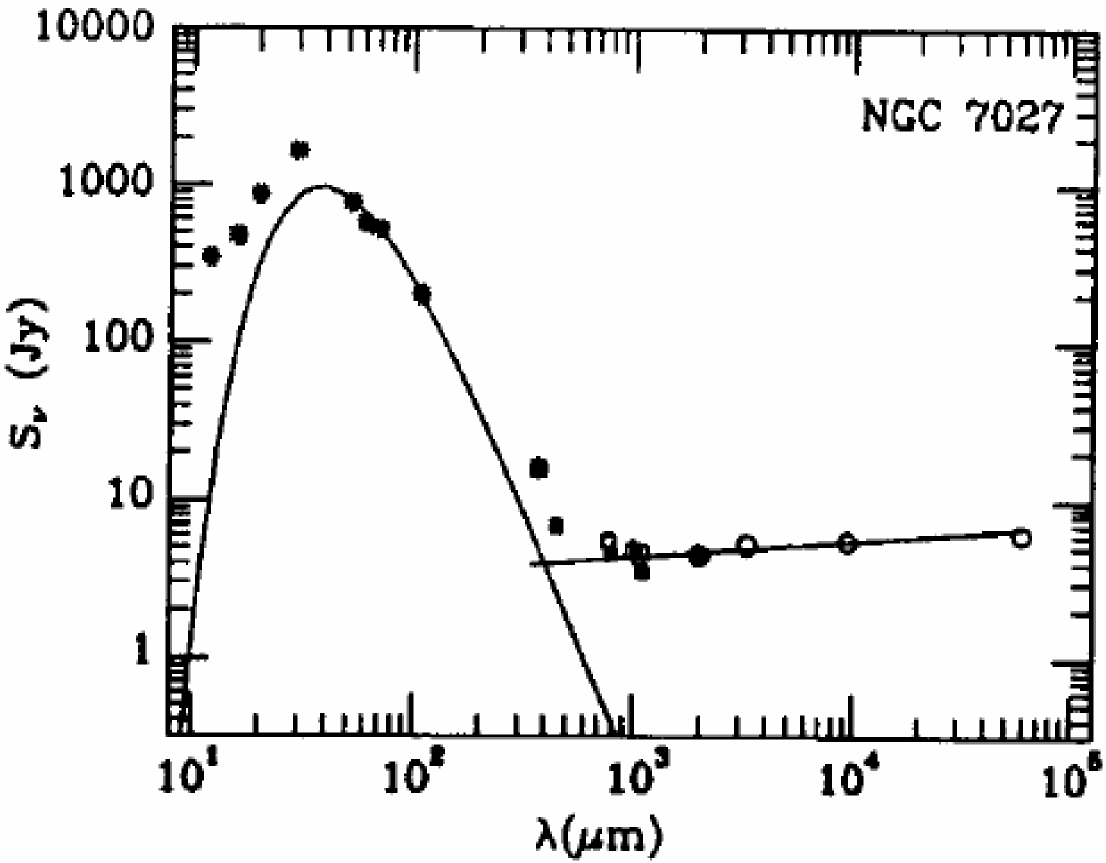

FIG 5.5.— The SED of the young planetary nebula NGC 7027 (reproduced from Hoare, Roche and Clegg, 1992). Thermal emission from dust dominates the IR-mm part of the spectrum, while the contribution of free-free emission from the ionized envelope is evident in the radio.

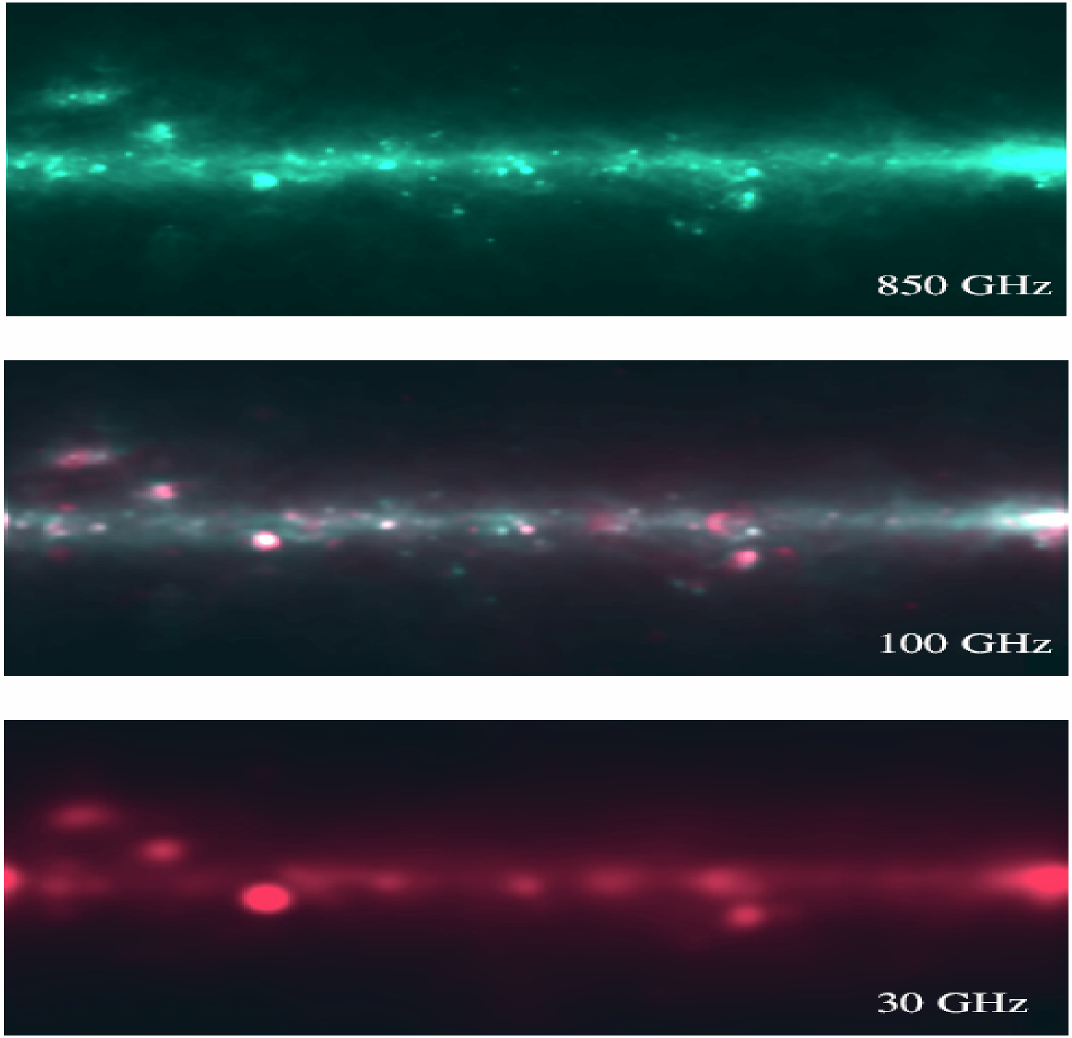

FIG 5.6.— Simulated maps of the dust and free-free emission in *Planck* bands at 850, 100, and 30 GHz. This is a $20^\circ \times 10^\circ$ map centered at $(l, b) = (10^\circ, 0^\circ)$. The free-free contribution (red) is derived from the Bonn 2.7 GHz survey (Reich et al. 1997); the dust contribution (blue) is derived from IRAS 100 μm data. A single dust temperature ($T = 25$ K, $n = 1.5$) and a single radio power law ($\alpha = -0.16$) were assumed. The angular resolutions used are respectively $5'$, $9'$, and $30'$.

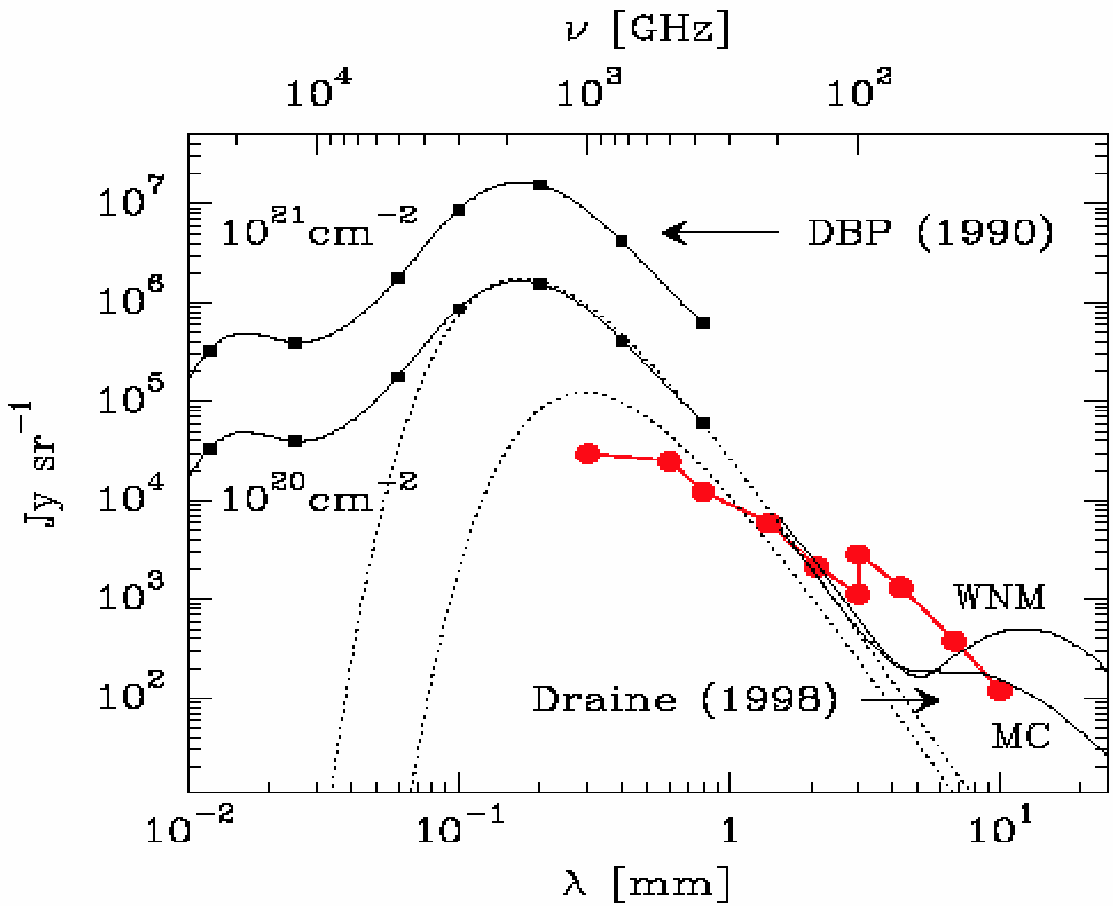

FIG 5.4.— Predicted dust emission from interstellar clouds. In the far-infrared part of the spectrum, solid lines indicate the predicted thermal dust emission for hydrogen column densities 10^{20} and 10^{21} cm^{-2} (Désert, Boulanger, Puget 1990). At longer wavelengths, predictions for spinning dust emission from the warm neutral medium and molecular clouds are shown for column density 10^{20} cm^{-2} (Draine and Lazarian 1998). The dotted lines are $\nu^2 B_\nu(T)$ spectra at temperatures 10 K (lower curve) and 17 K. The red curve indicates the predicted sensitivity of *Planck* (1σ in one year).

Solar System Science

NUMBER OF DETECTABLE MAIN BELT ASTEROIDS[a]

R/d	Differential Number	Cumulative Number[b]
$1–2 \times 10^{-7}$	299	397
$2–3 \times 10^{-7}$	76	98
$3–4 \times 10^{-7}$	15	22
$4–5 \times 10^{-7}$	4	7
$R/d > 5 \times 10^{-7}$	0	3

[a] The lower threshold considered here for asteroid detection is set to a radius to distance ratio $R/d \sim 10^{-7}$, derived by assuming a typical asteroid temperature of $\sim 150\,\mathrm{K}$ and by taking into account the *Planck* sensitivity at different channels (see Cremonese et al. 2003 for details).

[b] The cumulative number is computed at the lower limit of the range listed for the differential number.

ZLE with *Planck*

FIRAS Spectra

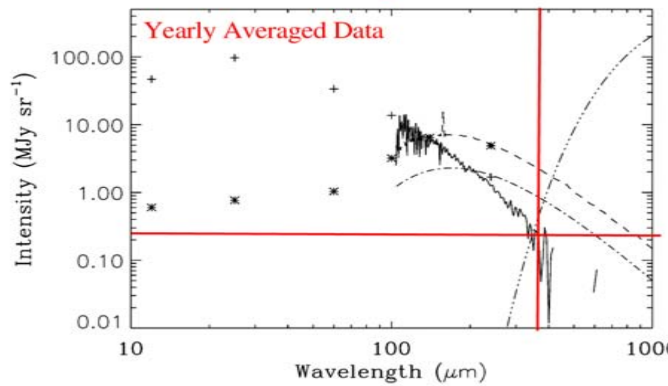

Fixsen, Dwek, 2002 ApJ, 578, 1009

WG7 Meeting - 16 Jan 2007– Catania - Italy – EU *Maris, Burigana. - ZLE and Planck* 7

ZLE COBE/DIRBE MAP

12 µm, ecliptic projection

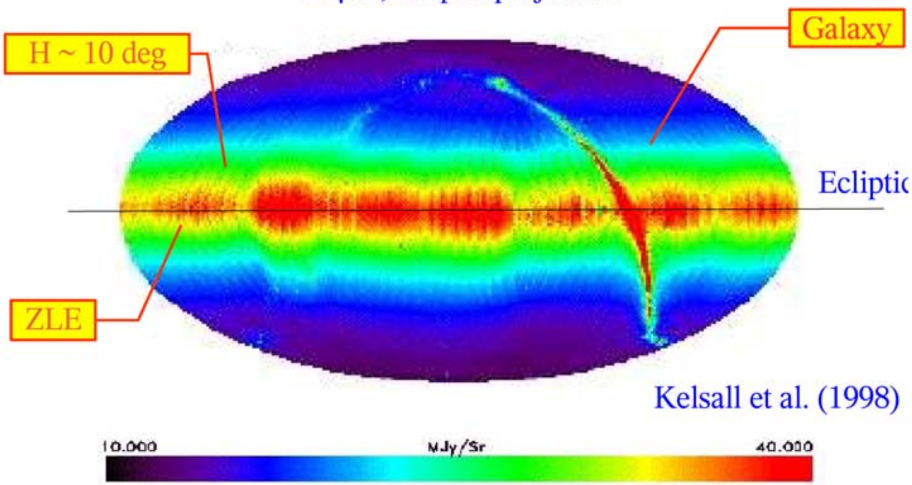

Kelsall et al. (1998)

WG7 Meeting - 16 Jan 2007– Catania - Italy – EU *Maris, Burigana. - ZLE and Planck* 4

Two Components Signal $F_f(P)$

f = Frequency (857 GHz, 550 GHz, …)

Pointing — Planck Position

$$F_f(P, R_P) = E_f\, Z_f(P, R_P) + G_f(P) + n$$

Emissivity Correction — Spatial Pattern — Galaxy

Function of size distribution and grains properties

E_f(Smooth) ~ 0.5

E_f(Secondary) ~ 1±0.2

Black Body emission averaged for grains spatial density

WG7 Meeting - 16 Jan 2007– Catania - Italy – EU *Maris, Burigana. - ZLE and Planck* 8

Multifrequency Galaxy v.z. ZLE

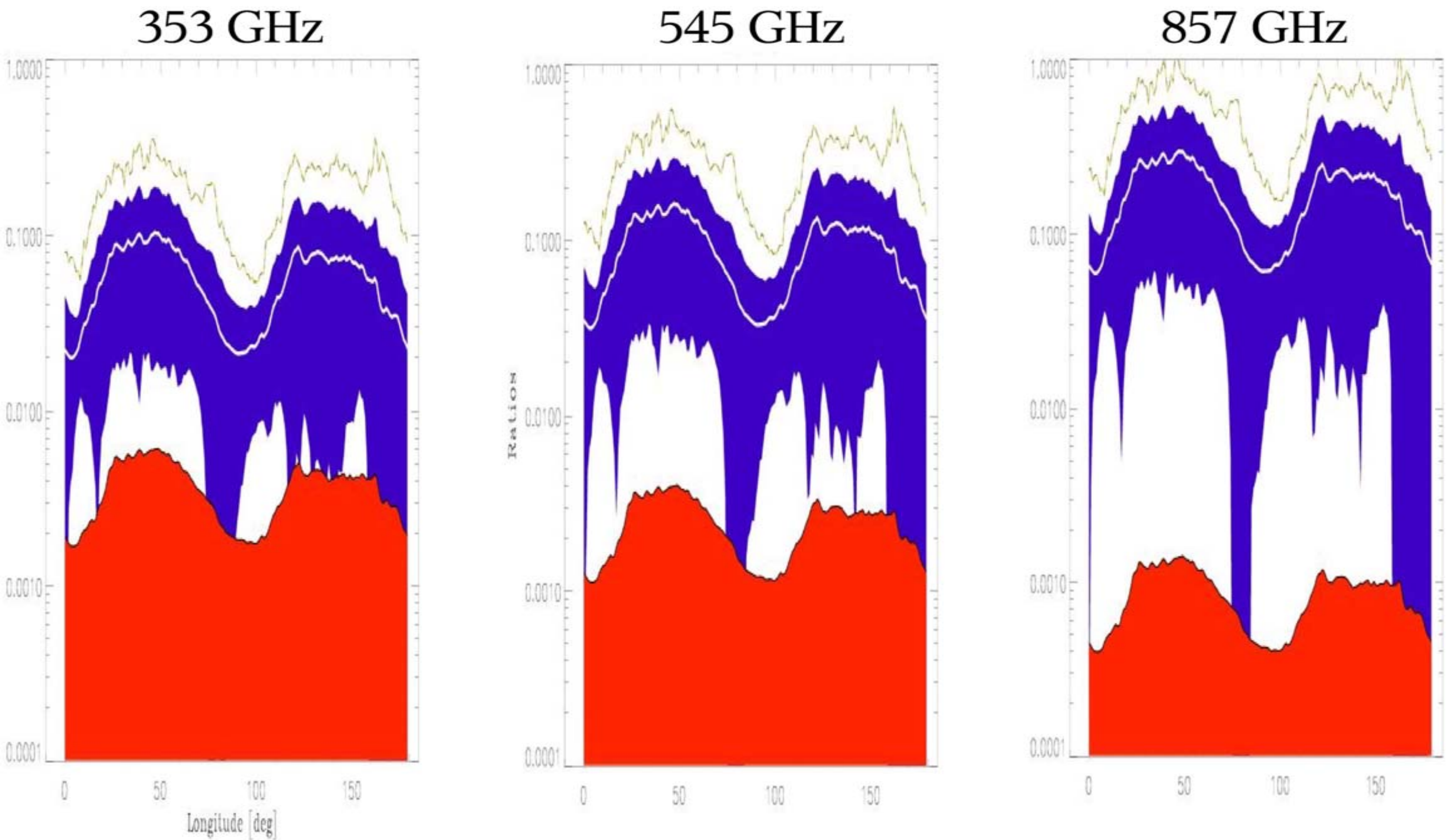

WG7 Meeting - 16 Jan 2007– Catania - Italy – EU   Maris, Burigana. - ZLE and Planck   13

Seasonal Modulation and Detection

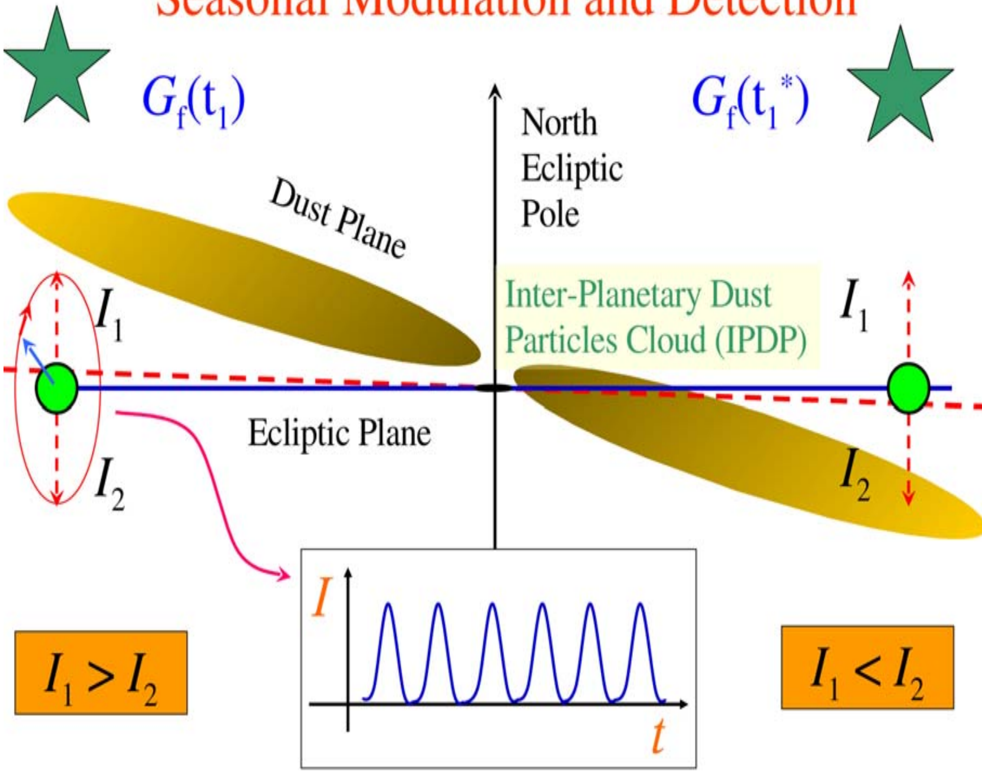

WG7 Meeting - 16 Jan 2007– Catania - Italy – EU   Maris, Burigana. - ZLE and Planck   15

Effect of Calibration Error

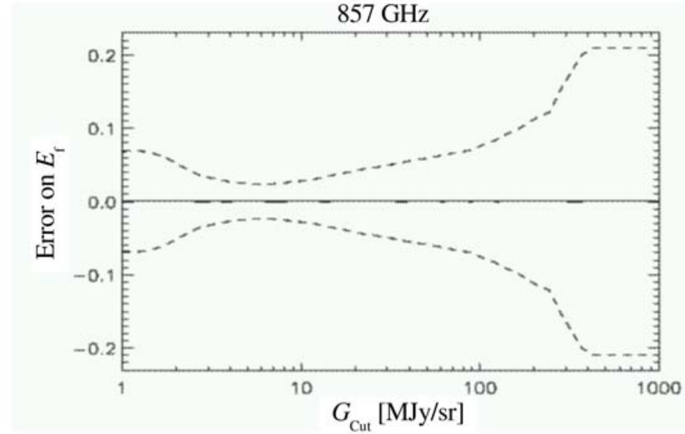

WG7 Meeting - 16 Jan 2007– Catania - Italy – EU   Maris, Burigana. - ZLE and Planck   27

Relative Accuracy on Ef (2deg patches)

		857 GHz	545 GHz	353 GHz
Expected Ef		0.6	0.3	0.1
Noise		0.15%	0.80%	2.40%
Pointing	RMS~1 arcmin	0.02%	0.03%	0.10%
Calibration	RMS~1%	4%	10%	23%
	RMS~0.1%	0.4%	1%	2.0%

(1sigma, and per patch)

WG7 Meeting - 16 Jan 2007– Catania - Italy – EU   Maris, Burigana. - ZLE and Planck   26

Conclusions

- *Planck* is now under CSL tests
- Requirements sensitivity have been essentially recovered during calibration tests
- Systematics are under control
- DPCs & ground segment works – recently, reviews have been carried out for LFI & HFI
- Instrument & DPC teams, WG & CT structures are intensively working!
- So … the future will be bright for
  - CMB & cosmological "main" science
  - Galactic & extragalactic "secondary" science

Thanks for your attention!

Acknowledgements

- I warmly acknowledge the *Planck* Collaboration – this talk is based in many parts on

PLANCK The Scientific Programme ESA-SCI(2005)1 astro-ph/0604069

- *Planck* (http://www.rssd.esa.int/Planck) is an ESA project with instruments funded by ESA member states (in particular the PI countries: France and Italy), and with special contributions from Denmark and NASA (USA).